

ESCUELA DE DOCTORADO DE LA UNIVERSIDAD DE CANTABRIA  
Doctorado en Ingeniería Química, de la Energía y de Procesos

# New biocompatible polymer membranes functionalized with graphene based nanomaterials for *in vitro* neural models

*Nuevas membranas de polímero biocompatible  
funcionalizadas con nanomateriales basados en grafeno  
para modelos neuronales in vitro*



Memoria de Tesis Doctoral para  
optar al título de Doctora por la  
Universidad de Cantabria

Presentada por:  
**Sandra Sánchez González**

Dirigida por:  
Prof. Dra. Ane Urtiaga Mendía  
Dra. Nazely Diban Gómez

Santander 2019



# UNIVERSIDAD DE CANTABRIA



ESCUELA DE DOCTORADO DE LA UNIVERSIDAD DE CANTABRIA  
DOCTORADO EN INGENIERÍAS QUÍMICA DE LA ENERGÍA Y PROCESOS

---

**New biocompatible polymer membranes  
functionalized with graphene based nanomaterials  
for *in vitro* neural models**

*Nuevas membranas de polímero biocompatible  
funcionalizadas con nanomateriales basados en grafeno  
para modelos neuronales in vitro*

---

Presentada por:

**Sandra Sánchez González**

Dirigida por:

**Prof. Dra. Ane Urtiaga Mendía**

**Dr. Nazely Diban Gómez**

Santander, 2019



The research of this thesis was performed in the Environmental Technologies and Bioprocesses research group of the Department of Chemical and Biomolecular Engineering of the University of Cantabria.

This research was financially supported by the Government of Cantabria/University of Cantabria, the Spanish Ministry of Economy, Industry and Competitiveness and the European Regional Development Fund through the projects: “Nuevos nanomateriales funcionalizados basados en grafeno como soportes para la regeneración de tejido nervioso” [JP03.640.69], “Estrategias avanzadas de integración de membranas y procesos electrocatalíticos y fotocatalíticos para la eliminación de contaminantes persistentes” [CTM2016-75509-R] and “Desarrollo de tecnologías innovadoras para el tratamiento de contaminantes perfluorados en aguas” [CTM2013-44081-R].

Moreover, the European Molecular Biology Organization (EMBO) awarded to the author, Sandra Sánchez González a short-term fellowship of three months in the Institute of Biomedical Engineering in the Department of Engineering Science (University of Oxford) (Ref. 7189).

Therefore, the most sincere gratitude is expressed to all these institutions.



*A mi familia*



# *Acknowledgements*

Deseo expresar mi más sincero agradecimiento a mis directoras de tesis. A la Prof. Dra. Ane Urtiaga por su confianza depositada en mí para la realización de esta tesis así como por su gran competencia profesional para realizar un mejor trabajo. A la Dra. Nazely Diban, por su ayuda, comprensión y dedicación durante todo este proceso. Gracias por enseñarme tantas cosas, en el ámbito profesional y personal.

Me gustaría agradecer al Dr. Jose Ramos-Vivas por haberme dado la oportunidad de trabajar en su laboratorio del Instituto de Investigación Marqués de Valdecilla (IDIVAL), y por haberme enseñado los conocimientos necesarios para mi investigación relacionados con la microbiología. Al Dr. Fidel Madrazo por ayudarme a obtener imágenes de células con el microscopio confocal. Igualmente, agradecer a María Lázaro-Díez e Itziar Chapartegui su ayuda, siempre dispuestas a echarme una mano cuando lo he necesitado.

I would like to thank Dr. Hua Ye for allowing me the opportunity to work at the University of Oxford in the Department of Engineering Science of the Institute of Biomedical Engineering. Furthermore, I personally would like to express my gratitude to Fabio Bianchi, who taught and supported me with the cell culture experiments. Finally, I sincerely would like to give special thanks to Miren Tamayo for her kindness, confidence and friendship. This experience would not have been the same without you.

Así mismo, agradecer la labor y asistencia recibida de las personas que forman parte del Departamento de Ingenierías Química y Biomolecular de la Universidad de Cantabria, incluyendo al personal administrativo, personal técnico y profesorado. También me gustaría dar las gracias a todos mis compañeros del departamento que me han acompañado durante estos años. Gracias por compartir logros, experiencias, conocimiento y algún que otro momento de estrés.

Por supuesto no me puedo olvidar de mis amigas, que aunque no nos veamos muy a menudo, siempre están dispuestas a ayudarme y escucharme. Gracias por las risas y los momentos de desconexión.

A Luis, por estar siempre a mi lado, en los momentos buenos para celebrar los logros así como en los no tan buenos para animarme y apoyarme. Gracias por sacarme siempre una sonrisa y por compartir tantos momentos desde hace tantos años.

Finalmente me gustaría dar las gracias a mi familia. Gracias por vuestro cariño y apoyo incondicional. A mis padres, quienes me han enseñado que la perseverancia y el esfuerzo son el camino para lograr objetivos. Y en especial a mi hermana Paula, que no ha dudado en ayudarme cuando lo he necesitado.

A todos, gracias.

# *Table of contents*

<b>Abstract/Resumen</b>	<b>1</b>
<b>Chapter 1. Tissue engineering approaches for the development of <i>in vitro</i> neural models</b>	<b>7</b>
1.1. <i>In vitro</i> neural model	9
1.2. Tissue engineering	15
1.3. Scaffolds for tissue engineering	17
1.4. Biomaterials	19
1.5. Graphene based nanomaterials (GbN)	20
1.6. Polymer/graphene hybrid scaffolds for tissue engineering	23
1.7. Bioreactors for tissue engineering	31
1.8. Aims and outline of this thesis	33
1.9. References	36
<b>Chapter 2. Fabrication and characterization of porous membranes of poly(<math>\epsilon</math>-caprolactone) with graphene based nanomaterials</b>	<b>45</b>
2.1. Introduction	47
2.2. Materials and methods	49
2.2.1. Materials	49
2.2.2. Synthesis of GO and rGO	49
2.2.3. Preparation of PCL-graphene flat membranes	51
2.2.4. Physical characterization of nanomaterials and membranes	52
2.2.5. Determination of glucose diffusion coefficient	56
2.2.6. Membrane flux characterization	58
2.2.7. Biocompatibility tests and static cell cultures on membranes	61
2.3. Results and discussion	63
2.3.1. Nanomaterial characterization	63
2.3.2. Physical characterization of the membranes	65
2.3.3. Glucose diffusion coefficient	74
2.3.4. Membrane flux properties	75

2.3.5. Membrane biocompatibility	79
2.4. Final remarks	81
2.5. References	82
<b>Chapter 3. Study of the hydrolytic degradation and stability</b>	<b>85</b>
<b>behavior of poly(<math>\epsilon</math>-caprolactone)/reduced graphene oxide</b>	
<b>membranes for <i>in vitro</i> models</b>	
3.1. Introduction	87
3.2. Materials and methods	90
3.2.1. Hydrolytic degradation assay	90
3.2.2. Physical-Chemical characterization	91
3.2.3. Functional characterization	93
3.3. Results and discussion	93
3.3.1. Physical-chemical properties characterization	93
3.3.2. Functional characterization	102
3.4. Final remarks	106
3.5. References	107
<b>Chapter 4. Influence of graphene-based nanomaterials oxidation</b>	<b>109</b>
<b>state on the differentiation and maturation of human neural</b>	
<b>progenitor cells behavior</b>	
4.1. Introduction	111
4.2. Materials and methods	113
4.2.1. Characterization of membranes	113
4.2.2. Cell culture assays	115
4.3. Results and discussion	120
4.3.1. Membrane characterization	120
4.3.2. Proliferation and differentiation of iPSCs culture	125
4.3.3. Proliferation, differentiation and maturation of NPCs culture	127
4.4. Final remarks	135
4.5. References	137

<b>Chapter 5. Design and preliminary testing of a perfusion poly(<math>\epsilon</math>-caprolactone)/reduced graphene oxide membrane bioreactor for cell cultures in dynamic conditions</b>	<b>139</b>
5.1. Introduction	141
5.2. Materials and methods	143
5.2.1. Perfusion membrane bioreactor	143
5.2.2. Dynamic cell culture	146
5.2.3. Nutrient flux characterization	148
5.3. Results and discussion	150
5.3.1. Nutrient flux characterization	150
5.3.2. Effect on cell behavior in static and dynamic conditions	155
5.4. Final remarks	158
5.5. References	159
<b>Chapter 6. Conclusions and challenges for future research</b>	<b>161</b>
6.1. Conclusions	163
6.2. Challenges for future research	166
6.3. Conclusiones	167
6.4. Retos para futuras investigaciones	170
<b>Appendix</b>	<b>173</b>
Appendix I. Composition of the culture medium	175
Appendix II. Scientific contributions	177



# *Abstract*

Nowadays, the study of the activity and functionality of the human brain is a challenging task, as it can only be evaluated indirectly by imaging techniques or analyzing post-mortem samples of individuals. The most commonly employed technique for studying the brain is the use of mouse *ex vivo* animal models. These models provide relevant data on the behavior of the brain to help in the early diagnosis of brain pathologies, the development of therapies and pharmacological treatments. However, due to the complexity of the human brain, animal models usually fail to accurately predict drug reactions for treating human patients. In consequence, the costs of preclinical trials suffer a substantial increase.

As a solution, researchers propose the development of an *in vitro* neural model of human origin with the target of mimicking the physiology and functionality of human brain tissues, as a way to obtain more representative results and to increase the success of subsequent preclinical trials. *In vitro* neural models are obtained from stem cells, which grow on an artificial support inside a bioreactor. This system is capable of creating a suitable microenvironment that stimulates and facilitates the cellular response. Therefore, cells proliferate and differentiate until they obtain the functionality of the desired organ. In recent years, many *in vitro* models have been developed by mimicking different human tissues/organs. Nonetheless, the high functional heterogeneity displayed in the regenerated neural tissues still hinders the experimental reproducibility from experimental batches.

The main challenge of this research is based on the **development and characterization of the proof of concept for an *in vitro* neural model with improved reproducible differentiation.**

*Chapter 1* provides an overview of the evolution of neuronal *in vitro* models. In addition, the methods and materials used to develop these models are addressed.

*Chapter 2* describes the procedures followed to fabricate and characterize biocompatible polymer membranes of poly( $\epsilon$ -caprolactone) functionalized with graphene nanomaterials. Moreover, the results are analyzed to evaluate the suitability of the membranes as cellular supports. An additional characterization of the membranes is exposed in *Chapter 3*, which defines and studies the hydrolytic degradation of the new functionalized membranes during a period of one year, simulating *in vitro* culture conditions.

Concerning the influence of the fabricated membranes materials over the cell stimulation in neural differentiation and functionality, *Chapter 4* studies the comparison between the different synthesized functionalized membranes and its capacity to induce neuronal functionality from human neural progenitor cells. Furthermore, *Chapter 5* develops a proof of concept test of the membranes in a perfusion bioreactor. On this chapter, the influence of mechanical stimuli produced by the bioreactor over the cell cultures is analyzed.

Finally, *Chapter 6* summarizes the most important conclusions of this work and proposes challenges for future research.

# Resumen

Actualmente, el estudio de la actividad y funcionalidad del cerebro humano resulta difícil ya que sólo puede ser evaluado de forma indirecta por técnicas de imagen o analizando individuos post-mortem. La técnica más comúnmente empleada en el estudio del cerebro es el uso de modelos animales *ex vivo* de ratón. Estos modelos proporcionan datos relevantes del comportamiento del cerebro que ayudan en el diagnóstico precoz de patologías cerebrales, desarrollo de terapias y tratamiento farmacológico. Sin embargo, debido a la complejidad del cerebro humano, los modelos de animales no suelen predecir con precisión las reacciones de los medicamentos para tratar a los pacientes humanos, dando lugar a un aumento sustancial en los costes de los ensayos preclínicos.

Como solución, los investigadores proponen el desarrollo de un modelo neuronal *in vitro* de origen humano dirigido a imitar la fisiología y funcionalidad del tejido cerebral humano necesario para obtener resultados más representativos y aumentar el éxito en los ensayos preclínicos posteriores. Los modelos neuronales *in vitro* se obtienen a partir de células madre, que son cultivadas sobre un soporte artificial dentro de un biorreactor. El sistema es capaz de crear un microambiente adecuado que estimula y facilita la respuesta celular. Por tanto, las células proliferan y se diferencian hasta obtener la funcionalidad del órgano deseado. En los últimos años, muchos modelos *in vitro* han sido desarrollados imitando diferentes órganos/tejidos humanos. Sin embargo, la alta heterogeneidad funcional mostrada por los tejidos neuronales regenerados aún dificulta la reproducibilidad experimental entre lotes experimentales.

El principal desafío de esta investigación se basa en el **desarrollo y caracterización de una prueba de concepto para un modelo neuronal *in vitro* con una reproducibilidad de diferenciación celular mejorada.**

El **Capítulo 1** proporciona una visión general sobre la evolución de los modelos neuronales *in vitro*. Además, se abordan los métodos y materiales utilizados para desarrollar estos modelos.

En el **Capítulo 2** se describen los procedimientos seguidos para la fabricación y caracterización de membranas poliméricas biocompatibles de poli( $\epsilon$ -caprolactona) funcionalizadas con nanomateriales de grafeno. Además, se analizan los resultados para evaluar la aptitud de las membranas como soportes celulares. La caracterización de las membranas se amplía en el **Capítulo 3**, donde se define y estudia la degradación hidrolítica de las nuevas membranas funcionalizadas, durante un periodo de un año, simulando condiciones de cultivo *in vitro*.

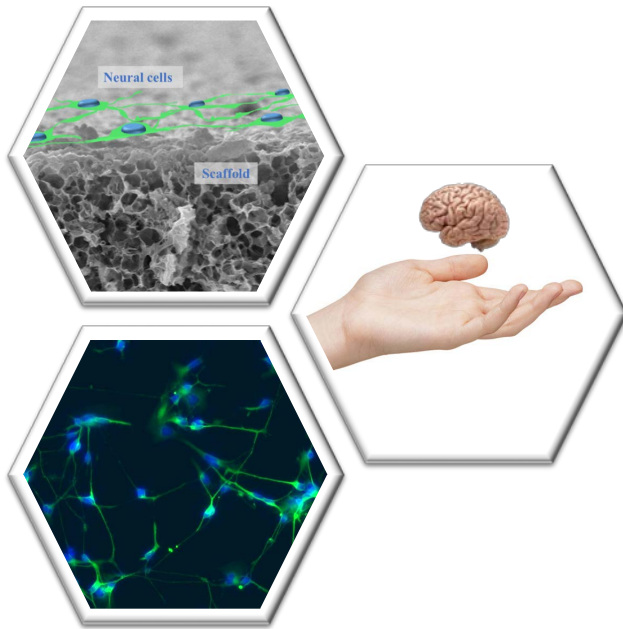
Con el objetivo de evaluar la influencia de los materiales de membrana fabricados sobre la estimulación de la diferenciación y de la funcionalidad neuronales, en el **Capítulo 4** se estudian y comparan las membranas funcionales sintetizadas con diferentes nanomateriales basados en grafeno, en su capacidad para inducir la funcionalidad neuronal a partir de células neuronales progenitoras de origen humano. Además, el **Capítulo 5** desarrolla una prueba de concepto de las membranas fabricadas en un biorreactor de perfusión, donde se analiza la influencia de los estímulos mecánicos producidos por el biorreactor en los cultivos celulares.

Finalmente, el **Capítulo 6** resume las conclusiones más importantes de este trabajo y se proponen retos para futuras investigaciones.

*Everything may die, nothing may be regenerated. It is for the science of the future to change, if possible, this harsh decree*

*Santiago Ramón y Cajál, 1928*





# *Chapter 1*

**Tissue engineering approaches for the development of *in vitro* neural models**



### **1.1. *In vitro* neural models**

The human brain is an extraordinarily complex structure that has fascinated scientists for centuries [1]. It is the least understood organ in the human body due to its difficult access and complex structure and function [2]. Nowadays, the techniques employed to analyze the human brain consist on imaging studies of the shape and activity of the brain. Similarly, post-mortem brain tissues are extensively examined by specialists [3]. Therefore, taking into account the techniques applied, the possibility to understand the mechanisms involved in the onset of neurodegenerative diseases is limited. Moreover, successful treatments for neurological disorders and brain damages are very difficult to achieve. For instance, it was reported that Alzheimer neurological disease was the sixth-leading cause of death in the United States in 2014. In light of these concerns, in 2017, 700,000 Americans over 65 years would have died from Alzheimer's disease, which involved an estimated total payment of \$259 billion in health care. From 2002 to 2012, several potential drugs for Alzheimer's were tested in clinical trials but only one drug, out of 244 tested drugs, was positively completed and approved by the Food and Drug Administration (FDA) [4]. A similar trend has been observed in other neurodegenerative diseases, such as Parkinson's disease or autism.

Drug development proceeds through several stages before approval for clinical use [5]. In fact, the development of a new drug can cost 800-1200 million dollars and takes around 10-12 years [6]. The use of animal models for preclinical drug screening is common. However, animal models are limited in their ability to mimic the complexity of the human brain and therefore, the translation of results from animal models to clinical trials largely fails [3,7]. As a consequence, the pharmaceutical

companies are looking for new strategies to study the human brain and to evaluate new drugs in order to get a return on the investment. To address this issue, new techniques have emerged as alternatives, such as *in silico* models [8] and the use of *in vitro* models based on human cells. The term *in silico* refers to the characterization of biological experiments through mathematical and computational modelling. Molecular profiles and interactions of cells and tissues are simulated using advanced statistics and sophisticated algorithms [9]. This alternative provides theoretical hypothesis that can be useful for laboratory experiments [10]. Meanwhile, the term *in vitro* involves experimental procedures working with cells or tissues from animal or human origin in a controlled environment, outside of a living organism. *In vitro* models include two dimensional (2D) and three dimensional (3D) cell cultures. Traditionally, 2D cell cultures grow in a monolayer on glass or plastic flasks [11]. 2D cell cultures are simple and convenient to be analyzed. They provide information on fundamental biological processes. However, they cannot mimic the complex *in vivo* tissue due to its physiological inaccuracies [2,5]. On the contrary, 3D cell cultures have an enormous potential to simulate the physiological and pathological functions of an *in vivo* tissue. They offer biologically superior structures with complex cellular interactions between cells and the extracellular matrix (ECM) [12–14].

In recent years, many *in vitro* models have been developed by mimicking different human tissues/organs, including kidney [15], intestine [13], or liver [16] among others. Indeed, there are biotechnology companies in the world, such as *MatTek Corporation*, *Insphero* or *Creative Bioarray*, which provide available and validated 2D and 3D *in vitro* models as an alternative to animal testing. However, the development of *in vitro* neural models remains a challenge due to its

complex cellular structure [17]. Several *in vitro* neural models have been developed but they still need to overcome some difficulties [18–20]. Figure 1.1 summarizes the progression on the development of *in vitro* neural models.

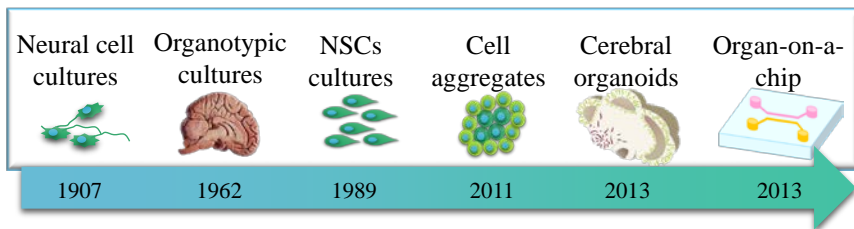


**Figure 1.1.** Evolution of *in vitro* neural models.

The study of *in vitro* neural models started in the early 20<sup>th</sup> century, using 2D *in vitro* cell cultures [21]. In 1907, Harrison [22] observed the outgrowth of nerve cells from a living animal for the first time. He isolated pieces of embryonic tissue from a frog to generate nerve fibers. After this study, 2D neural cell cultures were rapidly adapted and were improved by other researchers. They studied long-term cultured cells using new methodologies and enhanced techniques for analysis. On that basis, it was possible to study the morphology and function of neural cells [23,24]. Nevertheless, 2D neural cell cultures did not reflect the nature of the organisms because of isolation and lack of contact with other cells [25]. In contrast, intact cultures of neural tissue, called as organotypic cultures of brain slices, appeared as a promising tool for the brain studies. For instance, Wolf [26] employed an organotypic cerebellum to describe the brain tissue in detail for the first time. Also, Stoppini et al. [27] prepared old neonates hippocampal slices of rats to analyze the morphological and electrophysiological aspect of the hippocampus. Advantages of the organotypic brain slice models include

3D architecture and partial similarities with the *in vivo* brain tissue. Nonetheless, the major disadvantage of this model is the difficulty to acquire human samples [28]. Furthermore, the studies of the mature adult state as well as the reconstruction of neuronal pathways are identified as challenges to be overcome [25].

Neural cells were long considered to be incapable of regeneration. Nevertheless, advances in neural cell cultures showed differentiation of neurons from stem cells in the mid late 20<sup>th</sup> century [29]. Stem cells are self-renewing cells through cell division and can become into many different cell types in the body during early life and growth. Stem cells can be isolated from different sources: i) embryos to produce embryonic stem cells (ESCs) and ii) somatic cells to produce adult stem cells and induced pluripotent stem cells (iPSCs) [30]. In particular, iPSCs have revolutionized the availability of human stem cells as a source of neurons for experimental studies *in vitro*. iPSCs are somatic cells genetically reprogrammed by overexpressing key transcription factors to generate all cell types of the body in a similar way as ESCs do [31], but without taking into consideration any ethical concerns, which are attributed to the research with ESCs [32].

Regarding neural regeneration, the technology of neural stem cells (NSCs) is expected to replace almost any type of neuron lost from neurodegenerative disorders or brain damage [33]. Temple [34] reported the first culture of isolated NSCs from an embryonic rat brain in 1989. She determined that NSCs produced different types of cells from the nervous system. Since then, enhanced protocols were established and employed to differentiate stem cells into specific cells of the nervous system [35,36]. For example, Zhang et al. [35] cultured ESCs to generate

human neural rosettes for the first time. They are radial arrangements of columnar cells that resemble the neurogenesis *in vivo* [37].

2D *in vitro* cell cultures have provided extensive information about neural cell behavior, including spontaneous network formation, axonal guidance mechanisms or molecules in synaptic targeting. However, 3D *in vitro* cell cultures emerged to provide better understanding of cell–cell interactions and physiology compared to the ECM using the 2D *in vitro* cell cultures [21]. The first entirely 3D *in vitro* neural cell culture was developed by Eiraku et al. [38], who formed a 3D self-formation of optic-cup from mice ESC aggregates. After that, new strategies have been arisen to improve the efficiency of neural models such as the development of cerebral organoids [12,39,40]. Organoids are 3D multicellular stem cell derived constructs that simulate *in vivo* tissues. They were considered the “Method of the Year 2017” by Nature Methods due to its extraordinary potential as tools to study any biological process [41]. For neural applications, Lancaster et al. [12] developed a cerebral organoid, embedding human stem cells in Matrigel<sup>®</sup> that was sustained in a bioreactor. Matrigel<sup>®</sup>, a protein mixture, was used to support the cell growth that conferred the 3D structure of the tissue [42], while the bioreactor facilitated the nutrient and oxygen supply through the tissue formed. As a result, they developed an organoid created by various brain regions with 4 mm in diameter that was able to live up to 10 months.

Cerebral organoids can reflect the human brain physical complexity closer than 2D neural cell cultures or mice models [43]. But despite that, there are still several limitations that should be born in mind: i) the lack of vascularization produces limitation of the oxygen and nutrient exchange through the inner tissue leading to deficient cell growth and

maturation, or even cell death; and ii) the uncontrolled stem cell differentiation may result in stochastically variable regenerated neural tissue and an unorganized neural connectivity [18,19,44,45].

Alternatively, researchers focused their attention on more elaborated *in vitro* models, known as organ-on-chips [46–52]. Organ-on-chips are microfluidic devices for culturing living cells in continuously perfused, micro scaled chambers to model physiological functions of tissues and organs [53]. The chips consist of 3D polymeric microchannels lined by living human cells. The microchannels form 3D microarchitecture with spatial distribution of several tissues to mimic *in vivo* organs [54]. Organ-on-chip devices also enable to improve the control of relevant conditions (e.g. fluid flow, shear stress, mechanical deformations). For instance, Griep et al. [52] developed a microfluidic platform using human brain endothelial cells. They observed a positive influence over the cells related to the barrier tissue integrity, which is vital for the physiological activities of the tissue [55]. They also demonstrated the versatile potential of microfluidic models.

First, in contrast to macroscopic cell cultures, the microdevice allows the investigators to study a lower number of cells. Second, even single cells in high temporal and/or spatial resolution are also analyzed. Eventually, microdevices reduce reagents consumption, mass transport limitations and contamination risks [49,50]. Despite these advantages, the high heterogeneity displayed in the brain tissues still hinders the experimental reproducibility [56]. Therefore, further research about how to design better microdevices for inducing neural differentiation is important.

All the technologies aforementioned have emerged from converging progress in human cell sourcing and tissue engineering (TE), which is an interdisciplinary field that combines the principles of engineering and life sciences [57]. Alternative innovative strategies from both fields should be considered to overcome the limitations of developing an effective tissue formation, e.g. internal or external signals.

## **1.2. Tissue engineering**

TE emerged to generate functional tissues based on human cells to overcome the drawbacks of organ transplantation. However, recent advances in TE have also explored developing *in vitro* models of tissues and organs for drug screening as well as investigating diseases or new therapies [58].

The most common approach adopted in TE (Figure 1.2) employs the combination of living cells, biomaterials, biochemical (e.g. growth factors) and physical signals (e.g. mechanical loading) and bioreactors to create tissue-like structures [59–61].

Cells are derived from a donor tissue, which are commonly supported by a scaffold. In this way, cells can survive and proliferate. The scaffold should mimic the native tissue and allow permeation of nutrients and wastes [59]. The system composed of scaffold and cells can be implanted in the human body for regenerating tissue (*in vivo*). However, it can also be used as extra-corporeal devices for being studied in the development of therapies and pharmacological treatments (*in vitro*).

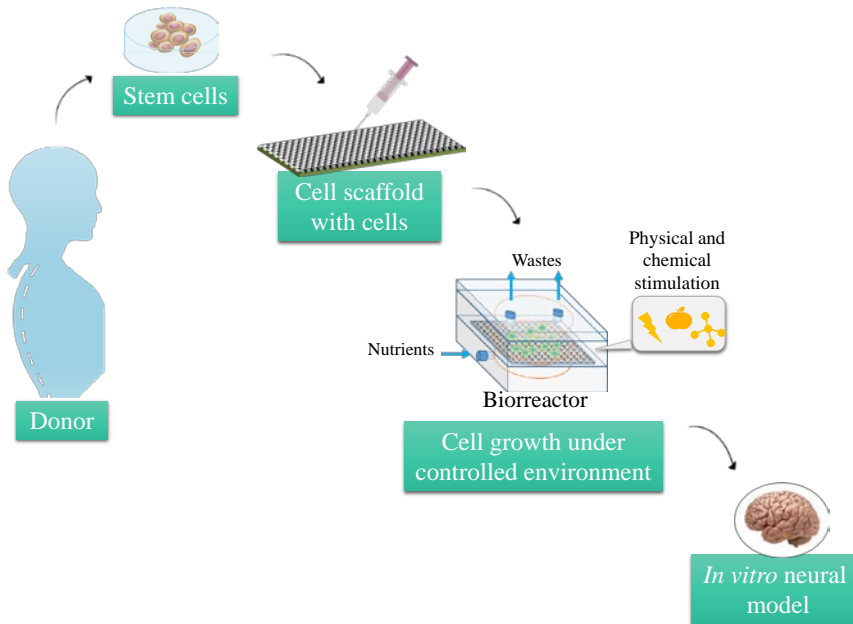


**Figure 1.2.** Graphical description of the fundamentals of TE to develop an *in vitro* neural model.

For *in vitro* models, it is necessary to provide an adequate cell environment, simulating *in vivo* conditions. Therefore, the use of bioreactors is considered essential to obtain the desired controlled microenvironment. Moreover, tissue-inducing substances and stimuli are critical signaling. They can influence the final cell fate. The growth factors, such as proteins [62] or vitamins[63], affect cell migration, proliferation and cellular differentiation. Meanwhile, different stimuli assist tissues to be functional. For example, mechanical pulses have been widely used in cartilage TE [64] and electrical stimulation has been employed to favor neural differentiation [65]. Also, the material of the scaffolds may intrinsically induce cell stimulation by morphological, topographical or chemical cues [66].

### 1.3. Scaffolds for tissue engineering

Scaffolds for TE are fundamental elements to develop an *in vitro* model. Scaffolds are structures made up of a variety of natural or synthetic materials, processed by different techniques to generate diverse formats (gels, porous solids and fibers) to support cells for tissue formation [2]. These types of materials refer to biomaterials, which will be explained later.

Scaffolds should present a number of features: i) Biocompatibility: cells must adhere, proliferate and differentiate on the scaffold, which must not elicit any immunological rejection to the cell culture; ii) Mechanical properties: the scaffolds should be able to maintain its structure and integrity within a determined time and to ensure new tissue formation and maturation up to its degradation; iii) Architecture: the scaffold should be designed to mimic the native tissue, developing a suitable environment to promote the cell growth and induce its behavior. A highly porous structure with interconnected pores is required to supply cell nutrients, oxygen and biochemical factors. These components are essential to maintain cell survival [67–69]. Moreover, cells' function control can be improved through specific micro/nanotopography designs [70]. In addition to these requirements, the possible biodegradation of the scaffold should be studied. Scaffolds are designed to allow cells to produce their own ECM. To avoid further surgery in *in vivo* applications, bioresorbable scaffolds should progressively degrade and metabolize while the tissue is formed at the same time. Although scaffolds in *in vitro* models do not have to be biodegradable because they are thought to be employed outside the body, the erodible behavior of the biomaterial

during the *in vitro* use has a potential influence on the feasibility of the cell model.

Among the different scaffolds for TE, e.g. porous scaffolds [71], hydrogels with embedded cells [72] and decellularized ECM [73], porous membranes have attracted the researchers' attention to act as porous scaffolds [74]. Although membranes are commonly used for separation processes [75], its thin and porous structure as well as the easy method of fabrication make them suitable for acting as porous scaffolds [76].

Different techniques have been employed to fabricate membranes. Some of the common methods are phase separation, electrospinning, freeze-drying, gas foaming or spin casting, among others [76,77]. Phase separation is a useful procedure to fabricate porous membranes. It is a versatile method that can work in most biodegradable polymers. The technique consists of the conversion of a polymer in solution to the solid state, which can proceed via different methods, namely, vapor induced phase separation (VIPS), evaporation induced phase separation (EIPS), thermally induced phase separation (TIPS) or non-solvent induced phase separation (NIPS) [78,79]. Particularly, NIPS method is a widely used technique to fabricate highly porous scaffolds. In this method, a polymeric solution is conformed as flat membrane or hollow fiber and then submerged in a coagulation bath, which contains the non-solvent. Due to the solvent and non-solvent exchange, polymer precipitation takes place [80]. Depending on the precipitation rate, the structure of the membranes may vary. Slow precipitation rates generate membranes with small size sponge-like pore morphologies, whereas instantaneous liquid-liquid demixing processes produce finger like pore morphologies [81].

## 1.4. Biomaterials

According to the European Society for Biomaterials (ESB), a biomaterial is a “material intended to interface with biological systems to evaluate, treat, augment or replace any tissue, organ or function of the body” [68]. Biomaterials play an important role in the field of TE. They have been widely used for different applications, such as cardiovascular, orthopedic and dentistry, among others [82]. However, new opportunities for clinical use have emerged due to advancements in cell and molecular biology, chemistry, materials science, and engineering. They are used to fabricate scaffolds that resemble the natural ECM, providing support and scaffolding for cell growth [83] as well as guide for new tissue formation [67].

Biomaterials for TE can be broadly classified into natural and synthetic polymers, and their composites [67]. Natural biomaterials, including chitosan, alginate and gelatin, present easy recognition by the biological environment, certain similarity to macromolecular substances, non-toxicity and biodegradability. Conversely, the lot-to-lot variability in molecular structure associated with animal/vegetal sourcing may limit its use. This is a problem particularly when trying to model and reproduce the scaffold structure and behavior. Besides, other possible drawbacks include the immunogenic response and pathogen transmission [84]. In contrast, synthetic biomaterials such as polystyrene, poly(L-lactic acid) (PLLA), poly(glycolic acid) (PGA) and poly( $\epsilon$ -caprolactone) (PCL), can be produced with a tailored architecture, controlling the shape and even the degradation characteristics. Furthermore, the synthetic polymers offer low bioactivity, which does not involve risk of immune response [67].

PCL is considered to be one of the most common synthetic biomaterials in neural TE [85–87]. It is a semi-crystalline, biocompatible and biodegradable aliphatic polyester. Moreover, this material has been approved by the FDA for its use in different biomedical devices [88]. Apart from that, because of its low melting temperature (55-60°C), PCL can be easily processed by using different fabrication techniques.

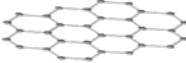
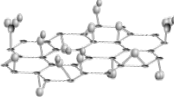
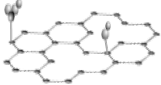
In general, the versatility of synthetic polymers provides the possibility of modifying its surface or/and bulk properties. In particular, the combination of different synthetic polymers with other components has been widely employed to modify their properties in neural TE applications, e.g. synthetic polymers combined with hydroxyapatite [89], graphene based nanomaterials [90–92], different natural and synthetic polymers [85,93] or bioactive glass [93].

### **1.5. Graphene based nanomaterials (GbNs)**

Graphene is a one atom thick sheet of graphite. It is exclusively composed by carbon atoms with  $sp^2$  bonding ( $\sigma$ -bonds), which are arranged in a 2D honeycomb lattice. Each carbon atom leaves 1 electron free ( $\pi$  electron) for electronic conduction. These  $\pi$  orbitals overlap, generating  $\pi$  bonds between each pair of adjacent carbon atoms [94]. The atomic structure together with the electron distribution of graphene result in excellent mechanical and optical properties, high chemical stability, large surface area and extraordinary thermal and electrical conductivity (Table 1.1). Graphene and its derivatives can be synthesized by a variety of methods, such as mechanical and chemical exfoliation, or chemical vapor deposition (CVD) [95]. Typical graphene based nanomaterials (GbNs) include the oxidized derivative of graphene, graphene oxide

(GO), and reduced GO (rGO). To produce rGO, the oxygen content of GO can be reduced by different techniques, such as hydro-thermal or chemical methods, forming vacancies and defects in the layers [96].

**Table 1.1.** Physical-chemical properties of GbNs.

Properties	Graphene	Graphene oxide (GO)	Reduced GO (rGO)
Structure			
Functional groups	None [97]	Carbonyl Hydroxyl Epoxides Carboxyl [97]	Low presence, depending on reduction efficiency [97]
Surface area (m <sup>2</sup> ·g <sup>-1</sup> )	2600 [98]	736.6 [99]	1200 [100]
Young Modulus (GPa)	1000 [98]	207-529 [101,102]	250 [95]
Thermal conductivity (W·m <sup>-1</sup> ·K <sup>-1</sup> )	5000 [98]	2000 [96]	0.14-2.87 [103]
Electrical conductivity (S·cm <sup>-1</sup> )	6000-10000 [96,98]	10 <sup>-1</sup> [96]	1.9x10 <sup>-3</sup> -298 [97]
Optical transmittance (%)	97.7 [98]	23-77 [102]	60-90 [96]
Wettability	Hydrophobic [98]	Hydrophilic [98]	Hydrophobic (less than graphene) [98]

Due to their extraordinary properties, graphene represent a promising nanomaterial for a wide range of applications, such as sensors, batteries, supercapacitors, flexible electronics and catalysis [104]. Besides, recent studies showed the high potential of graphene and its derivatives for biomedical applications. For instance, scientists have put into practice the function of graphene, GO and rGO in drug delivery [105], cancer therapies [106] or regenerative medicine [107,108]. In the field of neural

TE, GbNs have garnered significant interest, as they may provide suitable environments for neural cell behavior [108–110]. The electrical properties of graphene and rGO induce neural differentiation, as neural cells are electro-active [109,110]. Furthermore, graphene and GO can be easily functionalized with bioactive compounds such as proteins, enzymes, growth factors and DNA via physical interaction, which promote cell attachment and proliferation [94,109]. For instance, Park et al. [109] demonstrated that CVD graphene films served as an excellent cell-adhesion layer during the long-term differentiation process and induced the preferential differentiation of human neural stem cells towards neurons rather than glial cells. Similarly, Tang et al. [111] demonstrated great potentials of CVD graphene films to modulate the behavior of neural network *in vitro*. In another work, Li et al. [112] used 3D porous structures of graphene synthesized by CVD to culture and sustain NSC adhesion and proliferation. It was observed that 3D graphene-foams promoted sprouting of neurites after 5 days of culture. Furthermore, Serrano et al. [113] cultured embryonic neural progenitor cells on 2D and 3D free-standing partially reduced GO scaffolds. They observed that cells formed an intricate and well interconnected neural network after 14 days of *in vitro* culture tests.

Nevertheless, the use of GbNs in TE is still under study due to the contradictory toxic effects [108]. The biocompatibility and cytotoxicity of GbNs depend on their intrinsic physical-chemical properties. At the same time, these properties are defined by the raw materials and production methods used [114]. Both the concentration employed and the time of exposure of GbNs are also crucial factors for toxicity and biocompatibility [115]. For example, while Kang et al. [115] found apoptosis levels of PC12 cells after treatments with 50 and 100  $\mu\text{g}\cdot\text{mL}^{-1}$

of GO and rGO dispersions in culture medium for 24 h, Zhang et al. [116] detected apoptosis in PC12 cells using  $10 \mu\text{g}\cdot\text{mL}^{-1}$  of CVD graphene in culture medium. The thorough revision of Volkov et al. [117] found the potential cytotoxicity of GbNs as well as the potential risks under different types of exposures to these nanomaterials. They also observed reports which GbNs demonstrated its improved biocompatibility in different biomedical applications.

Up to now, controversy over the biological effect of GbNs still remains and concerns scientists. However, incorporations of low concentrations of GbNs in biomaterials have provided successful results [118–120] and therefore, researchers have felt attracted to study the GbNs effect to induce the controlled neuronal differentiation [111,121–124].

### **1.6. Polymer/graphene hybrid scaffolds for tissue engineering**

Several studies are focused on the polymer scaffold modification by introducing GbNs, as it promotes considerable improvements of the polymer performance, such as an increase of the hydrophilicity, the electrical properties or the cell response [125,126]. The degree of properties enhancement is influenced by the processing conditions that have been used, such as the GbN loading or the affinity of the components involved in the process.

Table 1.2 summarizes the techniques found in the literature to fabricate polymer/GbN scaffolds for TE. The polymer/GbN scaffold, the materials employed, the morphology/structure obtained and the type of tissue/cell studied in each work have been collected.

**Table 1.2.** Techniques to fabricate polymer/GbN scaffolds for TE. The GbNs concentration was referred to the final concentration in the polymer.

Technique	Scaffold	Materials	Structure	Tissue/cell	Ref.
Electrospinning	PCL/GO	PCL 4% (w/v) GO 0.05 wt% DMF	Nanofiber mesh film	Musculoskeletal	[127]
	PCL/G	PCL 6% (w/v) G 0.5, 1% (w/v) Chloroform	Microfiber mesh film	Fibroblast	[128]
	PCL/ MWCNTs	PCL 10wt% MWCNTs 0. 1, 0. 5, 1, 2, 5 wt% DMF/Methanol	Porous nanofiber mesh film	Fibroblast	[129]
	PCL/GO	PCL 14%(w/v) GO 0.1, 0.3, 0.5, 1 wt% DMF/DCM	Nanofiber mesh film	Bone, neural	[130]
	PVA/GO	PVA 9% (w/v) GO 0.5, 1, 3, 5 wt% Distilled water	Nanofiber mesh film	Bone	[131]
	PLA/ rGO-PEG & PLA/GO	PLA 10 wt% GO+PEG 1, 2, 5 wt% GO 1, 2 wt% Chloroform Other reagents for crosslinking	Nanofiber mesh film	Fibroblast	[132]
	PLLA with coated GO	PLLA 8 wt% GO (-) HFIP (polymer dispersion) Water (GO dispersion) Other reagents for crosslinking	Nanofiber mesh film	Neural	[91]
	PLGA/GO	PLGA 15 wt% GO 1 wt% THF/DMF	Nanofiber mesh film	Bone	[133]
	PLGA/GO	PLGA 10 wt% GO 0.1, 0.2 wt% THF/DMF	Nanofiber mesh film	Neural	[134]
	AP /G	AP 12 wt% G 0.5, 1, 2, 5 wt% distilled water	Nanofiber mesh film	Neural	[92]

Table 1.2 continued

<b>Technique</b>	<b>Scaffold</b>	<b>Materials</b>	<b>Structure</b>	<b>Tissue/cell</b>	<b>Ref.</b>
EIPS	PCL/GO & PCL/rGO	PCL 10% (w/v) GO or rGO 1 wt% THF (GO dispersion) Chloroform (rGO dispersion) NaCl for salt leaching	3D porous scaffolds	Bone	[135]
	PLA/GO & PLA/G	PLA (-) GO 0.4 wt% G 0.4 wt% Chloroform (G dispersion and polymer solution) Acetone (GO dispersion)	Film	Fibroblast	[114]
	PAM/GO Hydrogel	acrylamide 27, 24, 21, 18, 12 % (w/v) GO 0.07, 0.17, 0.29, 0.44, 1 % (w/v) Distilled water Initiators addition	Porous film	Peripheral nerve	[136]
	PTMC-MA/rGO	PTMC-MA (-) rGO 0, 0.5, 1, 2, 4 wt% Chloroform Initiators addition Other reagents for crosslinking	Film	Neural	[137]
TIPS	PADM with coated rGO	PADM (-) GO 1.5 wt% Water Other reagents for crosslinking	3D porous scaffold	Neural	[138]
	CHT/GO	CHT 1% (w/v) GO 0.5, 3 wt% AA	3D porous scaffold	Bone	[139]
	CMC/rGO Hydrogel	CMC 4% (w/v) GO 0.2% (w/v) Deionized water Other reagents for crosslinking	3D porous scaffold	Bone	[140]

Table 1.2 continued

Technique	Scaffold	Materials	Structure	Tissue/cell	Ref.
NIPS	PVA/GO	PVA (-) GO 1.5 wt% Water Methanol (precipitation bath)	Film	Bone	[141]
	PVA/rGO	PVA (-) GO 1.5 wt% DMSO Acidified methanol (precipitation bath) Other reagents for crosslinking	Film	Bone	[141]
Pressing/filtration	PCL/GO, PCL/rGO & PCL/AGO	PCL 10% (w/v) GO, rGO or AGO 1, 3, 5 wt% THF (GO dispersion) Chloroform (rGO dispersion) Dioxane (AGO dispersion) Methanol (precipitation bath)	Film	Bone	[142]
	PCL/rGO	PCL (-) rGO 0.1, 0.5, 1, 5 wt% DMF Methanol (precipitation bath) Other reagents for crosslinking	Film	Fibroblast, neural, muscle	[143]

(-): not defined, AA: acid acetic, AGO: amine functionalized GO, AP: alginate/PVA, CHT: chitosan, CMC: carboxymethyl chitosan, DCM: dichloromethane, DMF: N,N-dimethylformamide, DMSO: dimethyl sulfoxide, G: graphene, HA: hydroxyapatite, HFIP: 1,1,1,3,3,3-Hexa fluoro-2-propano, MWCNTs: multiwalled carbon nanotubes, PADM: porcine acellular dermal matrix, PEG: poly(ethylene glycol), PLA: poly(lactic acid), PLLA: poly(L-lactic acid), PLGA: poly(D,L-lactic-co-glycolic acid, PMA: polyacrylamide, PTMC-MA: poly(trimethylene carbonate) functionalized with methacrylic anhydride, PVA: polyvinyl alcohol, THF tetrahydrofuran.

The polymer/GbN scaffolds fabricated for TE applications used different methods to include GbNs in the polymer matrices. Most researchers dispersed the GbNs in an organic solvent and then added the

polymer, which was dissolved in the dispersion before removing the solvent to induce the polymer coagulation [128–130,134,135,142,143]. The dispersion was commonly achieved by means of ultrasonication. The sonication time and power depend on the materials and concentration used. For example, Holmes et al. [128] prepared a dispersion by sonicating 0.25 and 0.5 mg G in 5mL chloroform for 10 min. In another work, Qi et al. [131] dispersed 8 mg GO for 1 h in 9.2 mL distilled water by sonication. Despite the different sonication times, both conditions resulted in homogenous mixtures. Sonication produces a stable and homogeneous mixture. However, the main drawback of this technique is that long sonication times and/or high sonication powers can reduce sheet size and form undesirable defects, which undermine the properties of GbNs [144]. An alternative method to sonication is to stir the mixture vigorously, which disperses the GbNs in the polymer matrix with less power. Nevertheless, agglomerations can be produced due to the insufficient power applied. In consequence, Luo et al. [133] combined stirring with sonication in order to produce a homogeneous mixture, avoiding the GbNs agglomeration. Surface coating was another method used to include GbNs in polymer matrices [91,138]. This method is the simplest way to improve the surface properties of the polymer. However, this method implies poor stability of the coating layer on the scaffold [145]. Therefore, some researchers used chemical treatments to anchor the coated layer. For instance, Guo et al. [138] assembled GO on a PADM scaffold by a solution immersion process and reduced the GO with ascorbic acid in situ. Moreover, Zhang et al. [91] aminolyzed PLLA nanofiber scaffolds before soaking the nanofiber scaffolds in a GO solution. Although the scaffolds demonstrated excellent hydrophilicity

and biocompatible properties, the final content of GO in the nanofiber could not be controlled using this method.

Electrospinning has been commonly reported in the literature as a processing method to produce polymer/GbN composites for TE [91,92,127–134]. It is a versatile technique to generate aligned nano/microfibers that mimic the ECM [146]. This technique involves the application of an elevated electric field to generate nanofibers from a charged polymer solution or melt [147]. The novel electrospinning techniques have recently improved the production of electrospun fibers at large scale (up to 1.6 m) [148,149]. However, this method still does not achieve the large scale (hundreds of meters) that can produce the phase separation technique.

Therefore, the use of phase separation is a more convenient alternative to produce large batches of specimens with homogeneous morphological and functional properties. In fact, most of the commercially available membranes are developed by NIPS because of the simplicity and flexibility to scale-up the membrane fabrication [151]. On the contrary, using the EIPS technique, the formation of a solid membrane is too slow [79]. Furthermore, although the TIPS method can be applied to a wide range of polymers, including those that have poor solubility, the extreme processing temperatures limit its use. But even so, using the different available methods of phase separation, there is a large number of polymer/GbN films prepared for TE applications with a wide range of polymers employed such as PCL [135,142,143], PLA [114] or PVA [141,150].

Most of works reported in Table 1.2 generated the scaffold structure and the polymer/GbN composite by phase separation in one step. Nevertheless, some works pre-developed composites of polymer/GbN prior to define the desired structures. For instance, Rotman et al. [137] firstly used the NIPS technique to obtain PTMC-MA/rGO films, which were subsequently dissolved in chloroform and poured into a petri dish. After that, chloroform was evaporated and the resulting film was crosslinked in a N<sub>2</sub> atmosphere under UV light. As a result, they obtained electrically conductive materials with rGO concentrations above 2 wt%. They also observed significant neural cell proliferation between day 1 and day 5 in films with 1 and 4 wt% of rGO. In another work, Sayyar et al. [143] prepared covalently linked PCL/rGO films by adding 4-dimethylaminopyridine (DMAP) and N,N'-dicyclohexylcarbodiimide (DCC) in the polymer solution of GO/DMF/PCL. Additionally, they prepared blended PCL/rGO films in the absence of reductive toxic chemicals. The polymer solutions were precipitated in cold methanol and subsequently filtered and dried in a vacuum oven. The covalently linked PCL/rGO films presented better homogeneity than blended PCL/rGO films. However, no differences were observed in the growth of fibroblast cells cultured on both films. In general, the processing methods used to obtain scaffolds that have been reported in the literature frequently employed extreme temperature conditions [139,140], toxic reductive chemicals [140,141,143] and/or laborious and time consuming in situ polymerization techniques [136,137,152]. For instance, Dinescu et al. [139] obtained 3D porous CHT/GO scaffolds by freezing the polymer solution of GO/AA/CHT at -70°C and lyophilizing for 2 days at -50°C and 0.040 mbar. Linares et al. [141] used DCC and DMAP to reduce GO nanosheets. Furthermore, Li et al. [136] fabricated PAM/GO composite

scaffolds by in situ polymerization using acrylamide as monomer and ammonium persulfate and temperature as initiators.

Regarding the microstructure of the phase separation scaffolds, it can be tailored by adjusting different variables, such as the processing technique, the polymer concentration and the composition of the polymer solution [153]. Using the EIPS technique, Li et al. [136] observed different porous structure of the PAM/GO scaffolds depending on the GO concentration used. The PAM/GO increased its pore structure with interpenetrating polymer networks from GO concentrations of 0.07 to 0.29 wt%. However, the porosity of the scaffolds disappeared when the GO concentration was further increased (GO concentrations of 0.44 and 1 wt%). Specifically, for the NIPS technique, the choice of the solvent/non-solvent system has strong influence on the type of porosity obtained. The rapid demixing leads to macrovoids, while delay demixing produces dense structures [154]. For example, Linares et al. [141] used DMF as solvent and methanol as non-solvent to obtain dense PVA/GO films by NIPS. In order to open porous microstructures in dense films or scaffolds, other works employed additional techniques such as salt leaching or freeze-drying [135,139].

Overall, the different techniques applied to fabricate tissue engineered scaffolds are developed to improve the current scaffold design. Although each method has determined advantages and drawbacks, the appropriate selection of the methodologies must satisfy the requirements to develop the desired tissue [155] trying to minimize extreme processing conditions.

## 1.7. Bioreactors for tissue engineering

Bioreactors are fundamental devices for TE, as they are systems designed to cultivate cells under controlled *in vitro* environments (e.g. temperature, pH, oxygen levels, nutrients) [156–158]. They play a key role for culturing long-tissues, as they stimulate cells under dynamic conditions, enhancing the nutrients and oxygen transport. In addition, it is important to highlight the ability of bioreactors to provide uniform cell distribution and to improve the cellular fate by different physical signals, such as shear stress, compression, pressure or stretch [159,160]. Depending on the desired tissue formation, the operational conditions and the selected signals can vary.

For *in vitro* dynamic neural cell cultures, rotating wall vessel [161–165], spinner-flask [12,166,167] and perfusion bioreactors [168–170] have been commonly employed (Figure 1.3). Firstly, in the rotating wall vessels, the scaffold/cells are suspended in the culture media between the spaces of two cylindrical chambers. The outer cylinder rotates, producing simulated microgravity (weightless conditions) [158]. Ma et al. [164] observed that microgravity provided low fluid shear stress, which promoted the cell-cell interactions and neural cell differentiation.

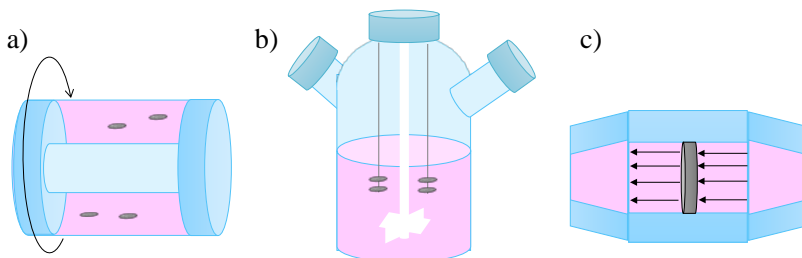


**Figure 1.3.** Typical bioreactors employed for TE applications, including a) rotating wall vessel, b) spinner-flask and c) perfusion bioreactor.

Secondly, scientists have observed suitable neural differentiation in spinner flask bioreactors using scaffolds [12,167,171] or suspension cultures (cell aggregates) [166]. For instance, Liu et al. [171] developed polyethylene terephthalate (PET) microfibrinous scaffolds to be used in a spinner flask for neural differentiation. The stirring in the bioreactor implied shear stress, which varied depending on the stirring conditions. Results showed that low agitation speeds led to higher cell density and more effective neural cell responses with respect to the static cultures. Lancaster et al. [12,172] also used a spinning bioreactor to develop a cerebral organoid model. They generated the most completed cerebral organoid tissue to date, using 3D Matrigel® scaffolds in a spinning bioreactor. However, there are still several limitations to develop an effective brain tissue formation. On the one hand, there is an insufficient control over cells. On the other hand, there is a lack of oxygen supply to internal 3D tissues, which was attributed to the low vascularization of the tissue structures.

Thirdly, perfusion bioreactors would help overcoming the low oxygenation of internal tissue structures observed by Lancaster et al. [12,172]. A perfusion bioreactor involves the constant and direct pumping of the culture medium through scaffolds, which enhances the exchange of oxygen and nutrients and provides mechanical stimuli to cells [169,173,174]. For instance, Morelli et al. [169] designed a bioreactor composed of poly-L-lactic acid (PLLA) highly aligned membrane hollow fiber to improve the neuronal differentiation. The microtube offered an indirect perfusion to the cells in the laminar flow regime, protecting cells from shear stress. As a result, the system promoted long-term growth and differentiation of neural cells.

Finally, based on the previous basic bioreactor configurations, improvements on the bioreactor designs for neural cultures can be done by for instance, introducing electrical stimulation [175]. Indeed, the application of electrical stimuli was demonstrated to influence the extension and orientation of neurite outgrowth from neurons cultured *in vitro* [65,176,177]. For example, Pires et al. [65] proliferated and differentiated NSCs in laminin coated surfaces of cross-linked poly(3,4-ethylenedioxythiophene) (PEDOT) polymer under 100 Hz pulsed direct current (DC) electrical stimulation. As a result, they obtained a higher population of neurons with higher elongations and longer neurites under electrical stimulus, compared to those obtained in its absence.

## 1.8. Aims and outline of this thesis

This thesis has been performed in the Environmental Technologies and Bioprocesses research group of the Department of Chemical and Biomolecular Engineering of the University of Cantabria. The main objective of this thesis was **the development and characterization of the proof of concept for an *in vitro* neural model based on a porous polymer membrane functionalized with graphene based nanomaterials to modulate reproducible neural differentiation.**

Specific objectives have been addressed in order to achieve the main objective:

- Fabrication and characterization of highly porous flat membranes of PCL biopolymer functionalized with low loadings of GbNs. The hypothesis behind the introduction of GbNs in the porous membranes is to incorporate an electrical and/or biochemical stimulation to cause an effect on the neural cell response. Furthermore, the high porosity of the

polymer membranes helps to ensure sufficient supply of nutrients to the cells and to facilitate the migration and colonization of the scaffold by the cells.

- Evaluation of the long-term hydrolytic degradation of the fabricated PCL/GbN membranes to determine their aptitude to act as scaffolds during hydrolytic attack in *in vitro* perfusion bioreactors for neural tissue regeneration. Factors such as the mechanical stability and the potential cytotoxic effect of the materials have been evaluated.

- Analysis of the ability of the fabricated PCL/GbN membranes to induce neuronal functionality to differentiated stem cells. In particular, the effect of the chemical state (oxidative or reductive) of the GbNs and the nanomaterials dispersion on the membrane matrix on neural differentiation and maturation will be evaluated. This study would help elucidating the importance of the chemical state of the nanomaterial and the GbN accessibility to direct cell differentiation and maturation fate.

- Proof of concept on the use of the PCL/GbN membranes in a perfusion membrane bioreactor to examine the influence of introducing mechanical stimuli on neural cell cultures, additionally to the intrinsic material stimulation of the PCL/rGO membrane to promote neural cell differentiation.

Hence, in **Chapter 2**, membranes composed of PCL and GO or rGO were fabricated under mild temperatures without toxic reductive chemicals by the NIPS technique. The membranes were evaluated by means of morphological, physical, filtration and biocompatibility characterization, demonstrating promising properties to be used as cell supports in perfusion bioreactors for *in vitro* neural models.

**Chapter 3** investigated the long-term hydrolytic degradation of the PCL/rGO membranes, simulating *in vitro* conditions. During one year, the structural stability of the membranes was studied by mechanical, morphological and thermal characterization. Moreover, the degradation by-products were analyzed and the potential cytotoxic effects caused by the membrane biodegradation were estimated.

The core task of **Chapter 4** was to evaluate the ability of the PCL/GO and PCL/rGO membranes to elicit the differentiation of human iPSCs-derived neural progenitor cells in mature neural cells under static conditions. The effects of nanoparticle distribution along the membrane and of the intrinsic nanomaterial properties, on the cell behavior, were studied. Cells were evaluated at proliferation, differentiation and maturation stages. The functionality of the neural-derived cells cultured on the membranes was assessed by means of calcium imaging.

In **Chapter 5**, a perfusion membrane bioreactor was used to evaluate the mechanical stimuli effect on neural cells cultured on the membranes. Likewise, the nutrient consumption and metabolites production was characterized by protein, glucose and lactate analyses. In addition, the oxygen concentration and pressure of the system were monitored in the experimental device.

In **Chapter 6**, general conclusions arising from the original results of this thesis will be discussed. This chapter also outlines some future perspectives.

## 1.9. References

- [1] L. C. Case, M. Tessier-Lavigne, *Curr. Biol.* **2005**, *15*, R749.
- [2] A. R. Murphy, A. Laslett, C. M. O'Brien, N. R. Cameron, *Acta Biomater.* **2017**, *54*, 1.
- [3] B. Bae, C. A. Walsh, *Perspectives* **2013**.
- [4] A. Association, *Alzheimer's Dement.* **2017**, *13*, 325.
- [5] S. A. Langhans, *Front. Pharmacol.* **2018**, *9*, 1.
- [6] I. Parvova, N. Danchev, E. Hristov, *J. Clin. Med.* **2011**, *4*, 19.
- [7] Y. Xiong, A. Mahmood, M. Chopp, *Nat. Rev. Neurosci.* **2013**, *14*, 128.
- [8] X. Jin, F. Zhu, H. Mao, M. Shen, K. H. Yang, *J. Biomech.* **2013**, *46*, 2795.
- [9] G. Lemon, S. Sjöqvist, M. L. Lim, N. Feliu, A. B. Firsova, R. Amin, Y. Gustafsson, A. Stuewer, E. Gubareva, J. Haag, P. Jungebluth, P. Macchiarini, *Curr. Stem Cell Res. Ther.* **2015**, *0*, 1.
- [10] D. P. Williams, R. Shipley, M. J. Ellis, S. Webb, J. Ward, I. Gardner, S. Creton, *Toxicol. Res. (Camb)*. **2013**, *2*, 40.
- [11] R. Edmondson, J. J. Broglie, A. F. Adcock, L. Yang, *Assay Drug Dev. Technol.* **2014**, *12*, 207.
- [12] M. A. Lancaster, M. Renner, C.-A. Martin, D. Wenzel, L. Bicknell, M. Hurler, T. Hofrey, J. Perninger, A. Jackson, J. Knoblich, *Nature* **2013**, *501*, 373.
- [13] F. Liu, J. Huang, B. Ning, Z. Liu, S. Chen, W. Zhao, *Front. Pharmacol.* **2016**, *7*, 1.
- [14] M. Ravi, V. Paramesh, S. R. Kaviya, E. Anuradha, F. D. Paul Solomon, *J. Cell. Physiol.* **2015**, *230*, 16.
- [15] L. G. Griffith, M. A. Swartz, *Nat. Rev. Mol. Cell Biol.* **2006**, *7*, 211.
- [16] T. Takebe, R. R. Zhang, H. Koike, M. Kimura, E. Yoshizawa, M. Enomura, N. Koike, K. Sekine, H. Taniguchi, *Nat. Protoc.* **2014**, *9*, 396.
- [17] G. Quadrato, J. Brown, P. Arlotta, *Nat. Med.* **2016**, *22*, 1220.
- [18] C. T. Lee, R. M. Bendriem, W. W. Wu, R. F. Shen, *J. Biomed. Sci.* **2017**, *24*, 1.
- [19] E. Di Lullo, A. R. Kriegstein, *Nat. Rev. Neurosci.* **2017**, *18*, 573.
- [20] I. Kelava, M. A. Lancaster, *Dev. Biol.* **2016**, *420*, 199.
- [21] A. M. Hopkins, E. DeSimone, K. Chwalek, D. L. Kaplan, *Prog. Neurobiol.* **2015**, *125*, 1.
- [22] R. G. Harrison, *Anatomical Lab.* **1907**, *1*, 116.
- [23] R. K. Jakoby, C. C. Turbes, M. D. Freeman, *Surg. Exp. Lab.* **1958**.
- [24] E. J. H. Nathaniel, D. R. Nathaniel, *Exp. Neurol.* **1973**, *40*, 333.

- [25] C. Humpel, *Neuroscience* **2015**, 305, 86.
- [26] M. K. Wolf, *J. Comp. Neurol.* **1970**, 140, 281.
- [27] L. Stoppini, P.-A. Buchs, D. Muller, *J. Neurosci. Methods* **1991**, 37, 173.
- [28] E. Eugene, F. Cluzeaud, C. Cifuentes-Diaz, S. Clemenceau, M. Baulac, J.-C. Poncer, R. Miles, *J Neurosci Methods* **2014**, 30, 234.
- [29] M. k. Dengke, M. A. Bonaguidi, G. Ming, H. Song, *Cell Res.* **2009**, 19, 672.
- [30] R. F. Halliwell, *Neurochem. Int.* **2017**, 106, 37.
- [31] J. Hipp, A. Atala, *Stem Cell Rev.* **2008**, 4, 3.
- [32] B. Lo, L. Parham, *Res. Endocr Rev.* **2009**, 30, 203.
- [33] J. J. Breunig, T. F. Haydar, P. Rakic, *Neuron* **2011**, 70, 614.
- [34] S. Temple, *Nature* **1989**, 340, 471.
- [35] S.-C. Zhang, M. Wernig, I. D. Duncan, O. Brüstle, J. A. Thomson, *Nat. Biotechnol.* **2001**, 19, 1129.
- [36] K. Watanabe, D. Kamiya, A. Nishiyama, T. Katayama, S. Nozaki, H. Kawasaki, Y. Watanabe, K. Mizuseki, Y. Sasai, *Nat. Neurosci.* **2005**, 8, 288.
- [37] P. G. Wilson, S. S. Stice, *Stem Cell Rev.* **2006**, 2, 67.
- [38] M. Eiraku, N. Takata, H. Ishibashi, M. Kawada, E. Sakakura, S. Okuda, K. Sekiguchi, T. Adachi, Y. Sasai, *Nature* **2011**, 472, 51.
- [39] J. Jo, Y. Xiao, A. X. Sun, E. Cukuroglu, H. D. Tran, J. Göke, Z. Y. Tan, T. Y. Saw, C. P. Tan, H. Lokman, Y. Lee, D. Kim, H. S. Ko, S. O. Kim, J. H. Park, N. J. Cho, T. M. Hyde, J. E. Kleinman, J. H. Shin, D. R. Weinberger, E. K. Tan, H. S. Je, H. H. Ng, *Cell Stem Cell* **2016**, 19, 248.
- [40] X. Qian, F. Jacob, M. M. Song, H. N. Nguyen, H. Song, G. Ming, *Nat. Protoc.* **2018**, 13, 565.
- [41] *Nat. Methods* **2018**, 15, 1.
- [42] C. S. Hughes, L. M. Postovit, G. A. Lajoie, *Proteomics* **2010**, 10, 1886.
- [43] V. Marx, *Nature* **2015**, 522, 373.
- [44] S. P. Pasca, *Nature* **2018**, 553, 437.
- [45] S. H. Kim, S. K. Im, S. J. Oh, S. Jeong, E. S. Yoon, C. J. Lee, N. Choi, E. M. Hur, *Nat. Commun.* **2017**, 8, 1.
- [46] S. Halldorsson, E. Lucumi, R. Gómez-Sjöberg, R. M. T. Fleming, *Biosens. Bioelectron.* **2015**, 63, 218.
- [47] J.-H. Choi, H.-Y. Cho, J.-W. Choi, *Bioengineering* **2017**, 4, 77.
- [48] F. C. Nery, C. C. da Hora, U. Yaqub, X. Zhang, D. M. McCarthy, P. G. Bhide, D. Irimia, X. O. Breakefield, *J. Neurosci. Methods* **2015**, 0, 80.
- [49] A. Shamloo, M. Heibatollahi, M. R. K. Mofrad, *Integr. Biol.*

- 2015**, 7, 335.
- [50] A. Gladkov, Y. Pigareva, D. Kutyina, V. Kolpakov, A. Bukatin, I. Mukhina, V. Kazantsev, A. Pimashkin, *Sci. Rep.* **2017**, 7, 1.
- [51] G. Adriani, D. Ma, A. Pavesi, R. D. Kamm, E. L. K. Goh, *Lab Chip* **2017**, 17, 448.
- [52] L. M. Griep, F. Wolbers, B. De Wagenaar, P. M. Ter Braak, B. B. Weksler, I. A. Romero, P. O. Couraud, I. Vermes, A. D. Van Der Meer, A. Van Den Berg, *Biomed. Microdevices* **2013**, 15, 145.
- [53] S. N. Bhatia, D. E. Ingber, *Nat. Biotechnol.* **2014**, 32, 760.
- [54] E. W. Esch, A. Bahinski, D. Huh, *Nat. Rev. Drug Discov.* **2015**, 14, 248.
- [55] B. Srinivasa, A. R. Kolli, M. B. Esch, H. E. Abaci, M. L. Shuler, J. J. Hickman, *J. Lab. Autom.* **2015**, 20, 107.
- [56] I. Kelava, M. A. Lancaster, *Cell Stem Cell* **2016**, 18, 736.
- [57] R. Langer, J. P. Vacanti, **1993**.
- [58] G. V. Novakovic, T. Eschenhagen, C. Mummery, **2016**, 1.
- [59] F. Berthiaume, T. J. Maguire, M. L. Yarmush, *Annu. Rev. Chem. Biomol. Eng.* **2011**, 2, 403.
- [60] R. Langer, J. P. Vacanti, *Science (80-. )*. **1993**, 260, 920.
- [61] M. Sladkova, G. de Peppo, *Processes* **2014**, 2, 494.
- [62] K. Lee, E. A. Silva, D. J. Mooney, *J. R. Soc. Interface* **2011**, 8, 153.
- [63] F. L. Wei, C. Y. Qu, T. L. Song, G. Ding, Z. P. Fan, Y. Liu, S. Zhang, C.M., Shi, S. L. Wang, *J cell Physiol* **2012**, 227, 3216.
- [64] K. Li, C. Zhang, L. Qiu, L. Gao, X. Zhang, *Tissue Eng. Part B Rev.* **2017**, 23, 399.
- [65] F. Pires, Q. Ferreira, C. A. V. Rodrigues, J. Morgado, F. C. Ferreira, *Biochim. Biophys. Acta - Gen. Subj.* **2015**, 1850, 1158.
- [66] O. Akhavan, E. Ghaderi, *J. Mater. Chem. B* **2013**, 1, 6291.
- [67] F. M. Chen, X. Liu, *Prog. Polym. Sci.* **2016**, 53, 86.
- [68] F. J. O'Brien, *Mater. Today* **2011**, 14, 88.
- [69] L. S. Nair, C. T. Laurencin, *Prog. Polym. Sci.* **2007**, 32, 762.
- [70] H. Miyoshi, T. Adachi, *Tissue Eng. Part B Rev.* **2014**, 20, 609.
- [71] N. M. S. Bettahalli, J. Vicente, L. Moroni, G. A. Higuera, C. A. Van Blitterswijk, M. Wessling, D. F. Stamatialis, *Acta Biomater.* **2011**, 7, 3312.
- [72] B. Guo, B. Lei, P. Li, P. X. Ma, *Regen. Biomater.* **2015**, 2, 47.
- [73] K. Shimomura, B. B. Rothrauff, R. S. Tuan, *Am. J. Sports Med.* **2017**, 45, 604.
- [74] B. P. Chan, K. W. Leong, *Eur. Spine J.* **2008**, 17, S467.
- [75] A. Pérez-González, R. Ibáñez, P. Gómez, A. M. Urtiaga, I. Ortiz, J. A. Irabien, *J. Memb. Sci.* **2015**, 473, 16.

- [76] R. Suntornnond, J. An, W. Y. Yeong, C. K. Chua, *Macromol. Mater. Eng.* **2015**, *300*, 858.
- [77] A. Subramanian, U. M. Krishnan, S. Sethuraman, *J. Biomed. Sci.* **2009**, *16*, 108.
- [78] U. Jammalamadaka, K. Tappa, *J. Funct. Biomater.* **2018**, *9*, 22.
- [79] A. Kausar, *Polym. Plast. Technol. Eng.* **2017**, *56*, 1.
- [80] A. F. Ismail, N. Ridzuan, S. A. Rahman, *Membr. Sci. Technol.* **2002**, *24*, 1025.
- [81] G. R. Guillen, Y. Pan, M. Li, E. M. V. Hoek, *Ind. Eng. Chem. Res.* **2011**, *50*, 3798.
- [82] A. Sharma, G. Sharma, *Biomaterials and Their Applications*, **2018**.
- [83] T. J. Keane, S. F. Badylak, *Semin. Pediatr. Surg.* **2014**, *23*, 112.
- [84] O. O. Ige, L. E. Umoru, S. Aribio, *ISRN Mater. Sci.* **2012**, *2012*, 1.
- [85] E. Schnell, K. Klinkhammer, S. Balzer, G. Brook, D. Klee, P. Dalton, J. Mey, *Biomaterials* **2007**, *28*, 3012.
- [86] L. Ghasemi-Mobarakeh, M. P. Prabhakaran, M. Morshed, M. H. Nasr-Esfahani, H. Baharvand, S. Kiani, S. S. Al-Deyab, S. Ramakrishna, *J. Tissue Eng. Regen. Med.* **2011**, *5*, e17.
- [87] B. Mammadov, M. Sever, M. O. Guler, A. B. Tekinay, *Biomater. Sci.* **2013**, *1*, 1119.
- [88] M. Pérez-garnes, J. A. Barcia, U. Gómez-pinedo, M. M. Pradas, A. Vallés-lluch, *Cells and Biomaterials in Regenerative Medicine. Chapter 7: Materials for Central Nervous System Tissue Engineering*, **2014**.
- [89] C. K. Chua, K. F. Leong, K. H. Tan, F. E. Wiria, C. M. Cheah, *J. Mater. Sci. Mater. Med.* **2004**, *15*, 1113.
- [90] S. Shah, P. T. Yin, T. M. Uehara, S. T. D. Chueng, L. Yang, K. B. Lee, *Adv. Mater.* **2014**, *26*, 3673.
- [91] K. Zhang, H. Zheng, S. Liang, C. Gao, *Acta Biomater.* **2016**, *37*, 131.
- [92] N. Golafshan, M. Kharaziha, M. Fathi, *Carbon N. Y.* **2017**, *111*, 752.
- [93] A. D. Hammadi, *J. Nanomedicine Res.* **2016**, *4*, DOI 10.15406/jnmr.2016.04.00088.
- [94] S. R. Shin, Y. C. Li, H. L. Jang, P. Khoshakhlagh, M. Akbari, A. Nasajpour, Y. S. Zhang, A. Tamayol, A. Khademhosseini, *Adv. Drug Deliv. Rev.* **2016**, *105*, 255.
- [95] Y. Zhu, S. Murali, W. Cai, X. Li, J. W. Suk, J. R. Potts, R. S. Ruoff, *Adv. Mater.* **2010**, *22*, 3906.
- [96] S. Goenka, V. Sant, S. Sant, *J. Control. Release* **2014**, *173*, 75.
- [97] S. Pei, H. M. Cheng, *Carbon N. Y.* **2012**, *50*, 3210.

- [98] M. Gu, Y. Liu, T. Chen, F. Du, X. Zhao, C. Xiong, Y. Zhou, *Tissue Eng. Part B. Rev.* **2014**, *20*, 1.
- [99] P. Montes-Navajas, N. G. Asenjo, R. Santamaría, R. Menéndez, A. Corma, H. García, *Langmuir* **2013**, *29*, 13443.
- [100] K. Dž, F. Korać, S. Gutić, **2015**.
- [101] J. W. Suk, R. D. Piner, J. An, R. S. Ruoff, *ACS Nano* **2010**, *4*, 6557.
- [102] S. H. Kang, T. H. Fang, Z. H. Hong, *J. Phys. Chem. Solids* **2013**, *74*, 1783.
- [103] T. Schwamb, B. R. Burg, N. C. Schirmer, D. Poulidakos, *Nanotechnology* **2009**, *20*, 405704.
- [104] A. Nag, A. Mitra, S. C. Mukhopadhyay, *Sensors Actuators, A Phys.* **2018**, *270*, 177.
- [105] Q. Zhang, Z. Wu, N. Li, Y. Pu, B. Wang, T. Zhang, J. Tao, *Mater. Sci. Eng. C* **2017**, *77*, 1363.
- [106] S. Ghanbarzadeh, H. Hamishehkar, M. Sciences, M. Sciences, H. Hamishehkar, D. Applied, G. Ave, **n.d.**
- [107] C. Gardin, A. Piattelli, B. Zavan, *Trends Biotechnol.* **2016**, *34*, 435.
- [108] Kenry, W. C. Lee, K. P. Loh, C. T. Lim, *Biomaterials* **2018**, *155*, 236.
- [109] S. Y. Park, J. Park, S. H. Sim, M. G. Sung, K. S. Kim, B. H. Hong, S. Hong, *Adv. Mater.* **2011**, *23*, H263.
- [110] O. Akhavan, *J. Mater. Chem. B* **2016**, *4*, 3169.
- [111] M. Tang, Q. Song, N. Li, Z. Jiang, R. Huang, G. Cheng, *Biomaterials* **2013**, *34*, 6402.
- [112] N. Li, Q. Zhang, S. Gao, Q. Song, R. Huang, L. Wang, L. Liu, J. Dai, M. Tang, G. Cheng, *Sci. Rep.* **2013**, *3*, 1604.
- [113] M. C. Serrano, J. Patiño, C. García-Rama, M. L. Ferrer, J. L. G. Fierro, A. Tamayo, J. E. Collazos-Castro, F. del Monte, M. C. Gutiérrez, *J. Mater. Chem. B* **2014**, *2*, 5698.
- [114] A. M. Pinto, S. Moreira, I. C. Gonçalves, F. M. Gama, A. M. Mendes, F. D. Magalhães, *Colloids Surfaces B Biointerfaces* **2013**, *104*, 229.
- [115] Y. Kang, J. Liu, J. Wu, Q. Yin, H. Liang, A. Chen, L. Shao, *Int. J. Nanomedicine* **2017**, *12*, 5511.
- [116] Y. Zhang, S. F. Ali, E. Dervishi, Y. Xu, Z. Li, D. Casciano, A. S. Biris, *Am. Chemical Soc.* **2010**, *4*, 3181.
- [117] Y. Volkov, J. McIntyre, A. Prina-Mello, *2D Mater.* **2017**, *4*, DOI 10.1088/2053-1583/aa5476.
- [118] D. Ege, A. R. Kamali, A. R. Boccaccini, *Adv. Eng. Mater.* **2017**, *19*, 16.

- [119] J. R. Potts, D. R. Dreyer, C. W. Bielawski, R. S. Ruoff, *Polymer (Guildf)*. **2011**, 52, 5.
- [120] M. Silva, N. M. Alves, M. C. Paiva, *Polym. Adv. Technol.* **2018**, 29, 687.
- [121] O. Akhavan, E. Ghaderi, S. A. Shirazian, R. Rahighi, *Carbon N. Y.* **2016**, 97, 71.
- [122] X. Ding, H. Liu, Y. Fan, *Adv. Healthc. Mater.* **2015**, 4, 1451.
- [123] R. Guo, S. Zhang, M. Xiao, F. Qian, Z. He, D. Li, X. Zhang, H. Li, X. Yang, M. Wang, R. Chai, M. Tang, *Biomaterials* **2016**, 106, 193.
- [124] K. Yang, J. Lee, J. S. Lee, D. Kim, G. E. Chang, J. Seo, E. Cheong, T. Lee, S. W. Cho, *ACS Appl. Mater. Interfaces* **2016**, 8, 17763.
- [125] S. Kumar, K. Chatterjee, *ACS Appl. Mater. Interfaces* **2016**, 8, 26431.
- [126] V. Mittal, *Macromol. Mater. Eng.* **2014**, 299, 906.
- [127] B. Chaudhuri, D. Bhadra, L. Moroni, K. Pramanik, *Biofabrication* **2015**, 7, 015009.
- [128] B. Holmes, X. Fang, A. Zarate, M. Keidar, L. G. Zhang, *Carbon N. Y.* **2016**, 97, 1.
- [129] Z. X. Meng, W. Zheng, L. Li, Y. F. Zheng, *Mater. Sci. Eng. C* **2010**, 30, 1014.
- [130] J. Song, H. Gao, G. Zhu, X. Cao, X. Shi, Y. Wang, *Carbon N. Y.* **2015**, 95, 1039.
- [131] Y. Y. Qi, Z. X. Tai, D. F. Sun, J. T. Chen, H. B. Ma, X. B. Yan, B. Liu, Q. J. Xue, *J. Appl. Polym. Sci.* **2013**, 127, 1885.
- [132] C. Zhang, L. Wang, T. Zhai, X. Wang, Y. Dan, L. S. Turng, *J. Mech. Behav. Biomed. Mater.* **2016**, 53, 403.
- [133] Y. Luo, H. Shen, Y. Fang, Y. Cao, J. Huang, M. Zhang, J. Dai, X. Shi, Z. Zhang, *ACS Appl. Mater. Interfaces* **2015**, 7, 6331.
- [134] O. J. Yoon, C. Y. Jung, I. Y. Sohn, H. J. Kim, B. Hong, M. S. Jhon, N. E. Lee, *Compos. Part A Appl. Sci. Manuf.* **2011**, 42, 1978.
- [135] S. Kumar, D. Azam, S. Raj, E. Kolanthai, K. S. Vasu, A. K. Sood, K. Chatterjee, *J. Biomed. Mater. Res. - Part B Appl. Biomater.* **2016**, 104, 732.
- [136] G. Li, Y. Zhao, L. Zhang, M. Gao, Y. Kong, Y. Yang, *Colloids Surfaces B Biointerfaces* **2016**, 143, 547.
- [137] S. G. Rotman, Z. Guo, D. W. Grijpma, A. A. Poot, *Polym. Adv. Technol.* **2017**, 28, 1233.
- [138] W. Guo, S. Wang, X. Yu, J. Qiu, J. Li, W. Tang, Z. Li, X. Mou, H. Liu, Z. Wang, *Nanoscale* **2015**, 8, 1897.

- [139] S. Dinescu, M. Ionita, A. M. Pandele, B. Galateanu, H. Iovu, A. Ardelean, M. Costache, A. Hermenean, *Biomed. Mater. Eng.* **2014**, *24*, 2249.
- [140] J. Ruan, X. Wang, Z. Yu, Z. Wang, Q. Xie, D. Zhang, Y. Huang, H. Zhou, X. Bi, C. Xiao, P. Gu, X. Fan, *Adv. Funct. Mater.* **2016**, *26*, 1085.
- [141] J. Linares, M. C. Matesanz, M. J. Feito, H. J. Salavagione, G. Martínez, M. Gómez-Fatou, M. T. Portolés, **2016**, *138*, 50.
- [142] S. Kumar, S. Raj, E. Kolanthai, A. K. Sood, S. Sampath, K. Chatterjee, *ACS Appl. Mater. Interfaces* **2015**, *7*, 3237.
- [143] S. Sayyar, E. Murray, B. C. Thompson, S. Gambhir, D. L. Officer, G. G. Wallace, *Carbon N. Y.* **2013**, *52*, 296.
- [144] D. W. Johnson, B. P. Dobson, K. S. Coleman, *Curr. Opin. Colloid Interface Sci.* **2015**, *20*, 367.
- [145] F. Liu, N. A. Hashim, Y. Liu, M. R. M. Abed, K. Li, *J. Memb. Sci.* **2011**, *375*, 1.
- [146] W. Zhu, **2014**, *9*, 859.
- [147] F. E. Ahmed, B. S. Lalia, R. Hashaikeh, *Desalination* **2015**, *356*, 15.
- [148] H. Niu, T. Lin, *J. Nanomater.* **2012**, *2012*, DOI 10.1155/2012/725950.
- [149] S.-L. Liu, Y.-Y. Huang, H.-D. Zhang, B. Sun, J.-C. Zhang, Y.-Z. Long, *Mater. Res. Innov.* **2014**, *18*, S4.
- [150] C. Shuai, P. Feng, C. Gao, X. Shuai, T. Xiao, S. Peng, *RSC Adv.* **2015**, *5*, 25416.
- [151] N. Hilal, A. F. Ismail, C. J. Wright, *Membrane Fabrication*, **2015**.
- [152] G. S. Wang, Z. Y. Wei, L. Sang, G. Y. Chen, W. X. Zhang, X. F. Dong, M. Qi, *Chinese J. Polym. Sci.* **2013**, *31*, 1148.
- [153] M. Mulder, in *Basic Princ. Membr. Technol. Second Ed.*, **1996**.
- [154] M. Mulder, in *Basic Princ. Membr. Technol.*, Kluwer, Dordrecht, **1996**, pp. 54–109.
- [155] B. Subia, J. Kundu, S. C., in *Tissue Eng.*, **2010**, pp. 141–157.
- [156] I. Martin, D. Wendt, M. Heberer, *Trends Biotechnol.* **2004**, *22*, 80.
- [157] G. Vunjak-novakovic, *Tissue Eng. Cartil. Bone Novartis Found. Symp.* **2003**, *249*, 34.
- [158] A. B. Yeatts, J. P. Fisher, *Bone* **2011**, *48*, 171.
- [159] C. H. Lin, S. hui Hsu, C. E. Huang, W. T. Cheng, J. M. Su, *Biomaterials* **2009**, *30*, 4117.
- [160] N. Plunkett, F. J. O'Brien, *Technol. Heal. Care* **2011**, *19*, 55.
- [161] S. Di Loreto, P. Sebastiani, E. Benedetti, V. Zimmitti, V. Caracciolo, F. Amicarelli, A. Cimini, D. Adorno, *In Vitro Cell. Dev. Biol. Anim.* **2006**, *42*, 134.

- [162] A. P. Pêgo, A. A. Poot, D. W. Grijpma, J. Feijen, *J. Biomater. Sci. Polym. Ed.* **2001**, *12*, 35.
- [163] R. A. Redden, R. Iyer, G. M. Brodeur, E. J. Doolin, *Vitr. Cell. Dev. Biol. - Anim.* **2014**, *50*, 188.
- [164] W. Ma, T. Tavakoli, S. Chen, D. Maric, J. L. Liu, T. J. O'Shaughnessy, J. L. Barker, *Tissue Eng. Part A* **2008**, *14*, 1673.
- [165] J. Chen, R. Liu, Y. Yang, J. Li, X. Zhang, J. Li, Z. Wang, J. Ma, *Neurosci. Lett.* **2011**, *505*, 171.
- [166] B. A. Baghbaderani, L. A. Behie, A. Sen, K. Mukhida, M. Hong, I. Mendez, *Biotechnol. Prog.* **2008**, *24*, 859.
- [167] C. A. V. Rodrigues, M. M. Diogo, C. L. da Silva, J. M. S. Cabral, *Biotechnol. Appl. Biochem.* **2011**, *58*, 231.
- [168] S. Morelli, S. Salerno, A. Piscioneri, F. Tasselli, E. Drioli, L. De Bartolo, *Chem. Eng. J.* **2016**, *305*, 69.
- [169] S. Morelli, A. Piscioneri, S. Salerno, C. C. Chen, C. H. Chew, L. Giorno, E. Drioli, L. De Bartolo, *Biofabrication* **2017**, *9*, 025018.
- [170] C. A. Brayfield, K. G. Marra, J. P. Leonard, X. Tracy Cui, J. C. Gerlach, *Acta Biomater.* **2008**, *4*, 244.
- [171] N. Liu, Y. Li, S. T. Yang, *Biochem. Eng. J.* **2013**, *75*, 55.
- [172] M. A. Lancaster, J. A. Knoblich, *Nat. Protoc.* **2014**, *9*, 2329.
- [173] J. Zhao, M. Griffin, J. Cai, S. Li, P. E. M. Bulter, D. M. Kalaskar, *Biochem. Eng. J.* **2016**, *109*, 268.
- [174] N. Salehi-nik, G. Amoabediny, B. Pouran, H. Tabesh, M. A. Shokrgozar, N. Haghighipour, N. Khatibi, F. Anisi, *Biomed Res. Int.* **2015**, *2013*, 15 pages.
- [175] I. D. Sagita, Y. Whulanza, R. Dhelika, I. Nurhadi, **2018**, *040019*, 040019.
- [176] B. C. Thompson, R. T. Richardson, S. E. Moulton, A. J. Evans, S. O'Leary, G. M. Clark, G. G. Wallace, *J. Control. Release* **2010**, *141*, 161.
- [177] J. Huang, X. Hu, L. Lu, Z. Ye, Q. Zhang, Z. Luo, *J. Biomed. Mater. Res. part A* **2009**, *93*, 164.





## *Chapter 2*

### **Fabrication and characterization of porous membranes of poly( $\epsilon$ -caprolactone) with graphene based nanomaterials**

This chapter was adapted from the manuscript published in “Journal of Membrane Science”:



N. Diban, S. Sánchez-González, M. Lázaro-Díez, J. Ramos-Vivas, A. Urtiaga, Facile fabrication of poly( $\epsilon$ -caprolactone)/graphene oxide membranes for bioreactors in tissue engineering, Journal of Membrane Science. 540 (2017) 219–228 [1].



## 2.1. Introduction

As it was mentioned in *Chapter 1*, the non-solvent induced phase separation (NIPS) technique is a versatile and facile method for producing large batches of porous flat membrane scaffolds with potential to be used in tissue engineering applications. Previously, the Environmental Technologies and Bioprocesses research group of the Department of Chemical and Biomolecular Engineering of the University of Cantabria developed poly( $\epsilon$ -caprolactone) (PCL) membranes by NIPS technique [2]. The fabricated PCL membranes showed high porosity and mass transport properties with suitable adherence and proliferation of the neural type cells.

Due to the unique properties of graphene based nanomaterials (GbNs), the development of PCL/GbN membranes was expected to improve the intrinsic properties of the polymer matrix, including mechanical, electrical and thermal properties, nutrient flux, antifouling as well as enhancing the neural cell culture [3–6]. Most experimental works found in journal articles had used electrospinning to fabricate PCL/GbN scaffolds for tissue engineering [7–10]. For instance, Ramazani and Karimi [11] fabricated electrospun composites of PCL with graphene oxide (GO) and reduced graphene oxide (rGO). After, they compared the effects of GbNs loading on the mechanical properties. As a result, they found a critical graphene loading of 0.1 wt% in PCL. In addition to electrospinning, other processing methods to produce polymer/GbN membranes reported the use of extreme temperature conditions, toxic chemicals [9,12] or laborious and time consuming in situ polymerization [13].

The main challenge of the research described in this chapter has been the fabrication of highly porous PCL membranes loaded with GO and rGO to be used in bioreactors for neural tissue regeneration by using the NIPS technique under mild temperatures and with the absence of toxic reductive chemicals. To the best of our knowledge, the use of NIPS technique under mild conditions to produce porous PCL/GbN membranes has not been reported previously. The high porosity of the membranes is key to ensuring the nutrient supply to the cells and to facilitate the migration and colonization of the scaffold by the cells. Meanwhile, the GbN presence in the polymer matrix is used to promote the neural cell differentiation and maturation.

The characterization of the membranes consisted of the evaluation of the morphological, electrical, chemical, mechanical, thermal and mass transport properties. Additionally, the possible formation of PCL/GbN composites was evaluated. The biocompatibility of the membranes was studied through glioblastoma cell cultures. Glioblastoma cells represent the most common and aggressive primary brain tumor and they are characterized by their resemblance to glia [14]. Therefore, they could be used to reproduce an example of *in vitro* brain cancer model, either to study the mechanisms involved in the formed tissue or to test clinical trials. Glial cells are responsible for giving support and assistance to neurons. Glial cells constitute between 33 and 66% of the total brain mass, and they can be subdivided in microglia, astrocytes, and oligodendrocytes [15].

## 2.2. Materials and methods

### 2.2.1. Materials

PCL pellets (Mw, 80 kDa), bovine serum albumin (BSA, A9647, Fraction V,  $p \geq 96\%$ ) and dibasic sodium phosphate ( $\text{Na}_2\text{HPO}_4$ ) were supplied by Sigma Aldrich. Graphite powder (99%) and N-methyl pyrrolidone (NMP, 99%, extrapure) were purchased from Acros Organics. Sulfuric acid (95-98%) ( $\text{H}_2\text{SO}_4$ ), hydrochloric acid (37%) (HCl), potassium permanganate ( $\text{KMnO}_4$ ), sodium nitrate ( $\text{NaNO}_3$ ), sodium chloride (NaCl), potassium chloride (KCl) and potassium dihydrogen phosphate ( $\text{KH}_2\text{PO}_4$ ) were provided by Panreac. Hydrogen peroxide ( $\text{H}_2\text{O}_2$ , 30% v/v) was purchased from Scharlab, and 2-propanol (IPA, 99%) was obtained from Oppac. The aliphatic solvent, Shellshol D70, was supplied by Shell Chemicals. All reagents were used in the same way as they were purchased.

### 2.2.2. Synthesis of GO and rGO

GO was synthesized following a modified Hummer's method [16,17]. First, the graphite powder was oxidized in an acid medium and then, the graphite oxide was exfoliated to separate the nanosheets, forming the GO. Briefly, 3 g of graphite powder, 1.5 g of  $\text{NaNO}_3$  and 70 mL of  $\text{H}_2\text{SO}_4$  were mixed and stirred in an ice bath (Figure 2.1a). Next, 9 g of  $\text{KMnO}_4$  was slowly incorporated to the solution. At a temperature lower than  $35^\circ\text{C}$ , the solution took 20 minutes to oxidize the graphite sheets. After that, 50 mL of ultrapure (UP) water was added, and the temperature reached  $98^\circ\text{C}$  for 15 minutes. Then, 170 mL of UP water and 4 mL of  $\text{H}_2\text{O}_2$  were added to remove the excess of  $\text{KMnO}_4$  and the solution was washed with UP water and HCl to obtain graphite oxide. Finally, the

graphite oxide was exfoliated using ultrasonication (VCX 500, Sonics & Materials, Inc.) for 30 minutes (Figure 2.1b) and centrifuged (Centrifuge 5810, Eppendorf) for 1 h (Figure 2.1c). The final GO powder was dried at 50°C.



**Figure 2.1.** a) Reactor containing the mixture of graphite powder in an acid medium. b) Ultrasonicator is operating to exfoliate the graphite oxide dispersed in UP water. c) Differentiated phases of graphene and graphite oxide, as a result of exfoliation and centrifugation (liquid=GO/water and precipitated solid=graphite oxide). d) Device with the UV light and e) Teflon lined autoclave employed to reduce the GO.

Two different methods were tested to synthesize rGO, including a UV irradiation treatment and a hydrothermal method. First, GO was redispersed in UP water ( $0.5 \text{ mg} \cdot \text{mL}^{-1}$ ) by sonication in both procedures. On the one hand, GO/UP water was exposed to UV light during 48 hours for the UV irradiation treatment and using a UV lamp (365 nm, 6 W, Model EA-160/FE, Spectroline) (Figure 2.1d) [18]. On the other hand, the hydrothermal method was based on an adapted method from Ribao et al. [17], in which GO/UP water dispersion was heated at 200°C for 3 h in

a Teflon lined autoclave (Figure 2.1e). The produced rGO precipitated in both processes and subsequently dried at a temperature of 50°C.

### 2.2.3. Preparation of the PCL-graphene flat membranes

Figure 2.2 presents the schematic process to fabricate three different types of membranes: PCL with GO (PCL/GO), PCL/GO membranes subjected to a post-photoreduction treatment (PCL/GO/UV) and PCL with rGO (PCL/rGO). PCL/GbN membranes were developed by NIPS, following a method by Diban et al. [2] that was adapted. First, a dispersion of GO or rGO in NMP was prepared by sonication for 30 minutes. Subsequently, PCL was added to the nanomaterial dispersion. The polymer solution consisted of PCL (15 w/w%) and GO or rGO nanomaterials (0.1 w/w%, 0.25 w/w% and 1 w/w%), dispersed in NMP. The solution was stirred continuously with a roller shaker (6 Basic, IKA) for 48 hours at 35°C until the polymer solution was completely dissolved. After, the solution was left to stand for 24 hours at room temperature in order to degasify it. The polymer solution was cast on a glass plate through a 0.2 mm slit doctor blade film casting knife. Immediately after, the glass plate was submerged into a coagulation bath composed of IPA 100 v/v%, obtaining PCL/GO and PCL/rGO membranes. Once the polymer precipitation was completed, a new IPA coagulation bath was used for further 24 h to guarantee the total solvent exchange. Finally, membranes were washed by submerging them into UP water baths that were periodically changed for 72 hours. Some PCL/GO membranes were exposed to a UV post-treatment using a UV lamp (Figure 2.1 d) for 48 h so as to reduce the GO contained in PCL/GO membranes, obtaining PCL/GO/UV membranes. Control PCL membranes (15 w/w% PCL in NMP) were also prepared to be compared.

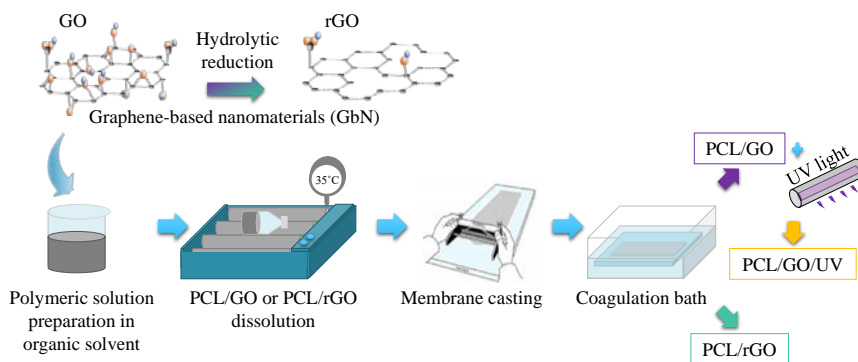


**Figure 2.2.** Scheme of the PCL/GbN membrane fabrication by NIPS technique

#### 2.2.4. Physical characterization of nanomaterials and membranes

Fourier transform infrared (FTIR) spectroscopy (Spectrum 65 spectrometer, Perkin Elmer) with an ATR accessory (GladiATR, PIKE Technologies) was used to characterize the chemical structure of the synthesized nanomaterials and its presence in the membranes.

Raman spectroscopy of the nanomaterials was carried out with a triple spectrometer T64000 (Horiba) equipped with a confocal microscope and a charge coupled device detector (Jobin Yvon Symphony) cooled with liquid nitrogen. A 514 nm wavelength beam from a Krypton-argon ion laser was focused with a 100× objective for detection and an effective laser power of 2mW was employed for all measurements. The elapsed time at which the experiment was carried out and the number of accumulations varied depending on the sample tested. Each band from the spectral curves was fitted with Lorentzian functions (Origin 6.0, OriginLab Corporation).

Cyclic voltammetry curves were performed using a Potentiostat/Galvanostat instrument (AUTOLAB, PGSTAT12). Figure

2.3 shows the procedure to execute the measurements. Briefly, two copper wires were placed on the surface of the membrane at a maximum distance of 0.5 cm between each other. The copper wires were also connected to alligator clips to allow the current flux. The system was covered to avoid any single movement of the wires. Measurements were accomplished by a scan rate of  $80 \text{ mV}\cdot\text{s}^{-1}$  over the potential range from +2.0 to -2.0 V. The results were collected by the software Nova 1.9.16 (MetrohmAutolab B.V.).

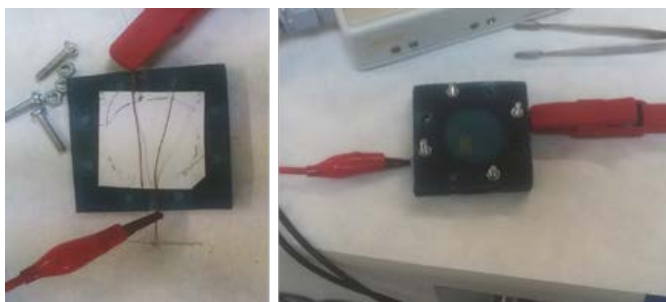


**Figure 2.3.** Arrangement of the membrane sample to develop cyclic voltammetry curves.

The resistivity  $R$  ( $\Omega\cdot\text{cm}$ ) was determined by Equation 2.1.

$$R = \frac{V \cdot A_m}{I \cdot D_e} \quad (2.1)$$

where  $V$  is the applied potential (V),  $I$  the current intensity (A),  $A_m$  the membrane area ( $3.3 \times 3.3 \text{ cm}^2$ ) and  $D_e$  the distance between the two electrodes (0.5 cm). The number of analyzed samples for each membrane type was  $n \geq 3$ .

Scanning electron microscopy (SEM) images of the different membranes were taken to study the structure and morphology of the surface and cross section. SEM images were carried out using a Carl

Zeiss EVO MA 15, at an acceleration voltage of 20kV. To prepare cross-section samples, membranes were submerged in liquid nitrogen to be fractured. All samples were kept overnight at 30°C under vacuum and were gold sputtered before examination.

The viscosity of the polymeric solutions was measured using a rotational viscometer (Fungilab, Alpha Series). The spindle type and volume used were selected depending on the expected viscosity range.

Membrane thickness ( $\delta$ ) was measured using an electronic micrometer (Standard, Series 293, Mitutoyo) with an average error of 0.001 mm.

The porosity of the membranes ( $\varepsilon$ ) was analyzed via gravimetric method [2]. Samples were cut into squares of 3 cm in length and dried in a vacuum oven at 30°C overnight. Dry samples were weighted ( $W_2$ ) and subsequently submerged in Shellshol D70 (aliphatic solvent) for 24h. After removing the excess of solvent with a tissue paper, samples were weighted again ( $W_1$ ). Finally,  $\varepsilon$  was calculated using Equation 2.2:

$$\varepsilon = \left( \frac{W_1 - W_2}{\rho_{solv}} \right) / \left( \frac{W_1 - W_2}{\rho_{solv}} + \frac{W_2}{\rho_{PCL}} \right) \times 100 \quad (2.2)$$

Where  $\rho_{solv}$  is the density of Shellshol D70 (0.8 g·cm<sup>-3</sup> at 25°C) and  $\rho_{PCL}$  is the density of PCL (1.145 g·cm<sup>-3</sup> at 25°C) [28]. The measurements were done in triplicate. Additionally, the surface porosity  $\varepsilon_s$ , and the pore diameter  $d$  of the membranes were quantified from the surface and cross section SEM images using Fiji (ImageJ) software.

Thermal gravimetric analysis (TGA) was developed with a DTG-60H thermobalance (Shimadzu). TGA was carried out under nitrogen

atmosphere using samples of 5-10 mg, at a heating rate of  $10^{\circ}\text{C}\cdot\text{min}^{-1}$  from room temperature to  $650^{\circ}\text{C}$ .  $T_{onset}$  and  $T_{max}$  were obtained from the TGA profiles.

DSC-131 instrumentation (SETARAM Instrumentation) was used to analyze the differential scanning calorimetry (DSC) of the membranes. Samples from 5 to 10 mg were heated from room temperature to  $100^{\circ}\text{C}$  at a rate of  $10^{\circ}\text{C}\cdot\text{min}^{-1}$ . After a stabilization period in which membranes were stored for 10 minutes at  $100^{\circ}\text{C}$ , samples were cooled down from  $100^{\circ}\text{C}$  to  $0^{\circ}\text{C}$  at  $10^{\circ}\text{C}\cdot\text{min}^{-1}$ . Also, they stabilized for 10 minutes at  $0^{\circ}\text{C}$  and finally heated again to  $100^{\circ}\text{C}$ . The temperature of crystallization ( $T_c$ ) is obtained in the first ramp of cooling, while the melting temperature ( $T_m$ ) is defined by the second heating ramp. The degree of crystallinity,  $\chi_c$  (%), was calculated using Equation 2.3 [25]:

$$\chi_c = \frac{\Delta H_m}{(1 - \beta) \cdot \Delta H_m^0} \quad (2.3)$$

where  $\beta$  is the mass fraction of GO or rGO in the PCL membrane,  $\Delta H_m$  is the sample melting enthalpy from the second heating ramp and  $\Delta H_m^0$  is the melting enthalpy for 100% crystalline PCL ( $139.5 \text{ J}\cdot\text{g}^{-1}$  [25]).

Mechanical properties of the membranes were evaluated through axial tensile tests (Figure 2.4). Experiments were carried out on a servo-hydraulic testing universal machine (SERVOSIS, ME-400) using samples of  $40 \times 6 \text{ mm}^2$  and a load cell capacity of 1.25 kN. A constant speed of  $8 \text{ mm}\cdot\text{s}^{-1}$  was employed, taking into account the ISO standard for thin plastic membranes (ASTM D882- 12). The average values of the tensile properties were obtained from two replicates.

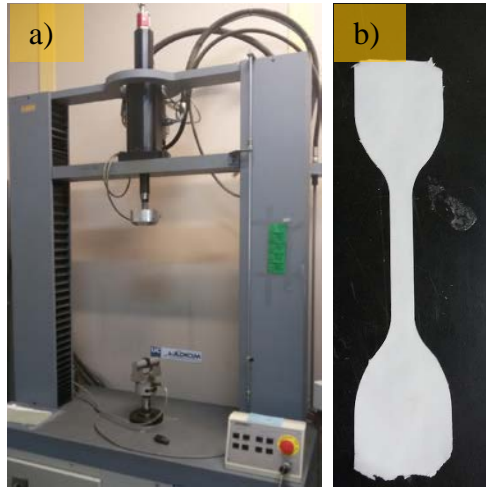


**Figure 2.4.** a) Servo-hydraulic testing universal machine. b) Membrane sample before testing ( $40 \times 6 \text{ mm}^2$ ).

### 2.2.5. Determination of glucose diffusion coefficient

The diffusivity of glucose was experimentally determined across the PCL/rGO scaffold using a diffusion cell (Figure 2.5). The diffusion cell consisted of two equal cylindrical compartments ( $\varnothing = 6.5 \text{ cm}$ ,  $h = 8.2 \text{ cm}$ ) that were connected by the PCL/rGO membrane with an effective area ( $A_G$ ) of  $15.9 \text{ cm}^2$ . One of the compartments, the donor chamber, was filled with 280 mL of  $5 \text{ g}\cdot\text{L}^{-1}$  of D-glucose (Sigma Aldrich,  $\geq 95\%$ , powder) dissolved in UP water, whereas the other compartment, the acceptor chamber, was only filled with 280 mL of UP water. Both compartments were stirred at 2 rpm to facilitate the diffusion. Samples of 0.4 mL were daily taken simultaneously from both compartments, until the solutions reached equilibrium. The experiment was conducted at room temperature, instead of being at  $37 \text{ }^\circ\text{C}$ , to minimize solvent evaporation. Before the experiment, the PCL/rGO membranes were immersed in a 70% ethanol/water solution for one day.

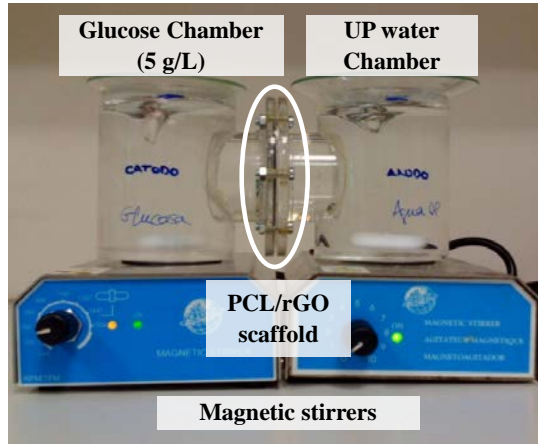


**Figure 2.5.** Diffusion cell with donor and acceptor compartments, connected by the PCL/rGO membrane.

The glucose concentration ( $C_{Gi}$ ) was measured with the Glucose GOD-PAP lab kit (Biolabo SAS). The sample was prepared following the steps of the manufacturer protocol using a reagent composed of phosphatase buffer  $150 \text{ mmol}\cdot\text{L}^{-1}$ , glucose oxidase  $20000 \text{ U}\cdot\text{L}^{-1}$ , peroxidase  $10000 \text{ U}\cdot\text{L}^{-1}$ , 4-aminoantipyrine  $0.8 \text{ mmol}\cdot\text{L}^{-1}$  and chlorophenol  $2 \text{ mmol}\cdot\text{L}^{-1}$ . The light absorbance (ABS) of the samples was measured by UV-vis spectroscopy at 500 nm. The quantification of glucose concentration was calculated through Equation 2.4 as:

$$C_{Gi} (\text{g} \cdot \text{L}^{-1}) = \frac{ABS \text{ sample}}{ABS \text{ standard}} \cdot [C_{st}] \quad (2.4)$$

where  $i$  is equal to the donor ( $g$ ) or the acceptor ( $w$ ) compartment and  $[C_{st}]$  the standard of glucose with a concentration of  $1 \text{ g}\cdot\text{L}^{-1}$ .

The effective diffusion coefficient of glucose across the PCL/rGO membrane ( $D_{G,eff}$ ,  $\text{m}^2\cdot\text{s}^{-1}$ ) was calculated from the experimental test of diffusion [19,20]. The corresponding diffusion coefficient is based on the Fick's first law of diffusion, as (Equation 2.5):

$$D_{G,eff} = J_G \cdot \delta / \Delta C \quad (2.5)$$

where  $\Delta C$  is the concentration glucose gradient between the donor ( $C_{Gg}$ ) and the acceptor compartment ( $C_{Gw}$ ). Furthermore,  $J_G$  ( $\text{g} \cdot \text{m}^{-2} \cdot \text{h}^{-1}$ ) is the glucose diffusional flux, which was calculated using Equation 2.6:

$$J_G = C_{Gw} \cdot V_w / A_G \cdot t \quad (2.6)$$

where  $V_w$  (mL) is the volume of the acceptor compartment and  $t$  (s) the time of sample collection.

The  $D_{G,eff}$  is also defined by the porosity and tortuosity ( $\tau_m$ ) of the porous membranes, as it is expressed in the equation below (Equation 2.7):

$$D_{G,eff} = D_G \cdot \varepsilon / \tau_m \quad (2.7)$$

where  $D_G$  is the diffusion coefficient in free media ( $6.9 \times 10^{-10} \text{ m}^2 \cdot \text{s}^{-1}$  [21]).

Results from two replicates were presented as the mean values  $\pm$  average deviation.

## 2.2.6. Membrane flux characterization

Figure 2.6 presents a homemade tangential flow filtration system that was employed to characterize the hydraulic and model nutrients flux across the membranes. An electrically heated feed reservoir was used to maintain the feed solution temperature at 37°C. The feed solution was pumped at a flow rate of 93  $\text{mL} \cdot \text{min}^{-1}$  through the filtration module with

an effective filtration area ( $A_e$ ) of 10 cm<sup>2</sup>. The permeate stream was collected and its mass was continuously recorded by a balance connected to a computer. The retentate stream was recirculated to the feed reservoir. A valve located at the outlet port of the retentate side of the membrane holder allowed the system to regulate the feed pressure. The permeate compartment was kept at atmospheric pressure.

The hydraulic permeance was measured using UP water as supply. Membranes were previously stabilized at a pressure of 0.20 bar during 1-1.5 h. After that, pressure was fixed at different points working with up-down pressure cycles (0.05 to 0.20 bars). Similarly, a model aqueous solution of the protein BSA (0.40 g·L<sup>-1</sup>) in a phosphate buffer solution (PBS, pH 7.4) was used to determine the nutrient permeance. First, membranes were preconditioned with UP water at 0.10 bar during 1 h. Later, the BSA solution was circulated through the filtrate system working at 0.10 bar and 37°C during 4 h.

PBS was prepared in the following way: 8.00 g of NaCl, 0.20 g of KCl, 1.44 g of Na<sub>2</sub>HPO<sub>4</sub> and 0.24 g of KH<sub>2</sub>PO<sub>4</sub> were solubilized in 800 ml of distilled water. Afterwards, the pH was adjusted to 7.4 with HCl (0.10 mol·L<sup>-1</sup>) and made up to 1 L with distilled water.

Volumetric total hydraulic flux  $J_w$  (L·m<sup>-2</sup>·h<sup>-1</sup>) and total nutrient flux  $J_t$  (L·m<sup>-2</sup>·h<sup>-1</sup>) were calculated at each pressure point according to Equation 2.8.

$$J_j = \frac{W_{permeated} \cdot \rho_{37^\circ C}}{\Delta t \cdot A_e} \quad (2.8)$$

where  $j$  is equal to water or nutrient depending on the feed,  $W_{permeated}$  (g) is the collected permeate mass,  $\rho_{37^\circ C}$  (g·m<sup>-3</sup>) is the density of the fluid,  $A_e$

( $m^2$ ) is the effective membrane surface area and  $\Delta t$  (h) is the time period of permeate collection.

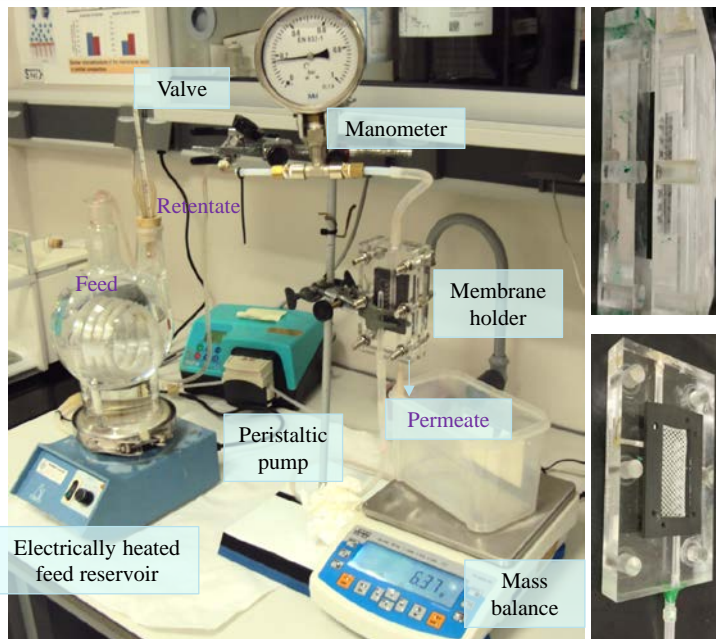
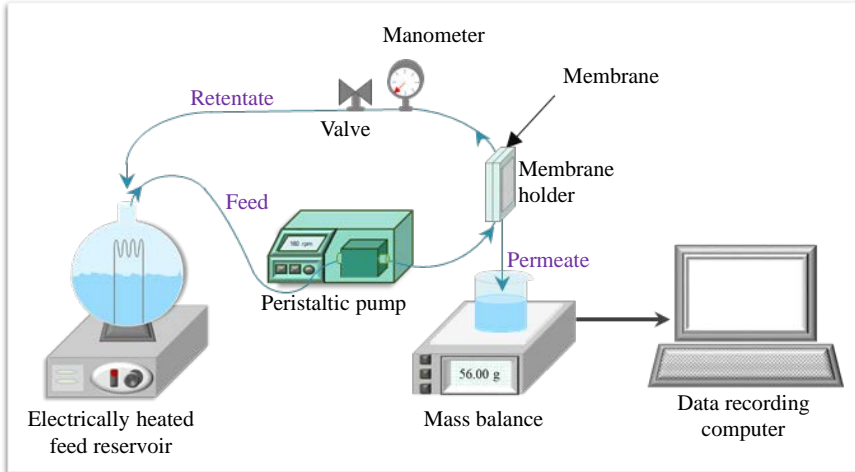


**Figure 2.6.** Homemade cross-flow filtration system shown a) as a scheme, for the sake of clarity and b) during the experimental procedure in the laboratory, indicating each component.

The hydraulic  $P_w$  and nutrient permeance  $P_t$  ( $L \cdot m^{-2} \cdot h^{-1} \cdot bar^{-1}$ ) were determined using the slope of the flux vs. pressure ( $\Delta P$ ) plot according to Equation 2.9:

$$P_j = \frac{J_j}{\Delta P} \quad (2.9)$$

For nutrient flux tests, the BSA rejection ( $R_{BSA}$ , %) was calculated using Equation 2.10:

$$R_{BSA} = \left( 1 - \frac{C_{BSA}^p}{C_{BSA}^f} \right) \times 100 \quad (2.10)$$

Samples from feed and permeate streams were taken periodically and the BSA concentration ( $C_{BSA}^f$  ( $mg \cdot L^{-1}$ ) and  $C_{BSA}^p$  ( $mg \cdot L^{-1}$ ), respectively) was measured by UV spectroscopy (UV-1800 Shimadzu) at 280 nm. Permeation tests were done twice to evaluate each type of membrane. Data were presented as the mean values  $\pm$  average deviation.

### 2.2.7. Biocompatibility tests and static cell cultures on membranes

Cell proliferation tests were carried out to study the biocompatibility of the membranes by using the U87 human glioblastoma cell line (ATCC<sup>®</sup> HTB-14<sup>™</sup>). Firstly, U87 human glioblastoma cells were cultured for expansion on a Roux flask of 75 cm<sup>2</sup>. Secondly, they were maintained in a humidified atmosphere of 5% carbon dioxide and 95% air at 37°C until 80-90% confluence (Figure 2.7a). Thirdly, cells from the Roux flask were trypsinized and resuspended in the culture medium. Lastly, cells were seeded on the sterilized membranes at a density of  $1 \times 10^4$  cells  $\cdot mL^{-1}$ ; they were kept in 6-well plates (Corning, Inc.) in a humidified atmosphere of 5% carbon dioxide and 95% air at 37 °C for up

to 21 days (Figure 2.7b-d).

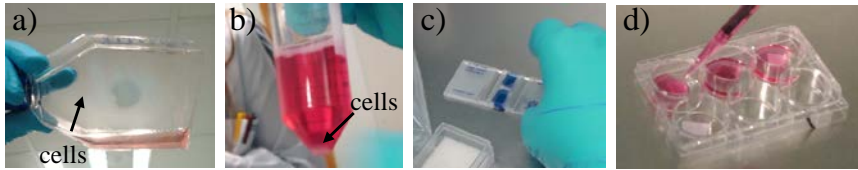


**Figure 2.7.** a) Expanded cells adhered to the flask wall. b) Cells deposited at the bottom of the flask after being trypsinized and centrifuged. c) NeuBauer chamber used to count the number of cells. d) Cell seeding on the membrane samples.

Membrane samples were sterilized by soaking in 70% ethanol for 5 minutes. The culture medium was composed of Dulbecco's-modified Eagle's (DMEM, Gibco Invitrogen) supplemented with 10% calf serum, antibiotic agents (penicillin G ( $100 \text{ U}\cdot\text{mL}^{-1}$ ) and streptomycin ( $100 \text{ mg}\cdot\text{mL}^{-1}$ ). The composition of the culture medium is detailed in Appendix A.

Confocal microscopy images of inverted membrane samples were taken using a Nikon A1R confocal scanning laser microscope (Nikon Corporation) with a Plan Apo VC 20X DIC N2 objective equipped with a 561 nm laser. Membranes with cells were preconditioned before analysis. First, cells were fixed using cold 3% paraformaldehyde solution in PBS for 20 minutes at room temperature. Later, cells were permeabilized with 0.1% X-100 in PBS for 5 minutes at room temperature, and washed three times with PBS. Finally, cells were stained using fluorescent-labelled phalloidin (Atto-590, Sigma Aldrich), which is a protein that identifies the actin filaments, the most abundant protein of eukaryotic cells [22]. Image analysis was carried out by NIS Elements 3.2 software.

## 2.3. Results and discussion

### 2.3.1. Nanomaterial characterization

Figure 2.8 shows the chemical structure of the synthesized GO and rGO nanomaterials using a) FTIR-ATR and b) Raman spectroscopy. Figure 2.8a presents the FTIR-ATR spectra of the synthesized GO and rGO produced both by UV irradiation treatment and through the hydrothermal method. GO displayed many strong absorption bands related to oxygen functional groups, which are representative of the nanomaterial. Bands at  $3551\text{ cm}^{-1}$  and  $1630\text{ cm}^{-1}$  corresponded to the stretching vibration of the hydroxyl groups (-OH) and the skeletal vibration from unoxidized graphitic domains (C=C), respectively. The stretching vibrations of oxygen were assigned at 1718, 1312, 1152 and  $1026\text{ cm}^{-1}$  by carboxyl (C=O), carboxyl (C-O), epoxy (C-O) and alkoxy (C-O) groups, respectively [23,24]. The FTIR spectrum of rGO was defined by the absence of the characteristic transmittance bands of the oxygenated groups, in comparison to GO, demonstrating the suitable reduction of the nanomaterial [18]. The hydrothermal method was selected to reduce the GO nanomaterial before the fabrication of the membrane (PCL/rGO). Meanwhile, UV irradiation was used to reduce the GO already contained in the PCL/GO membranes (PCL/GO/UV).

The Raman spectra of GO and rGO (from hydrothermal method) (Figure 2.8b) indicated two representative bands of the nanomaterials, the G band at  $1580\text{--}1600\text{ cm}^{-1}$  and the D band at  $1350\text{ cm}^{-1}$ . The G band arose from the primary in-plane vibration mode of graphene, whereas the D band matched with defects of graphene and disordered carbon [23]. The partial reduction of GO was confirmed by the clear reduction in

absorbance of rGO. Also, the D/G intensity ratio of GO and rGO nanomaterials were calculated to retrieve information about the reduction of the GO nanomaterial [25]. The D/G intensity ratio decreased from 0.96 in GO to 0.28 in rGO, confirming the GO reduction.

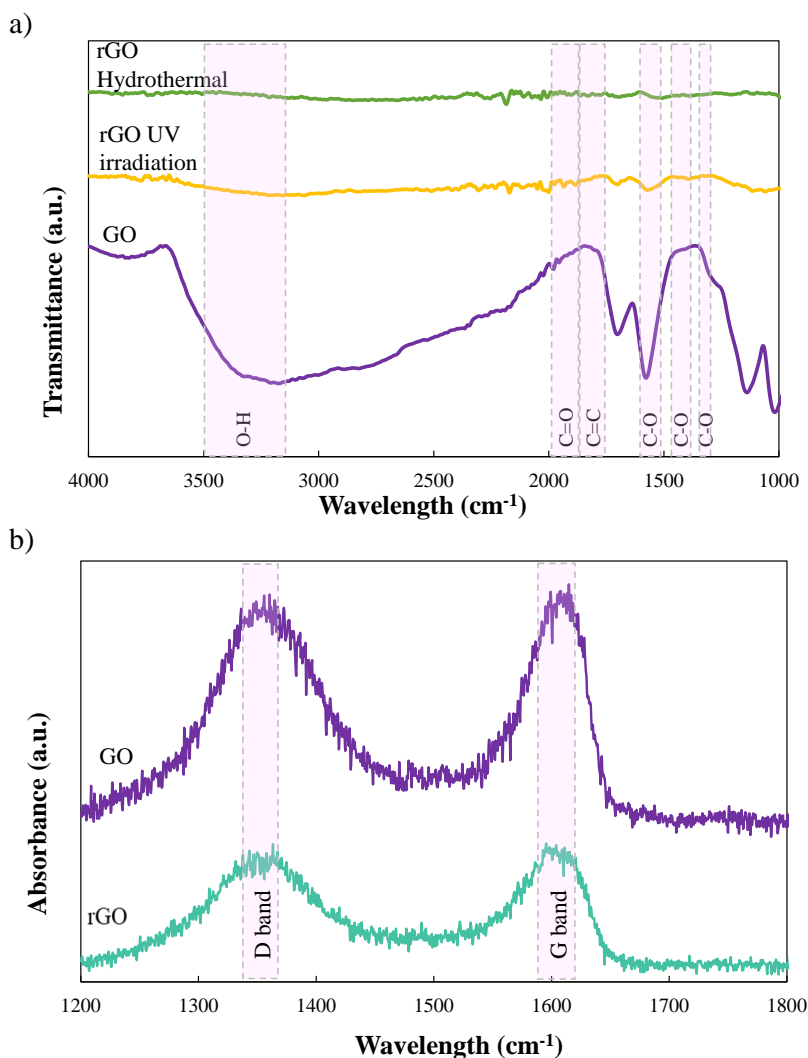
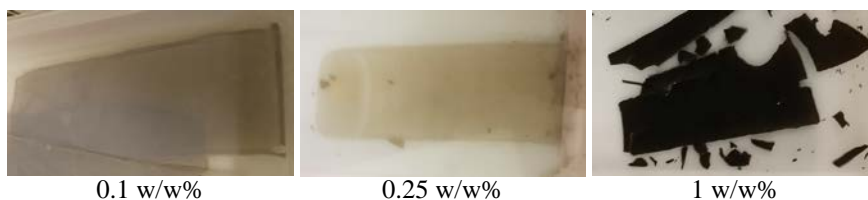


**Figure 2.8.** Chemical structure of GO and rGO, showing the representative bands of the nanomaterials, using a) FTIR-ATR and b) Raman spectroscopy.

Furthermore, the 2D band of the Raman spectra can give useful information regarding the number of layers of the graphene sheets through the 2D/G ratios. The definition of single-, double-, triple- and multi- (>4) layer graphene sheets corresponded to 2D/G ratio values above 1.60, ~0.80, ~0.30 and ~0.07, respectively [25]. The 2D band was located at 2835-2847  $\text{cm}^{-1}$  (data not shown) and the 2D/G ratios of GO and rGO were similar to values of 0.21 and 0.24 respectively, which were attributed to 3-4 layers.

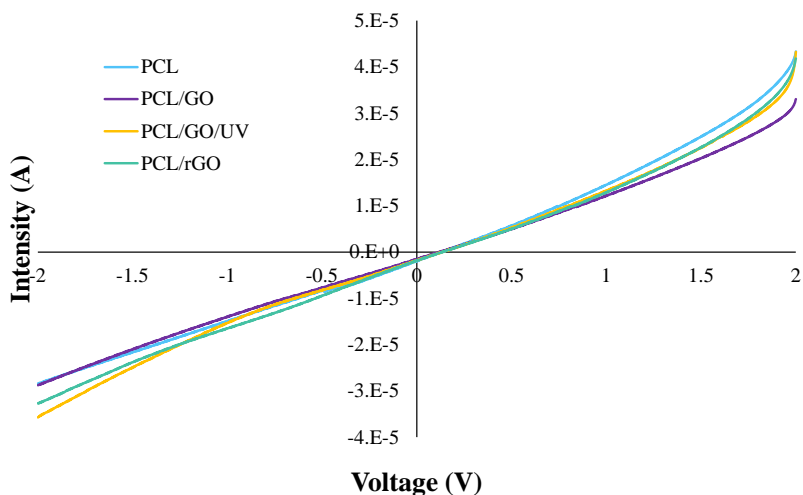
### 2.3.2. Physical characterization of the membranes

Figure 2.9 shows the fabricated membranes of PCL with different concentrations of GO nanomaterials (0.1 w/w%, 0.25 w/w% and 1 w/w%). Membranes with GO loads above 0.1 w/w% were too brittle, difficult to handle and/or mechanically unstable. Therefore, only membranes at concentrations of 0.1 w/w% were tested to be used in bioreactors for neural tissue regeneration.



**Figure 2.9.** Membrane fabrication of PCL and different GO concentrations.

Figure 2.10 presents the voltammetry curves of the PCL membranes and PCL/GbN membranes at 0.1 w/w%. The superficial electrical resistivity of the membranes was  $1.28 \times 10^6 \pm 2.46 \times 10^5 \Omega \cdot \text{cm}$  in plain PCL,  $1.32 \times 10^6 \pm 1.47 \times 10^5 \Omega \cdot \text{cm}$  in PCL/GO,  $1.22 \times 10^6 \pm 1.36 \times 10^5 \Omega \cdot \text{cm}$  in PCL/GO/UV and  $1.45 \times 10^6 \pm 2.55 \times 10^5 \Omega \cdot \text{cm}$  in PCL/rGO.



**Figure 2.10.** Cyclic voltammetry curves of PCL, PCL/GO, PCL/GO/UV and PCL/rGO membranes.

Overall, the resistivity of the membranes did not significantly vary when loads of 0.1 w/w% of GO or rGO were incorporated. Consequently, the concentration used was insufficient to result in conductive behavior. According to other works, the enhancement of the polymeric scaffolds electrical conductivity was achieved with increasing loadings of graphene [6,26]. However, the amount of additive to turn a material from insulator to conductor, known as percolation threshold, depends on the processing method, polymer matrix and filler type [27,28].

Figure 2.11 presents the morphology of the different membranes by SEM images of the cross section and surface and Table 2.1 collects the measurements of the thickness and porosity of the membranes. Qualitatively (Figure 2.11), the porosity of the membranes showed the characteristic internal porous sponge-like structure with a relatively dense top layer. All the PCL/GbN membranes presented high internal porosity with interconnected pores, which were similar to plain PCL membranes.

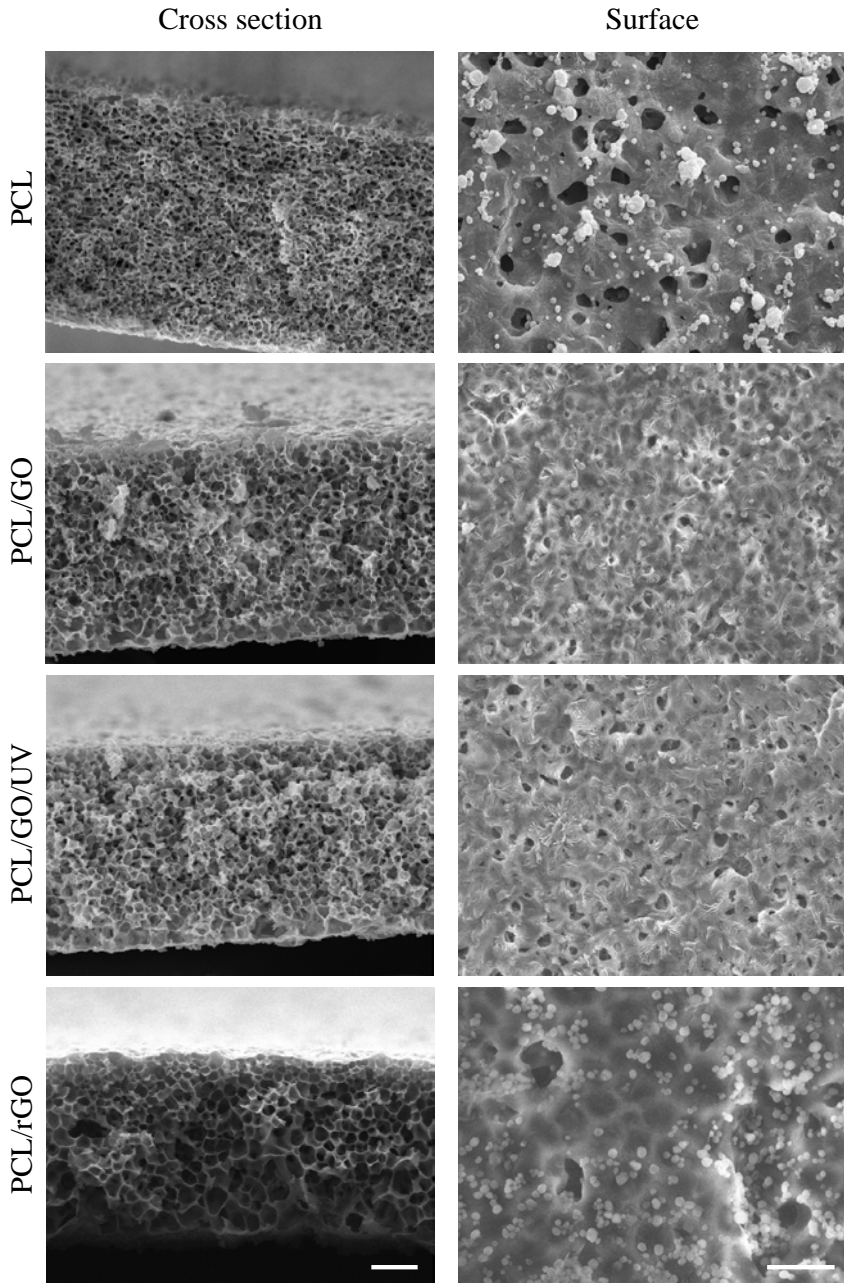


**Figure 2.11.** SEM images of the surface and cross section of the PCL and PCL/GbN membranes. The scale bar was 20  $\mu\text{m}$ .

On the contrary, when plain PCL membranes were compared, PCL/GbN membranes showed noticeable reduced porous surface. Besides, the surface of the membranes presented polymeric semi-spherical particles. These particles were scattered all over the surface in accordance to previous results by Diban et al. [2], being more notable in PCL and PCL/rGO membranes. Regarding the internal morphology of the membranes, the PCL, PCL/GO and PCL/GO/UV membranes exhibited similar symmetric and uniform porosity [2,29]. However, the symmetric pores throughout the thickness of PCL/GO and PCL/GO/UV membranes were larger with respect to the plain PCL membranes. On the contrary, PCL/rGO had an asymmetric porosity and the pore size gradually enlarged from the top to the bottom of the membrane.

**Table 2.1.** Morphological parameters of PCL and PCL/GbN membranes. The statistical significance (\$) with  $p < 0.05$  was calculated using one-way ANOVA test, considering PCL as the reference.

Membrane	PCL	PCL/GO	PCL/GO/UV	PCL/rGO
Thickness $\delta$ ( $\mu\text{m}$ )	$91 \pm 5$	$85 \pm 6$	$83 \pm 1$	$97 \pm 8$
Bulk porosity $\varepsilon$ (%)	$81 \pm 1$	$76 \pm 1$ (\$)	$77 \pm 1$ (\$)	$80 \pm 1$
Surface porosity $\varepsilon_s$ (%)	$40 \pm 4$	$9 \pm 1$ (\$)	$22 \pm 2$	$13 \pm 2$ (\$)
Pore diameter $d$ ( $\mu\text{m}$ )	$1.3 \pm 0.6$	$2.7 \pm 1.3$ (\$)	$2.9 \pm 1.0$ (\$)	$4.3 \pm 1.7$ (\$)

The incorporation of GbN inside the polymer matrix did not remarkably affect the thickness and the bulk porosity in comparison to the plain PCL, which were maintained in the range of 83-97  $\mu\text{m}$  and 75-80%, respectively (Table 2.1). In contrast, the average diameter of internal pore was significantly higher in the membranes with GbN (2.7-

4.3  $\mu\text{m}$ ) in comparison to the plain PCL membranes (1.3  $\mu\text{m}$ ). Furthermore, the surface porosity indicated a significant reduction in membranes with GbN (9-22%) with respect to the plain PCL membranes (40%).

In spite of the pore surface reduction, the fabricated membranes were classified as microfiltration materials, typically in the range of pore size 0.1-10  $\mu\text{m}$ . Additionally, microfiltration membranes are defined by high nutrient transport properties and low pore blockage [30,31]. The porous internal structure of the membranes was produced due to the slow exchange between the solvent and non-solvent during the phase-inversion technique, as the non-solvent had low miscibility with the solvent [32]. The greater internal pore sizes and less porous surfaces presented in PCL/GbN, in comparison to plain PCL membranes, were attributed to a faster demixing process during the NIPS processing [32–34]. The fast demixing process could be attributed to the viscosity reduction of the polymer solutions. The pristine PCL solution had a viscosity of 4900 cP, whereas this property decreased to 2900 and 2800 cP when 0.1 w/w% of GO and rGO was introduced in the polymer solution, respectively.

FTIR-ATR spectra of the different membranes are presented in Figure 2.12. PCL spectrum was identified by strong bands, including the ester bond (C=O) at 1725  $\text{cm}^{-1}$  and the stretching  $-\text{CH}_2-$  vibrational peaks at 2945 and 2865  $\text{cm}^{-1}$ . The bands at 1240 and 1170  $\text{cm}^{-1}$  corresponded to C-O-C stretching bonds and the bands at 1294 and 1157  $\text{cm}^{-1}$  were assigned to the C-O and C-C stretching vibration in the crystalline and amorphous phase of PCL [35]. Similarly, PCL/rGO membranes only showed the representative bands of the polymer, as rGO did not show any transmittance in the spectrum (Figure 2.8). The spectra of PCL/GO and

PCL/GO/UV membranes indicated the characteristic bands of PCL as well as of the nanomaterial (Figure 2.8). PCL/GO/UV presented a reduced intensity of the unoxidized graphitic domains (C=C) at  $1630\text{ cm}^{-1}$ , when comparing with PCL/GO. This reduction could be attributed to a partial reduction of GO and it may also indicate a chemical bonding formation between graphene and PCL.

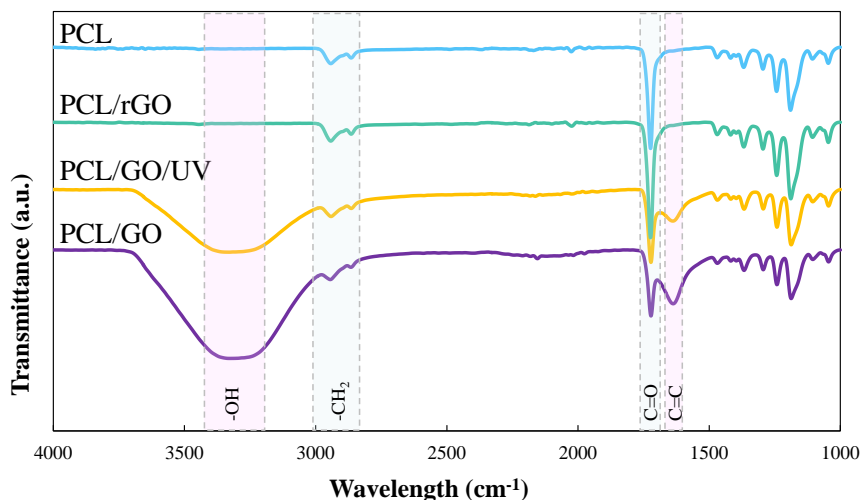


**Figure 2.12.** FTIR-ATR spectra of PCL and PCL/GbN membranes, showing some characteristic bands of PCL (blue) and GO (pink).

Figure 2.13 depicts the thermal properties of the PCL and PCL/GbN membranes by a) DSC thermograms and b) TGA curves. Additionally, table 2.2 summarizes the data collected from both techniques.

DSC analyses indicated that the crystallization temperature ( $T_c$ ) and the degree of crystallinity ( $\chi_c$ ) of membranes with GbN increased in comparison to the plain PCL membrane (Figure 2.13a and Table 2.2). Meanwhile, the melting temperature ( $T_m$ ) remained constant for all 4 types of membranes.

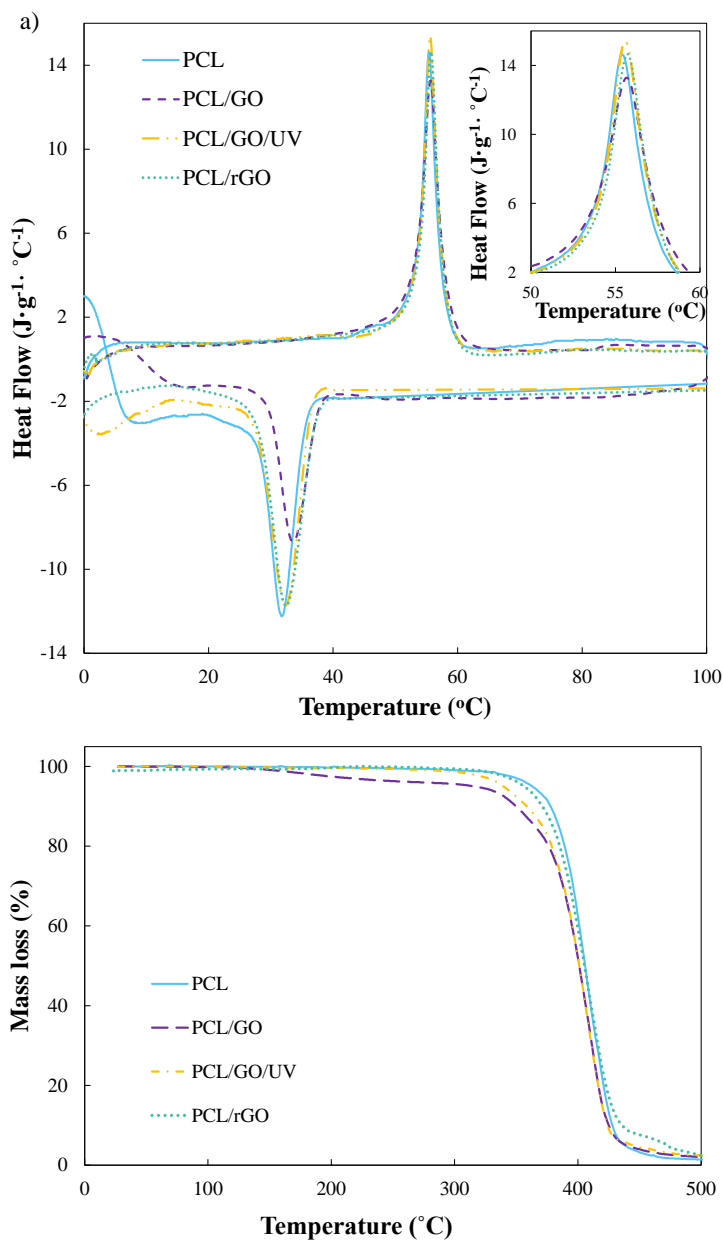


**Figure 2.13.** a) Thermal gravimetric curves from DSC thermograms and b) TGA profiles of PCL and PCL/GbN membranes. The inset in (a) shows a magnification of the melting temperature measured during the second heating ramp.

**Table 2.2.** Thermal properties obtained from the cooling and second heating ramp of the DSC and from TGA of the different membranes.

Membrane	PCL	PCL/GO	PCL/GO/UV	PCL/rGO
$T_c$ (°C)	31.75	33.58	32.35	32.45
$\Delta H_c$ (J/g)	-70.72	-62.93	-56.37	-59.89
$T_m$ (°C)	55.36	55.60	55.59	55.73
$\Delta H_m$ (J/g)	48.88	61.21	48.90	57.06
$\chi_c$ (%)	35.04	44.17	35.29	41.18
$T_{onset}$ (°C)	$272 \pm 9$	$291 \pm 11$	$290 \pm 1$	$319 \pm 4$
$T_{max}$ (°C)	$409 \pm 1$	$411 \pm 1$	$405 \pm 5$	$411 \pm 1$

The higher  $T_c$  and  $\chi_c$  were associated to the nucleating effect produced by GbN. In particular, the slight improvement of  $T_c$  in the PCL/GO membranes could be attributed to van der Waals interactions between PCL and GO [11]. On the contrary, the  $\chi_c$  of the PCL/GO/UV membranes decreased with respect to PCL/GO. In other works, the exposure of UV light through plain PCL membranes produced photodegradation of the amorphous phase of the polymer, leading to an increase of  $\chi_c$  [36,37]. Nevertheless, Campos et al. [36] observed a reduction of  $\chi_c$  in a range of 25-60% in PCL/sisal fibers exposed to a UV phototreatment for 6 days. They attributed the reduction of  $\chi_c$  to the breakdown of the crystalline phase of the PCL chains.

Figure 2.13b shows the thermal stability of the different membranes. The TGA profile provides two characteristic temperatures,  $T_{onset}$  and  $T_{max}$  (Table 2.2).  $T_{onset}$  is known as the temperature in which the material starts to degrade. Meanwhile,  $T_{max}$  is the temperature that provides the fastest degradation rate [38]. The introduction of GbN in PCL membranes

implied very little effect on the decomposition temperature of PCL. The membranes presented a monotonic weight loss in the range of 272-319 °C due to the decomposition of the polymer chains [12]. However, the decomposition of PCL/rGO membranes started later ( $T_{onset}$ ), suggesting that rGO displayed some thermal stability [39]. Moreover, PCL/GO membranes presented a slight weight loss around 200°C, which could be ascribed to the removal of absorbed moisture and residual solvent traces (boiling point of NMP = 202 °C) [40].

Figure 2.14 and Table 2.3 show the mechanical properties of the membranes. As compared to the plain PCL membranes, the presence of GbN in the PCL matrix did not affect significantly the values of elastic modulus and yield stress. However, the membranes with GbN increased their brittleness at the point of rupture, as its ultimate strain was lower than in the plain PCL membranes.

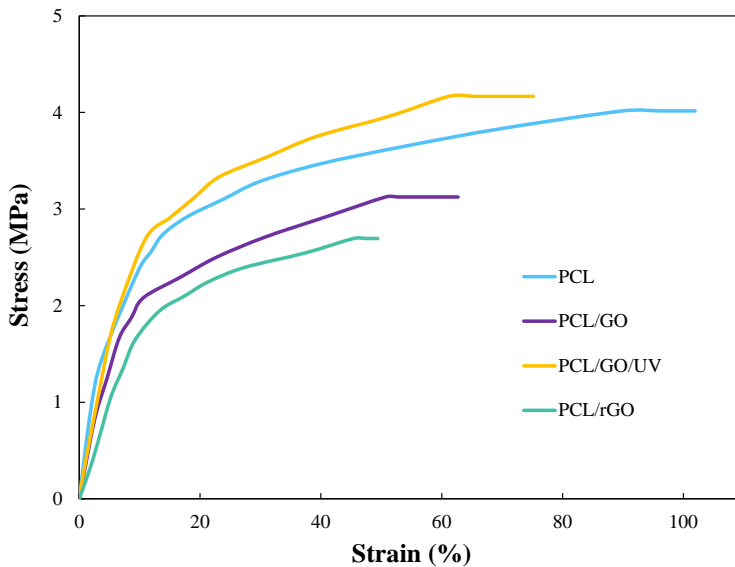


**Figure 2.14.** Axial tensile stress-strain curve of PCL and PCL/GbN membranes.

**Table 2.3.** Mechanical parameters of PCL, PCL/GO, PCL/GO/UV and PCL/rGO membranes, obtained from the axial tensile analyses.

Membrane	PCL	PCL/GO	PCL/GO/UV	PCL/rGO
Young's modulus (MPa)	23.9 ± 1.9	27.2 ± 2.1	24.0 ± 3.4	16.7 ± 1.5
Ultimate tensile stretch (MPa)	2.9 ± 0.2	2.5 ± 0.5	2.9 ± 0.2	1.8 ± 0.1
Yield point (MPa)	3.8 ± 0.2	3.7 ± 0.6	4.4 ± 0.2	2.5 ± 0.2 (§)
Ultimate strain (%)	100.5 ± 1.5	69.1 ± 6.5 (§)	93.5 ± 18.5	51.1 ± 1.7 (§)

Similar results were observed in PCL/graphene composites fabricated by mixing and covalent chemical bonding [12,13]. According to Wang et al. [13], the reduction of the ultimate elastic modulus could be associated to a restriction of the PCL chains movement, due to the presence of the GbN inside the polymer matrix. Moreover, PCL/GO/UV presented higher elongation at break than PCL/GO that may indicate the presence of certain chemical bonds between PCL and GO in accordance with results observed in FTIR-ATR analyses.

### 2.3.3. Glucose diffusion coefficient

Figure 2.15 features the variation of glucose concentration in the donor and acceptor compartments of the diffusion cell up to equilibration time. The glucose concentration progressively increased in the acceptor compartment, whereas the glucose concentration of the donor compartment decreased, as expected. The effective diffusion coefficient of glucose across the PCL/rGO membrane ( $D_{G,eff}$ ) was calculated as  $3.88 \times 10^{-10} \text{ m}^2 \cdot \text{s}^{-1}$ , in agreement with Suhaimi et al. [19]. They obtained an effective diffusivity of glucose of  $3.52 \times 10^{-10} \text{ m}^2 \cdot \text{s}^{-1}$  across a PCL scaffold with 80% porosity, using the diffusion cell technique.

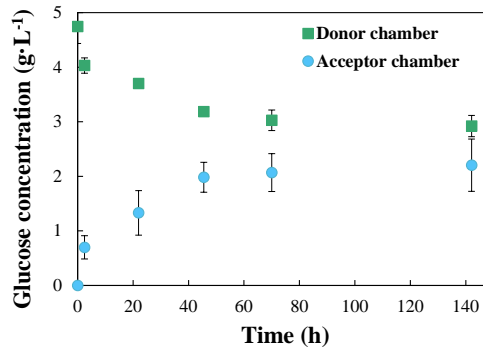


**Figure 2.15.** Evolution of glucose concentration in the donor and in the acceptor compartment during the glucose diffusion analysis across the PCL/rGO membrane.

Considering Equation 2.7 and the obtained values of  $D_{G,eff}$  and  $\varepsilon$ , the tortuosity was equal to 1.99. Furthermore, the tortuosity can be calculated through empirical equations, which provide the porosity-tortuosity relations for idealized porous materials [41]. For example, Alves et al. [42] employed the following empirical equation  $\tau = (2 - \varepsilon)^2 / \varepsilon$  to predict the tortuosity of porous membranes made by the phase separation method. For PCL/rGO membranes, the value of tortuosity calculated with this expression was 1.8, a value very similar to that estimated experimentally (Table 2.1). Nevertheless, the empirical equations were based on a specific idealized model of a porous medium and therefore, the estimated values were not comparable to our experimental results [19].

#### 2.3.4. Membrane flux properties

Figure 2.16 presents the permeate flux properties of the membranes, including a) the evolution of the dimensionless water fluxes until stabilization, b) the water fluxes ( $L \cdot m^{-2} \cdot h^{-1}$ ) at different transmembrane pressures and c) the hydraulic and total model BSA solution permeances ( $L \cdot m^{-2} \cdot h^{-1} \cdot bar^{-1}$ ) together with the values of BSA rejections.

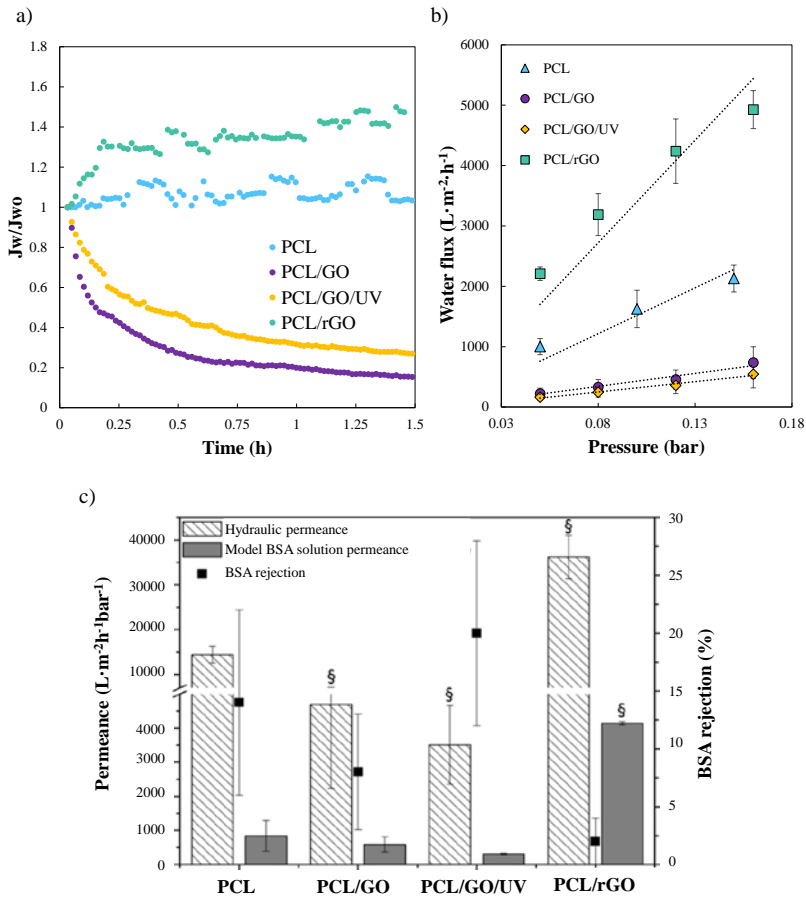


**Figure 2.16.** a) Evolution of the dimensionless water fluxes ( $J_w/J_{w0}$ ) of the membranes at 0.20 bar until stabilization (representative sample test). b) Hydraulic flux characterization vs. transmembrane pressure and c) the comparison between the hydraulic permeances and BSA solution permeances, and BSA rejections of the different membranes. §= $p < 0.05$  using one-way ANOVA, considering PCL as the reference.

The hydraulic properties of PCL/GO and PCL/GO/UV suffered a 75-85% flux decline during the filtration test until reaching the steady state with hydraulic permeances of  $4685 \pm 2447 L \cdot m^{-2} \cdot h^{-1} \cdot bar^{-1}$  and  $3507 \pm 1067 L \cdot m^{-2} \cdot h^{-1} \cdot bar^{-1}$  at steady state, respectively. Meanwhile, PCL and PCL/rGO presented stable water fluxes during the filtration test, in which

PCL/rGO (hydraulic permeance of  $36189 \pm 4789 \text{ L}\cdot\text{m}^{-2}\cdot\text{h}^{-1}\cdot\text{bar}^{-1}$  at steady state) offered significant improvements compared to PCL membranes (hydraulic permeance of  $14437 \pm 1860 \text{ L}\cdot\text{m}^{-2}\cdot\text{h}^{-1}\cdot\text{bar}^{-1}$  at steady state). These behaviors were associated to the different internal morphologies of the membranes (Figure 2.11). The reduction of the internal porosity observed in PCL/GO and PCL/GO/UV involved reduced hydraulic properties. On the contrary, the asymmetric porosity and the higher average pore diameter of PCL/rGO facilitated the water flux across the membrane more easily. Nevertheless, the hydraulic permeances of our PCL and PCL/GbN membranes were analogous or higher in comparison to other reported values in works that studied polymeric scaffolds for tissue engineering bioreactors (Table 2.4) [30,43–45].

**Table 2.4.** Hydraulic and culture/BSA filtration properties of different polymeric membranes at steady-state.

Membrane material	Hydraulic permeance ( $\text{L}\cdot\text{m}^{-2}\cdot\text{h}^{-1}\cdot\text{bar}^{-1}$ )	BSA/Culture m. permeance ( $\text{L}\cdot\text{m}^{-2}\cdot\text{h}^{-1}\cdot\text{bar}^{-1}$ )	Reference
PCL	$14437 \pm 1860$	$840 \pm 450$	Present work
PCL/GO	$4685 \pm 2447$	$591 \pm 219$	Present work
PCL/GO/UV	$3507 \pm 1067$	$310 \pm 23$	Present work
PCL/rGO	$36189 \pm 4789$	$4140 \pm 89$	Present work
PLGA-PVA	12000	-	[30]
PLLA	2094	-	[43]
	581	-	[46]
PES	5200	1040	[44]
PS	5200	660	[44]
PP	3010	300	[44]
PAN	146	-	[47]
PCL	200-800	-	[45]

For instance, commercial polyethersulfone (PES) and polysulfone (PS) hollow fiber membranes reached an average hydraulic permeance of  $5200 \text{ L}\cdot\text{m}^{-2}\cdot\text{h}^{-1}\cdot\text{bar}^{-1}$ , while the hydraulic permeance of a commercial polypropylene (PP) hollow fiber membrane was  $3010 \text{ L}\cdot\text{m}^{-2}\cdot\text{h}^{-1}\cdot\text{bar}^{-1}$  [44]. Polymeric hollow fiber membranes of PLLA exhibited hydraulic permeances of  $2094\text{-}581 \text{ L}\cdot\text{m}^{-2}\cdot\text{h}^{-1}\cdot\text{bar}^{-1}$  [43,46], whereas hollow fibers of PAN presented hydraulic permeances of  $146 \text{ L}\cdot\text{m}^{-2}\cdot\text{h}^{-1}\cdot\text{bar}^{-1}$  [47]. Moreover, flat membranes of PCL presented hydraulic permeances between  $200$  and  $800 \text{ L}\cdot\text{m}^{-2}\cdot\text{h}^{-1}\cdot\text{bar}^{-1}$ . In that study, the variation depended on the coagulation bath employed during the membrane fabrication by NIPS [45].

Figure 2.16c compares the hydraulic and total BSA model solution permeances of the different membranes. Overall, the nutrient permeance in all the membranes significantly diminished ( $\sim 95\%$ ) compared to the hydraulic permeance. However, the total BSA solution permeance of PCL/rGO membranes was still high ( $4140 \text{ L}\cdot\text{m}^{-2}\cdot\text{h}^{-1}\cdot\text{bar}^{-1}$ ). A similar trend applied to the results of Bettahali et al. [44]. They reported reductions of 80-90% of the total cell culture medium permeances with respect to the water permeances in the commercial microfiltration PES (from  $\sim 5400$  to  $1040 \text{ L}\cdot\text{m}^{-2}\cdot\text{h}^{-1}\cdot\text{bar}^{-1}$ ), PS (from  $\sim 5000$  to  $660 \text{ L}\cdot\text{m}^{-2}\cdot\text{h}^{-1}\cdot\text{bar}^{-1}$ ) and PP (from  $\sim 3000$  to  $300 \text{ L}\cdot\text{m}^{-2}\cdot\text{h}^{-1}\cdot\text{bar}^{-1}$ ) hollow fiber membranes.

Membrane fouling was considered to be the reason for the permeance reduction. Previous reports suggested three mechanisms for fouling in microfiltration membranes: i) internal fouling by pore narrowing, ii) pore blockage due to protein aggregates and iii) formation of a protein deposit on the membrane surface [30,48]. On account of the highly porous

structure of the membranes (Figure 2.11), internal fouling mechanism was selected as the most probable cause of the flux reduction [49]. Furthermore, the internal fouling phenomena could be attributed to internal protein adsorption on the microfiltration membranes [49]. This suggestion was in accordance with the high decrease in the total flux (approximately 82% in PCL membranes, 95% in PCL/GO and PCL/GO/UV membranes and 90% in PCL/rGO membranes) and with the low BSA rejections (between 2 and 20%) observed in the membranes during the filtration experiments (Figure 2.16c). Regardless the total BSA solution permeance reduction, all the membranes still displayed suitable permeances to be employed in a bioreactor, as reported Bettahalli et al. [44]. They found a theoretical culture medium permeance of  $250 \text{ L} \cdot \text{m}^{-2} \cdot \text{h}^{-1} \cdot \text{bar}^{-1}$  to be sufficient to supply glucose to enable 3-layer cell survival in a bioreactor.

### 2.3.5. Membrane biocompatibility

Figure 2.17 shows confocal images of U87 glioblastoma cells cultured on the surface of PCL and PCL/GbN membranes at day 1, 6, 14 and 21. Overall, membranes with GbN enhanced the cell proliferation during the experiment. At day 1, similar cell attachment was observed. While cells on PCL membranes seemed to form clusters and were not homogeneously distributed on the surface, membranes with GbN favored cells' uniform distribution along the surface of the membranes. At day 6 and day 14, the presence of GbN resulted in an increased cell density with suitable neural cell morphology in comparison to the plain PCL. After 21 days, PCL/GbN samples showed similar cell confluence and slightly higher than that of PCL membranes. Therefore, these preliminary biocompatible tests demonstrated that PCL/GbN membranes are

promising scaffolds that support neural cell cultures in neural tissue engineering applications. These results showed similarities to previous works, in which polymeric scaffolds containing rGO or GO nanoplatelets [9,12] as well as scaffolds of graphene [50] or GO [51] exhibited biocompatibility.

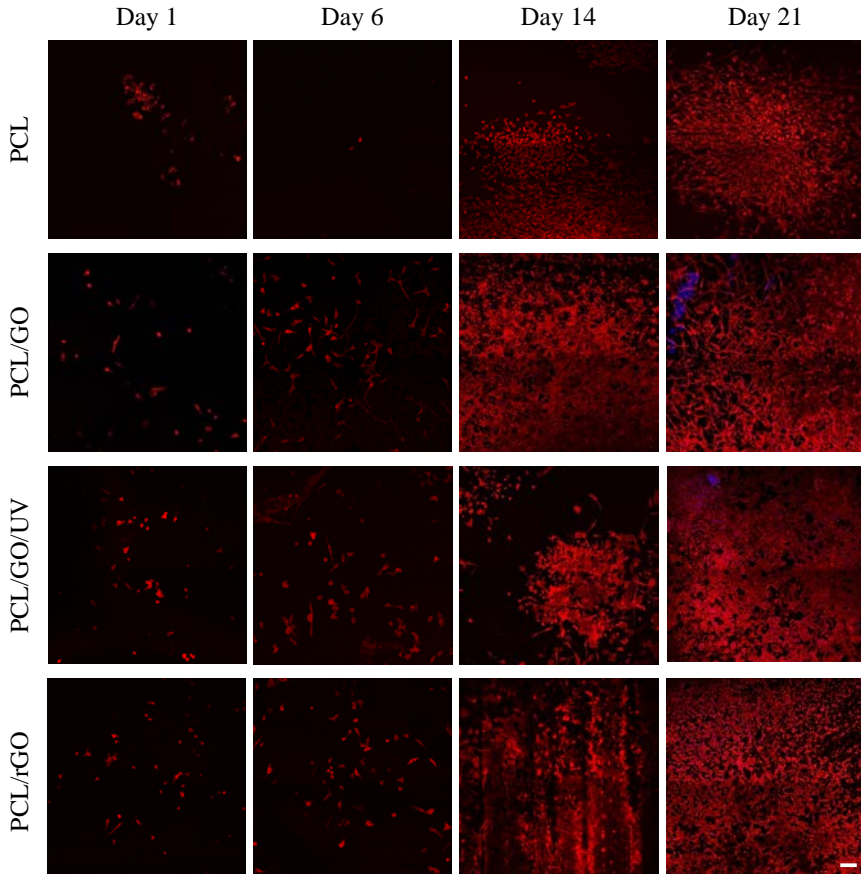


**Figure 2.17.** Confocal microscopy images of U87 glioblastoma cells cultured on PCL and PCL/GbN membranes after 1, 6, 14 and 21 days. Cytoplasmic membrane of cells was stained by fluorescent-labelled phalloidin (red). Scale bar represents 100  $\mu\text{m}$ .

## 2.4. Final remarks

In this study, PCL/GbN membranes were developed with the purpose of being used in neural cell culture applications. In contrast to previous reported works, our PCL/GbN were fabricated by the NIPS technique, using mild temperature conditions and nontoxic reductive reagents.

According to spectroscopic analyses, thermal analyses and mechanical characterization, the formation of covalent bonds between PCL and GO was not conclusive, considering the low GO concentration used in the membranes (0.1 w/w%). Therefore, membranes were considered to be mixed-matrix membranes, without nanocomposite formation. But despite that, PCL/GO/UV membranes reflected a possible covalent bond between PCL and reduced GO particles that was observed in spectroscopy and mechanical results. However, the DSC thermograms pointed out that the presence of interactions between PCL and the GO nanomaterials could be related to van der Waals forces.

The presence of GbN in the membranes did not influence in the electrical properties, which was attributed to the low nanomaterial loads used (0.1 w/w%). Furthermore, the mechanical properties of the membranes did not improve when GbN was added in the membranes. On the contrary, GbN limited the polymer chain mobility, being the mechanical properties of PCL/GbN reduced at rupture. Nevertheless, the membranes of PCL/GbN at 0.1 w/w% were expected to be suitable to maintain cell cultures in perfusion bioreactors. All membranes presented high water and nutrient transport properties for cell culture bioreactors, attributed to the interconnected porous structure of the membranes. In particular, PCL/rGO membranes exhibited higher porosity with

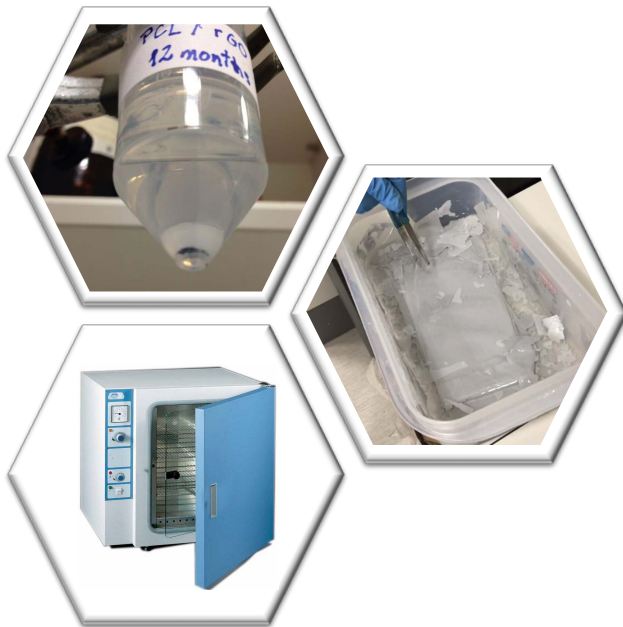
asymmetric pore distribution, leading to outstanding mass transport properties with low BSA rejection rates and high glucose diffusion. According to biocompatible tests, the membranes with GbN promoted a homogeneous distribution of cells along the surface of the membranes and suitable cell morphologies. In conclusion, PCL/GbN membranes showed suitable properties to act as scaffolds in neural tissue applications, mainly PCL/rGO membranes, which possessed outstanding flux properties.

## 2.5. References

- [1] N. Diban, S. Sánchez-González, M. Lázaro-Díez, J. Ramos-Vivas, A. Urriaga, *J. Memb. Sci.* **2017**, *540*, 219.
- [2] N. Diban, J. Ramos-Vivas, S. Remuzgo-Martinez, I. Ortiz, A. Urriaga, *Curr. Top. Med. Chem.* **2014**, *14*, 2743.
- [3] Y. C. Shin, J. H. Lee, L. Jin, M. J. Kim, Y. J. Kim, J. K. Hyun, T. G. Jung, S. W. Hong, D. W. Han, *J. Nanobiotechnology* **2015**, *13*, 1.
- [4] O. J. Yoon, C. Y. Jung, I. Y. Sohn, H. J. Kim, B. Hong, M. S. Jhon, N. E. Lee, *Compos. Part A Appl. Sci. Manuf.* **2011**, *42*, 1978.
- [5] O. N. Ruiz, K. A. S. Fernando, B. Wang, N. A. Brown, P. G. Luo, N. D. McNamara, M. Vangsness, Y. P. Sun, C. E. Bunker, *ACS Nano* **2011**, *5*, 8100.
- [6] S. G. Rotman, Z. Guo, D. W. Grijpma, A. A. Poot, *Polym. Adv. Technol.* **2017**, *28*, 1233.
- [7] B. Chaudhuri, D. Bhadra, L. Moroni, K. Pramanik, *Biofabrication* **2015**, *7*, 015009.
- [8] J. Song, H. Gao, G. Zhu, X. Cao, X. Shi, Y. Wang, *Carbon N. Y.* **2015**, *95*, 1039.
- [9] C. Wan, B. Chen, *Biomed. Mater.* **2011**, *6*, 055010.
- [10] B. Holmes, X. Fang, A. Zarate, M. Keidar, L. G. Zhang, *Carbon N. Y.* **2016**, *97*, 1.
- [11] S. Ramazani, M. Karimi, *Mater. Sci. Eng. C* **2015**, *56*, 325.
- [12] S. Sayyar, E. Murray, B. C. Thompson, S. Gambhir, D. L. Officer, G. G. Wallace, *Carbon N. Y.* **2013**, *52*, 296.
- [13] G. S. Wang, Z. Y. Wei, L. Sang, G. Y. Chen, W. X. Zhang, X. F. Dong, M. Qi, *Chinese J. Polym. Sci.* **2013**, *31*, 1148.

- [14] S. R. A. Llaguno, L. F. Parada, *Br. J. Cancer* **2016**, *115*, 1445.
- [15] S. Jäkel, L. Dimou, *Front. Cell. Neurosci.* **2017**, *11*, 1.
- [16] W. S. Hummers, R. E. Offeman, *J. Am. Chem. Soc.* **1958**, *80*, 1339.
- [17] P. Ribao, M. J. Rivero, I. Ortiz, *Environ. Sci. Pollut. Res.* **2017**, *24*, 12628.
- [18] Y. H. Ding, P. Zhang, Q. Zhuo, H. M. Ren, Z. M. Yang, Y. Jiang, *Nanotechnology* **2011**, *22*, 0.
- [19] H. Suhaimi, S. Wang, T. Thornton, D. B. Das, *Chem. Eng. Sci.* **2015**, *126*, 244.
- [20] B. J. Papenburg, L. Vogelaar, L. A. M. Bolhuis-Versteeg, R. G. H. Lammertink, D. Stamatialis, M. Wessling, *Biomaterials* **2007**, *28*, 1998.
- [21] B. E. Poling, G. H. Thomson, D. G. Friend, R. L. Rowley, W. V. Wilding, in *Perry's Chem. Eng. Handb.*, **2008**, pp. 2–1, 2–517.
- [22] R. Dominguez, K. C. Holmes, *Annu. Rev. Biophys.* **2011**, *40*, 169.
- [23] D. Liang, C. Cui, H. Hub, Y. Wang, S. Xu, B. Ying, P. Li, B. Lu, H. Shen, *J. Alloys Compd.* **2014**, *582*, 236.
- [24] B. . Mistry, *A Handbook of Spectroscopic Data Chemistry (UV, IR, PMR, 13CNMR and Mass Spectroscopy)*, **2009**.
- [25] O. Akhavan, *Carbon N. Y.* **2015**, *81*, 158.
- [26] N. Golafshan, M. Kharaziha, M. Fathi, *Carbon N. Y.* **2017**, *111*, 752.
- [27] T. Kuilla, S. Bhadra, D. Yao, N. H. Kim, S. Bose, J. H. Lee, *Prog. Polym. Sci. Vol.* **2010**, *35*, 1350.
- [28] F. Gattazzo, C. De Maria, Y. Whulanza, G. Taverni, A. Ahluwalia, G. Vozzi, *J. Biomed. Mater. Res. - Part B Appl. Biomater.* **2015**, *103B*, 1107.
- [29] N. Diban, D. F. Stamatialis, *Macromol. Symp.* **2011**, *309–310*, 93.
- [30] G. Meneghello, D. J. Parker, B. J. Ainsworth, S. P. Perera, J. B. Chaudhuri, M. J. Ellis, P. A. De Bank, *J. Memb. Sci.* **2009**, *344*, 55.
- [31] W. R. Bowen, N. J. Hall, *Biotechnol. Bioeng.* **1995**, *46*, 28.
- [32] G. R. Guillen, Y. Pan, M. Li, E. M. V. Hoek, *Ind. Eng. Chem. Res.* **2011**, *50*, 3798.
- [33] J. Yin, B. Deng, *J. Memb. Sci.* **2015**, *479*, 256.
- [34] M. Mulder, in *Basic Princ. Membr. Technol.*, Kluwer, Dordrecht, **1996**, pp. 54–109.
- [35] T. Elzein, M. Nasser-Eddine, C. Delaite, S. Bistac, P. Dumas, *J. Colloid Interface Sci.* **2004**, *273*, 381.
- [36] A. Campos, J. M. Marconcini, S. M. Martins-Franchetti, L. H. C. Mattoso, *Polym. Degrad. Stab.* **2012**, *97*, 1948.

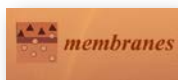
- [37] C.-C. Yeh, C.-N. Chen, Y.-T. Li, C.-W. Chang, M.-Y. Cheng, H.-I. Chang, *Cell. Polym.* **2011**, *30*, 261.
- [38] X. Luo, *Effects of SureFlo® on the Thermo-Oxidative Stability of Polyethylene (PE), Polypropylene (PP) and Polystyrene (PS) Systems*, **2011**.
- [39] P. X. Thinh, C. Basavajara, J. K. Kim, D. S. Huh, *Polym. Compos.* **2012**, *33*, 2159.
- [40] M. E. Uddin, R. K. Layek, N. H. Kim, D. Hui, J. H. Lee, *Compos. Part B Eng.* **2015**, *80*, 238.
- [41] H. Suhaimi, D. Bhusan Das, *Rev. Chem. Eng.* **2016**, *32*, 629.
- [42] V. D. Alves, I. M. Coelho, *J. Memb. Sci.* **2004**, *228*, 159.
- [43] N. M. S. Bettahalli, H. Steg, M. Wessling, D. Stamatialis, *J. Memb. Sci.* **2011**, *371*, 117.
- [44] N. M. S. Bettahalli, J. Vicente, L. Moroni, G. A. Higuera, C. A. Van Blitterswijk, M. Wessling, D. F. Stamatialis, *Acta Biomater.* **2011**, *7*, 3312.
- [45] N. Diban, S. Haimi, L. Bolhuis-Versteeg, S. Teixeira, S. Miettinen, A. Poot, D. Grijpma, D. Stamatialis, *J. Memb. Sci.* **2013**, *438*, 29.
- [46] S. Morelli, A. Piscioneri, S. Salerno, C. C. Chen, C. H. Chew, L. Giorno, E. Drioli, L. De Bartolo, *Biofabrication* **2017**, *9*, 025018.
- [47] S. Morelli, S. Salerno, A. Piscioneri, F. Tasselli, E. Drioli, L. De Bartolo, *Chem. Eng. J.* **2016**, *305*, 69.
- [48] A. Persson, A. S. Jönsson, G. Zacchi, *J. Memb. Sci.* **2003**, *223*, 11.
- [49] W. R. Bowen, Q. Gan, *Biotechnol. Bioeng.* **1991**, *38*, 688.
- [50] N. Li, Q. Zhang, S. Gao, Q. Song, R. Huang, L. Wang, L. Liu, J. Dai, M. Tang, G. Cheng, *Sci. Rep.* **2013**, *3*, 1604.
- [51] M. C. Serrano, J. Patiño, C. García-Rama, M. L. Ferrer, J. L. G. Fierro, A. Tamayo, J. E. Collazos-Castro, F. del Monte, M. C. Gutiérrez, *J. Mater. Chem. B* **2014**, *2*, 5698.



## Chapter 3

### Study of the hydrolytic degradation and stability behavior of poly( $\epsilon$ -caprolactone)/reduced graphene oxide membranes for *in vitro* models

This chapter was adapted from the manuscript published in “Membranes”:



**S. Sánchez-González**, N. Diban, A. Urriaga, Hydrolytic degradation and mechanical stability of poly( $\epsilon$ -caprolactone)/reduced graphene oxide membranes as scaffolds for *in vitro* neural tissue regeneration, *Membranes*. 8 (2018) 1–14 [1].



### 3.1. Introduction

The promising properties exhibited by the poly( $\epsilon$ -caprolactone)/reduced graphene oxide (PCL/rGO) membranes in *in vitro* neural models (*Chapter 2*), generated further interest in studying the long term properties of these membranes. Biodegradable scaffolds should maintain their properties with the necessary time to complete their function [2]. Therefore, the study of the *in vitro* hydrolytic degradation route and stability behavior of these innovative membranes was crucial, as PCL is a non-permanent scaffolding material.

PCL is a biodegradable long-term stable polymer subjected to degradation conditions (up to 2–4 years), which depends on the starting molecular weight of the PCL [3]. This polymer is also identified as bioresorbable because its chain breakdown pathway forms degradation products, which can be rapidly removed from the body without cytotoxic effects [4].

Figure 3.1 describes the degradation mechanisms of polymers that are classified into bulk and surface erosion. Bulk degradation happens when the medium penetrates inside the polymer matrix causing uniform hydrolytic chain scissions. The size and the shape of the material are maintained and the molecular weight of the polymer is reduced. In contrast, the surface degradation arises when water cannot penetrate inside the polymer matrix. In consequence, the polymer sample loses material exclusively on the surface, while its molecular weight does not suffer a significant change [4,5].

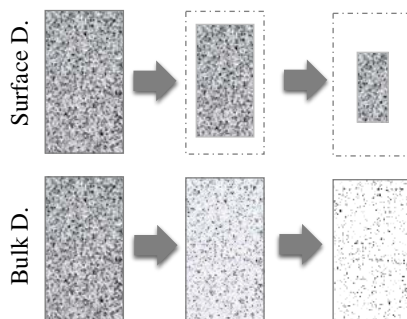


**Figure 3.1.** Scheme description of the surface and bulk erosion.

Different studies have successfully documented the degradation behavior of PCL-based scaffolds [4,6–9]. For example, Castilla-Cortázar et al. [6] investigated the PCL degradation process under hydrolytic and enzymatic conditions. The surface erosion degradation rate was found to be faster in the presence of enzymes, while the hydrolytic degradation resulted in a bulk degradation mechanism. However, it has also been observed that the stability behavior under hydrolytic degradation conditions can change by the introduction of graphene based nanomaterials (GbNs) in polymer matrices [10–12].

Table 3.1 summarizes previous works that studied the degradation behavior of PCL/GbN. For instance, Meng et al. [10] evaluated the hydrolytic degradation of electrospun PCL nanofiber membranes with different contents of multiwalled nanotubes (MWCNTs) in phosphate buffer solution (PBS, pH 7.4, 37°C) for up to 8 weeks. The PCL/MWCNTs membranes showed faster weight loss and morphology decomposition than the plain PCL membranes. The hydrolyzed polymers diffused from the fibers and made water molecules diffuse inside the fibers more easily. Furthermore, Mohammadi et al. [11] studied nanofibers composed of PCL and GO that were subjected to accelerated hydrolytic degradation using an alkaline medium during 3 days. The degradation rate of the PCL scaffolds

also increased due to the addition of GbNs. In that example, the hydrophilicity of the scaffold increased due to the polar oxygenated groups of the GO nanomaterials, and consequently the water adsorption and hydration of PCL chains also enhanced, leading to faster degradation rates. However, the integrity of PCL/GO fibers was preserved, and fewer fiber breakages occurred in comparison to the PCL plain scaffold.

**Table 3.1.** Degradation studies of PCL/GbN membranes reported in the literature.

Ref	Structure	Type of degradation	Conditions	Prop. studied	GbN influence
PCL/MWCNTs [10]	Porous nanofiber	Bulk-Hydrolytic	37°C PBS pH 7.4 8 weeks	Weight loss Morphology	Accelerating effect
PCL/GO [11]	Porous nanofiber	Surface-Hydrolytic	37°C NaOH pH alkaline 3 days	Weight loss Morphology	Accelerating effect
PCL/rGO [12]	Dense flat membrane	Surface-Enzymatic	37°C Lipase+PBS pH 7.4 96 h	Weight loss Morphology Wettability Resistivity Crystallinity Toxicity Thermal analysis	Decelerating effect

Moreover, Murray et al. [12] studied the enzymatic degradation of PCL/rGO scaffolds. The enzymatic degradation kinetics was not significantly influenced by rGO loadings below 5 w/w%. However, loadings of rGO above 5 w/w% caused the decrease of the enzymatic degradation rate, attributed to the higher hydrophobicity of the composite PCL/rGO materials. Enzymatic or accelerated degradation makes easier

the study of biodegradable polymers fate. Nevertheless, the hydrolytic degradation over long periods mimics more adequately the *in vitro* conditions [6]. In addition, the enzymatic/accelerated and long-term degradation are defined by different degradation mechanisms, leading to different functional properties.

As the long-term hydrolytic degradation of PCL/rGO membranes has not been reported so far (see Table 3.1), in this chapter, PCL/rGO membranes were evaluated under hydrolytic degradation conditions for 12 months. The hydrolytic degradation of the membranes was evaluated through functional, mechanical, morphological, chemical and thermal analysis. Also, the potential effect on cell cytotoxicity was characterized by monitoring the degradation by-products. The hydrolytic degradation pathway was hypothesized and ascertained by the kinetic results. Additionally, plain PCL membranes were evaluated and compared.

## **3.2. Materials and methods**

### **3.2.1. Hydrolytic degradation assay**

PCL and PCL/rGO membranes were exposed to hydrolytic degradation under simulated *in vitro* bioreactor conditions. A sufficient number of membranes were submerged in PBS (pH 7.4) and placed in an incubator at 37 °C. PCL and PCL/rGO membranes were kept separately in different vessels. For sterilization, PBS was autoclaved and membranes were submerged in a solution of ethanol 70% and exposed to a UV light for 20 min in a laminar cabinet. Samples were taken out of the solution for characterization at predetermined degradation time intervals: 0, 2, 4, 6, 9, and 12 months. Before testing took place, membrane samples were submerged in ultrapure water to remove any possible salt deposit.

### 3.2.2. Physical–Chemical characterization

The physical-chemical properties were useful to define the causes of the degradation and their effects on the functional behavior. Physical-chemical characterization included the study of changes on morphology, pH, molecular weight, formation of degradation products and thermal properties.

Figure 3.2 shows the gel permeation chromatograph (GPC model 510, Waters) used to determine the average molecular weight of the polymer in the membranes. GPC consisted of three size exclusion chromatographic columns (model Styragel HR 5E, Waters) and a refractometer (model 410, Waters) that was used for detection. The columns, composed of styrene divinyl benzene copolymer, were placed in series and thermostated at 40 °C. The GPC was connected to the computer to provide the average molecular weight values using the Empower 2 software (Waters).



**Figure 3.2.** Gel permeation chromatography (GPC) system.

Measurements were taken using tetrahydrofuran (THF 99.9%, Panreac) as carrier at  $1 \text{ mL} \cdot \text{min}^{-1}$ . Results were obtained from a universal calibration curve related to polystyrene standards (Shodex, Waters), corrected by the Mark–Houwink–Sakura equation and the corresponding PCL coefficients.

The sample preparation consisted in solubilizing the membrane sample in THF at a concentration of  $0.5 \text{ mg}\cdot\text{mL}^{-1}$ . Before GPC injection, the solubilized sample of PCL/rGO was centrifuged for 1 hour and filtered through a  $0.45 \text{ }\mu\text{m}$  filter to avoid rGO contamination in the columns of GPC. Measurements were done in duplicate.

Differential scanning calorimetry (DSC, DSC-131, SETARAM Instrumentation) was used to analyze the thermal properties of the membranes at 0 and 12 months of hydrolytic degradation. Samples were analyzed as explained in *Chapter 2*.

The generation of hydrolysis degradation by-products was characterized. 6-hydroxycaproic acid (6-HCA) is a monomer typically found in PCL degradation studies. Samples of the PBS medium, which was used to submerge the membranes, were analyzed using UV-vis spectrophotometer (UV-1800 model, Shimadzu) at a wavelength of 210 nm [13]. The concentration of 6-HCA was evaluated at 6 and 12 months of degradation time. Moreover, the pH change of the PBS solution was also measured.

The rGO content of the membrane matrix was analyzed, so that the fate of rGO nanomaterials during the hydrolytic degradation could be determined. 5 mg samples of PCL/rGO membranes (at 0 and 12 months of degradation) were dissolved in 10 mL of THF. Then, the solution was centrifuged to precipitate the rGO for qualitative analysis.

The visual aspect of the membrane samples was evaluated periodically through photographs of the same membrane specimen. In addition, the microscopic morphology of the membranes was evaluated by scanning electron microscopy (SEM) images. Images were obtained at a voltage of

20 kV. Samples were prepared using the same procedure as described in *Chapter 2*.

### 3.2.3. Functional characterization

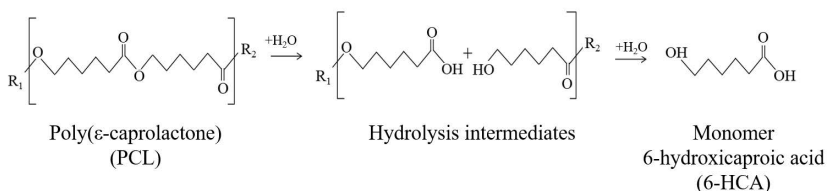
The study of the functional properties, including mechanical and nutrient flux characterization, were aimed at evaluating the ability of the herein prepared membranes for applications in bioreactors during long term degradation.

Axial tensile tests and bovine albumin serum (BSA) model flux analyses were conducted as explained in *Chapter 2*. Results were expressed as average  $\pm$  standard deviation.

## 3.3. Results and discussion

### 3.3.1. Physical-chemical properties characterization

The hydrolysis degradation pathway of the PCL polymer is defined in Figure 3.3. In the reaction between PCL and water, the scission of the ester bond of PCL was produced. In consequence, carboxyl end groups were formed as well as the PCL average molecular size was progressively reduced. As a result, water soluble degradation products arose, such as oligomers and the 6-HCA monomer. These by-products diffused out of the membrane matrix and solubilized in the PBS medium [15].



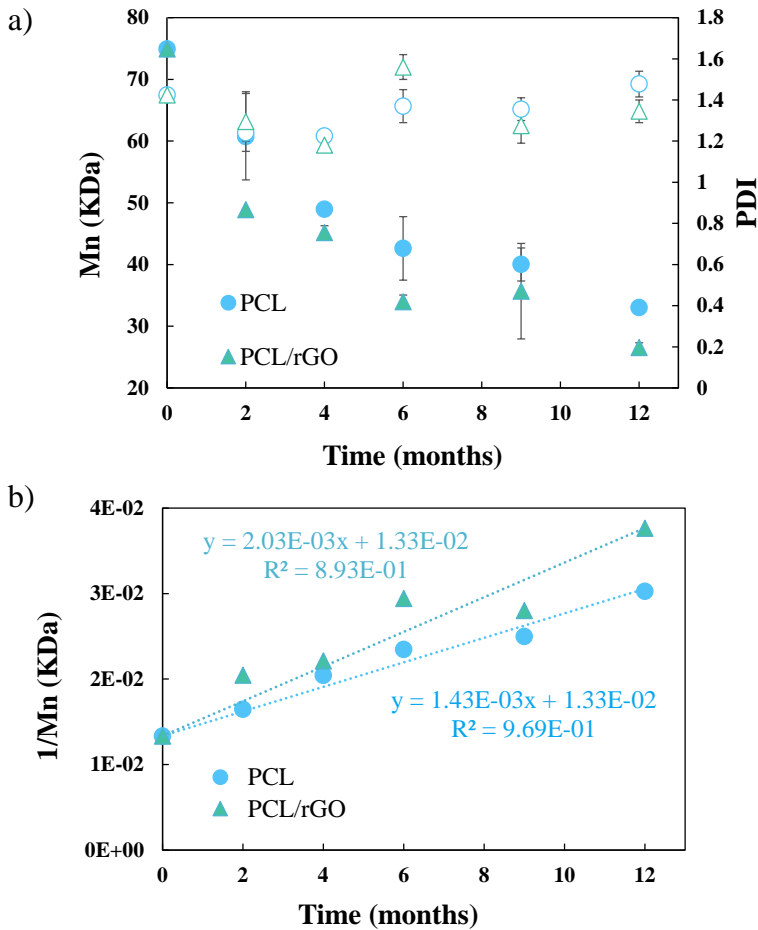
**Figure 3.3.** PCL hydrolytic degradation process, adapted from Woodruff et al. [3].

Figure 3.4a shows the average molecular weight ( $M_n$ ) and the polydispersity index (PDI) of the molecular weight distribution during the hydrolytic degradation. Overall, the  $M_n$  of the membranes showed a gradual decrease. Initially, the  $M_n$  reduced significantly in the first two months, from  $75 \pm 6$  kDa to  $61 \pm 7$  kDa (drop of 19%) in PCL and to 49 kDa (drop of 35%) in PCL/rGO membranes. After, the  $M_n$  decreased more slowly, but at similar rates in both cases. After 12 months, PCL membranes presented a  $M_n$  of  $33 \pm 0.04$  kDa with an overall reduction of 56% in the molecular weight, while the  $M_n$  of PCL/rGO was  $27 \pm 0.75$  kDa that accounts for a reduction of 65%. On the contrary, the PDI was maintained during the hydrolytic degradation, with PDI values between 1.47-1.23 in PCL membranes and 1.56-1.18 in PCL/rGO membranes.

Figure 3.4b represents the kinetics of the hydrolysis of PCL and PCL/rGO membranes, which were obtained from  $M_n$  kinetic data. Results determined that the hydrolysis of our membranes followed second order kinetics, defined in Equation 3.1 as [16]:

$$\frac{dE}{dt} = k \cdot C_B \cdot C_w \cdot t \quad (3.1)$$

where  $E = \frac{\rho}{(N \cdot M_0)}$  is the chain end concentration,  $C_B = \frac{\rho}{M_0} \cdot \left(1 - \frac{1}{N}\right)$  is the total bond concentration,  $C_w$  is the water concentration and  $k$  is the kinetic constant of the PCL polymer hydrolysis. The initial monomer molecular weight ( $M_0$ ) and  $C_w$  are constants with the same values in PCL and PCL/rGO membranes. Moreover,  $\rho$  is the density of the polymer samples and  $N$  is the degree of polymerization.



**Figure 3.4.** a) Average molecular weight during the hydrolytic degradation ( $M_n$ , filled symbols) and polydispersity index (PDI, empty symbols). b) Kinetics of the hydrolysis of PCL and PCL/rGO membranes. Dotted lines represented the 2<sup>nd</sup> order hydrolysis kinetic adjustment of the molecular weight.

Considering that the carboxylic/ester polymer groups present similar probability of hydrolytic attack, the hydrolysis kinetics can be simplified on polyesters with large molecular weight ( $N \gg 1$ ) as (Equation 3.2) [16]:

$$\frac{1}{M_n} = \frac{1}{M_{n_0}} + \frac{1}{M_0} k \cdot C_w \cdot t \quad (3.2)$$

In this study, all the carboxylic bonds of the polymer chain demonstrated equal reactivity as the PDI values were constant during the hydrolytic degradation.

The second order kinetics seen in our membranes were in line with typical hydrolysis of large molecular weight polyesters [16]. Comparing the hydrolysis kinetics of PCL and PCL/rGO membranes, they were not significantly different. Despite the hydrophobic character of the rGO nanomaterials [17], the kinetic of PCL/rGO membranes was hardly faster than the PCL membranes ( $\frac{k_{PCL/rGO}}{k_{PCL}} = \frac{2.03 \times 10^{-3}}{1.43 \times 10^{-3}} \approx 1.4$ ).

Figure 3.5 shows the concentration of 6-HCA per unit mass released to the PBS medium first, after 6 and 12 months of degradation. The pH change of the PBS medium is also presented. A significant increase of the concentration of 6-HCA with the degradation time was found, being higher in the PCL/rGO than in PCL membranes. This behavior was affected in accordance with the fast reduction in molecular size observed in the PCL/rGO membranes (Figure 3.4). As it was expected, the water penetration produced scission of the ester bonds and therefore the 6-HCA monomer was released and diffused in the buffer media. In consequence, the concentration of 6-HCA increased with time. In contrast, due to the buffer media, the overall pH of the PBS solution was only slightly reduced during the hydrolytic degradation. It changed from 7.4 to 7.1 for PCL membranes and for 6.9 in PCL/rGO membranes, after 12 months of degradation.

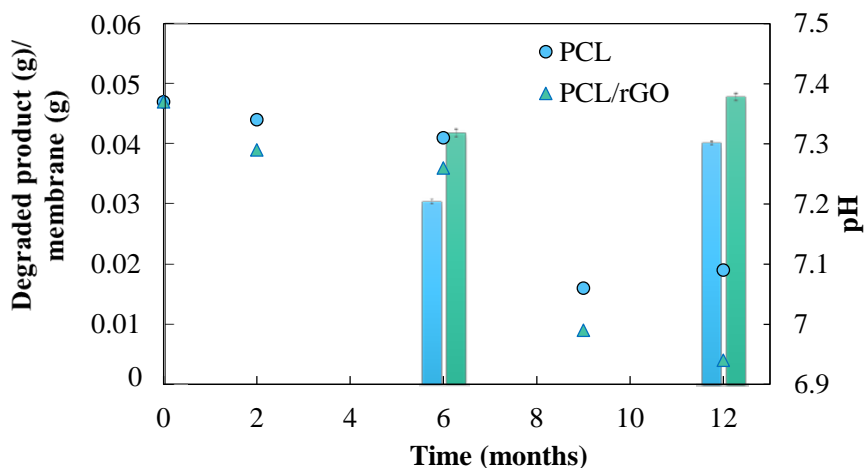


**Figure 3.5.** Mass of 6-HCA in the PBS medium formed during the hydrolytic degradation of PCL and PCL/rGO membranes (bars), and the pH change of the PBS solution (dots).

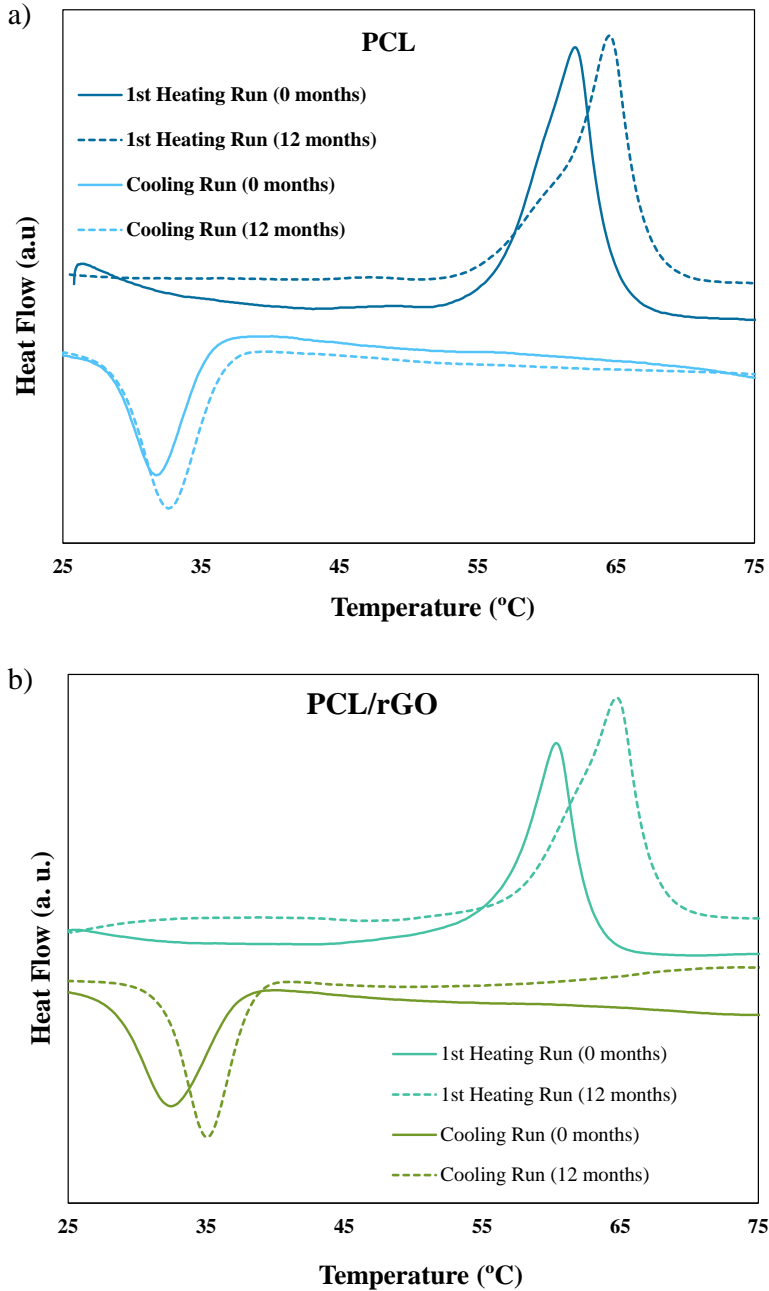
Figure 3.6 presents the rGO content that precipitated after centrifugation of 5 mg of re-dissolved PCL/rGO membrane samples at 0 and 12 months. Images show that the amount of rGO was qualitatively higher in the solution of PCL/rGO membranes at 12 months than at time 0. Therefore, results suggested that the rGO particles mostly remained in the polymer matrix along the long term hydrolytic experiment.



**Figure 3.6.** rGO content of the PCL/rGO membranes at 0 and 12 months of degradation.

In view of the acidic degradation products, the mid- and end-point degradation products should be carefully investigated as alterations in the pH can lead to negative effects in the cell behavior [5]. Also, the rGO nanomaterial content should be monitored for possible immunogenic reactions [18]. The pH barely changed while the rGO nanomaterials remained mainly in the membrane during the hydrolytic degradation. The results obtained determined that our membranes would not negatively affect the cell behavior. This was supported by the reliable preliminary results observed in cell cultures (*Chapter 2*). A suitable biocompatibility of the membranes with glioblastoma cells was found after 21 days of culture. The toxicity of the GbN is associated with its difficult degradation, being possible through enzymes or microbes [19]. However, our membranes did not provide negative effects on the cells probably because of the small concentration of nanomaterials employed in the biocompatible polymer matrix [19,20]. When comparing the results with other studies, Murray et al. [12] also showed that loadings up to 5 w/w % of rGO in PCL matrices did not negatively affected L-929 fibroblast cells growing for short periods under enzymatic degradation conditions.

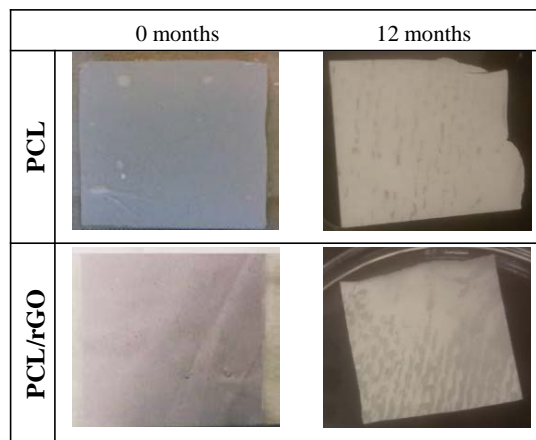
Figure 3.7 presents the DSC thermograms of the a) PCL and b) PCL/rGO membranes at 0 and after 12 months of hydrolytic degradation. Overall, the thermal properties experienced an increase during the degradation time in both types of membranes. The melting temperature ( $T_m$ ) increased during the hydrolytic degradation from 62.10 °C to 64.54 °C in PCL and from 60.36 °C to 64.72 °C in PCL/rGO after 12 months. Moreover, the crystallization temperature ( $T_c$ ) increased in both membranes. The initial  $T_c$  in PCL membranes was 31.75 °C and increased 0.88 °C after 12 months. Meanwhile, the  $T_c$  in PCL/rGO was 35.00 °C after 12 months with an initial  $T_c$  equal to 32.45 °C.



**Figure 3.7.** DSC thermograms of PCL (a) and PCL/rGO (b) membranes at 0 and 12 months of degradation.

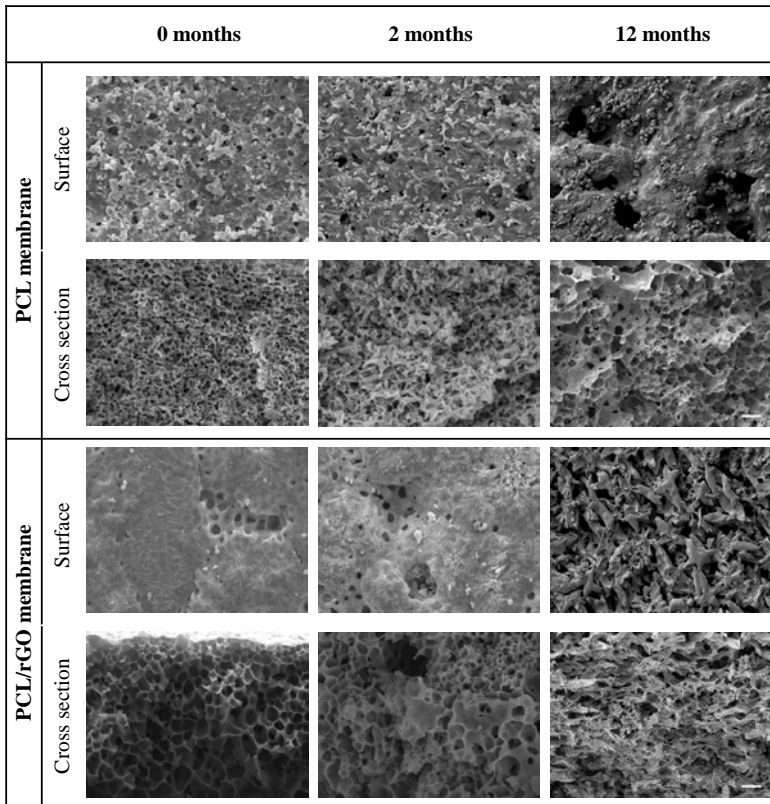
The moderate increase observed in the thermal properties during the hydrolytic degradation was attributed to the preferential hydrolytic attack of the amorphous polymer phase [2], which was confirmed by the increase of the degree of crystallinity ( $\chi_c$ ) in PCL and PCL/rGO membranes from 35% to 44% and from 41% to 46%, respectively.

Figure 3.8 presents the wet membranes both at 0 and after 12 months of degradation. The visual aspect of the membranes did not show a significant change during the hydrolytic degradation, including features as width, length, and thickness. However, a visible high wet internal porosity was observed in the specimens after 12 months, being more notable in PCL/rGO membranes.



**Figure 3.8.** Wet PCL and PCL/rGO membranes at 0 and 12 months of degradation (size of the membrane pieces = 4x4 cm<sup>2</sup>).

Figure 3.9 shows the microscopic morphology of the membranes. Membranes presented a noticeable change on the surface as well as in the cross section during the hydrolytic degradation. After 2 months, membranes eroded slightly. Then, the morphology of the membranes was clearly degraded after 12 months of degradation.



**Figure 3.9.** SEM images of PCL and PCL/rGO membranes at 0, 2 and 12 months during hydrolytic degradation. Scale bars = 10  $\mu\text{m}$ .

During the degradation process, the morphology of the membranes suffered a clear change; meanwhile the dimensions of the membranes remained constant. After considering the results achieved (Figure 3.4 and 3.9), the degradation mechanism was defined as bulk degradation [21]. The main cause of the bulk hydrolysis mechanism was referred to a highly porous structure of the membranes [22]. The high internal porosity of the membranes enhanced the water penetration and outward diffusion of the degradation products. Consequently, the evaluated membranes presented a faster degradation rate than in the PCL polymer (2-4 years) [3]. Comparing our analysis to other works, Castilla-Cortázar et al. [6] also determined a

bulk degradation behavior of PCL networks under similar hydrolytic degradation conditions. Overall, PCL membranes reported in the literature [8,9] with similar molecular weight (PCL 80 kDa) demonstrated very low rates of degradation in comparison with the membranes that were developed by us, being attributed to the different porous structures of the materials.

### **3.3.2. Functional characterization**

Figure 3.10 presents the mechanical properties of PCL and PCL/rGO membranes under hydrolytic degradation. The analysis of the mechanical properties included the evolution of the Young modulus (Figure 3.10a), ultimate strain (Figure 3.10b), ultimate tensile strength (Figure 3.10c) and yield point (Figure 3.10d). It should be pointed out that the mechanical properties were analyzed only during 4 months, due to the loss of mechanical stability at longer periods. Specifically, the stability of PCL and PCL/rGO membranes was lost after 6 and 4 months, respectively.

Figure 3.10 showed a progressive reduction of the mechanical properties of the membranes during the hydrolytic degradation. At time 0, the mechanical properties of PCL/rGO membranes underwent a significant reduction in comparison with the plain PCL membranes. Then, PCL and PCL/rGO membranes suffered similar reduction rates in the mechanical properties, which varied from 41 to 68% depending on the studied parameter. After 4 months, the reduction of the mechanical properties was maintained at almost the same level in PCL/rGO. However, PCL membranes presented different reduction rates, depending on the analyzed parameter.

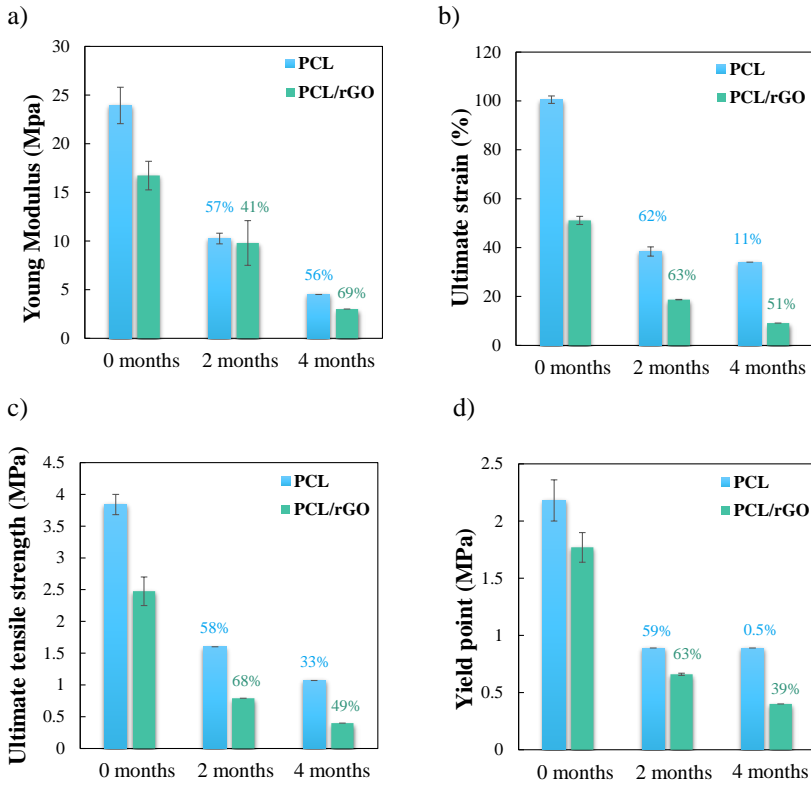


**Figure 3.10.** Mechanical properties of the membranes at 0, 2 and 4 months of degradation, in terms of a) Young modulus, b) ultimate strain, c) ultimate tensile strength and d) yield point (% values represented the reduction of the mechanical parameters between degradation times).

Overall, the PCL/rGO membranes showed a significant decrease in the mechanical properties at any degradation time with respect to plain PCL membranes. Moreover, PCL/rGO membranes presented a faster and more intense loss of structural stability. This behavior was attributed to the presence of GbNs, as rGO formed restrictions in the mobility of the polymer chains [23] and generated defects and gaps in the polymer matrix [24].

Despite the fast decrease of the mechanical properties of our fabricated membranes, they were considered able to act as scaffolds in neural regeneration. Indeed, hydrogels typically employed as scaffolds materials for neural tissue regeneration (Matrigel [25], modified gelatin [26], polyethylene glycol, or alginate hydrogels [27,28]) presented values of mechanical stiffness close to those of our 4-month degraded membranes. By comparing other materials employed in neural cell cultures, the Young modulus value was established in the order of 0.2–20 kPa in alginate hydrogel [27] and 0.1–1.2 MPa in modified gelatin [26]. Even though the use of Matrigel is widely extended for scaffolds in neural adhesion and proliferation, Matrigel provides weak mechanical strength and significant degradation over long-term culture, which may limit its use in *in vitro* neural models [29].

Apart from the stiffness of the membranes, biodegradable scaffolds should lose mechanical properties as the tissue mechanical stability is formed, in an equivalent rate. In the field of neural tissue regeneration, Mahoney and Anseth [28] demonstrated that polyethylene glycol hydrogels with a loss of mechanical properties established in 12 days were suitable scaffolds for transplantation in the central nervous system. For neural *in vitro* applications, Lancaster et al. [25] developed an *in vitro* model of cerebral organoid in approximately one month. The neural identity appeared at day 8-10, while brain regions were defined after 20-30 days. Therefore, the rate of membrane structural disintegration could be established in 8%/week for *in vivo* degradation [30], while the neural scaffold materials would ideally degrade via hydrolysis, ion exchange, or through enzymatic reactions over a period of 2–8 weeks [18]. Consequently, we could suggest that the degradation rate of our membranes coincides with the formation of the neural tissue, being more

adequate in the PCL/rGO membranes. Actually, culture assays showed an adequate structural integrity to handle the membranes and promising cell during at least for 21 days (*Chapter 2*). Also, preliminary experiments on neural stem cells have been conducted for 20 days on PCL and PCL/rGO membranes (*Chapter 4*) with similar results.

Figure 3.11 shows the permeate flux of BSA model solution across PCL membranes at 0, 2, 4 and 6 months of degradation. The permeate flux across PCL/rGO was only evaluated at time 0, as PCL/rGO membranes after *in vitro* degradation ( $t > 0$  months) could not withstand the stress created by transmembrane pressure that was applied in the filtration device. In addition, the inset of Figure 3.12 presents the permeate fluxes at steady state.

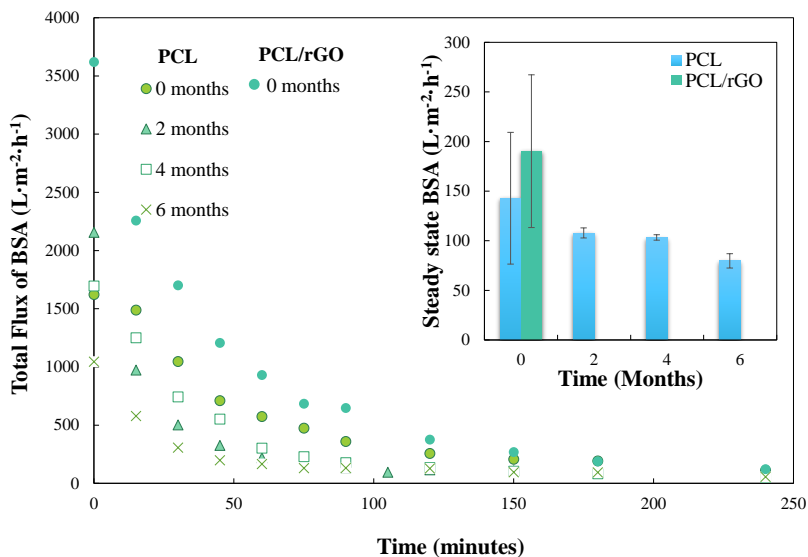


**Figure 3.11.** Average permeate fluxes of BSA model solution during 240 minutes across PCL membranes at 0, 2, 4 and 6 months of degradation and across PCL/rGO membrane at  $t = 0$  (deviation bars not shown for the sake of clarity). Inset shows the values of BSA solution flux at steady state.

Overall, the permeate flux of BSA model solution decreased during the filtration experiment. During the first 2h of filtration, the permeate flux across the PCL membranes suffered a sharp decrease, with a reduction of  $88.1 \pm 2.9\%$  in each point of degradation. Then, the permeate fluxes were maintained at a pseudo steady state, with values of:  $143 \pm 66 > 108 \pm 5 > 103 \pm 3 > 80 \pm 7 \text{ L}\cdot\text{m}^{-2}\cdot\text{h}^{-1}$  at 0, 2, 4, and 6 months of degradation, respectively. Similarly, the permeate flux across the PCL/rGO membranes at time 0 suffered a reduction of  $94.5 \pm 2.4\%$  until the steady state flux was achieved at  $190 \pm 68 \text{ L}\cdot\text{m}^{-2}\cdot\text{h}^{-1}$ .

As it was previously explained in *Chapter 2*, the reduction of the permeate flux during the filtration tests was attributed to the internal fouling. On the contrary, the reduction observed in the permeate fluxes across the PCL membranes during the hydrolytic degradation was considered to be influenced by the loss of structural integrity of the membranes. The filtration tests may induce hydrodynamic pressures, provoking the compaction of the membranes as well as the reduction of the pore size [22]. According to Betahalli et al [31], in spite of the reduced values of steady state fluxes, our fabricated membranes offered sufficient permeate flux to feed more than one layers of cells in a perfusion bioreactor.

### **3.4. Final remarks**

The hydrolytic degradation during a long term period of 12 months of PCL and PCL/rGO membranes was evaluated, in order to study the membrane capacity to act as scaffold in *in vitro* bioreactors. The fabricated membranes continuously degraded under the presence of PBS, simulating *in vitro* culture conditions. Both PCL/rGO membranes and PCL

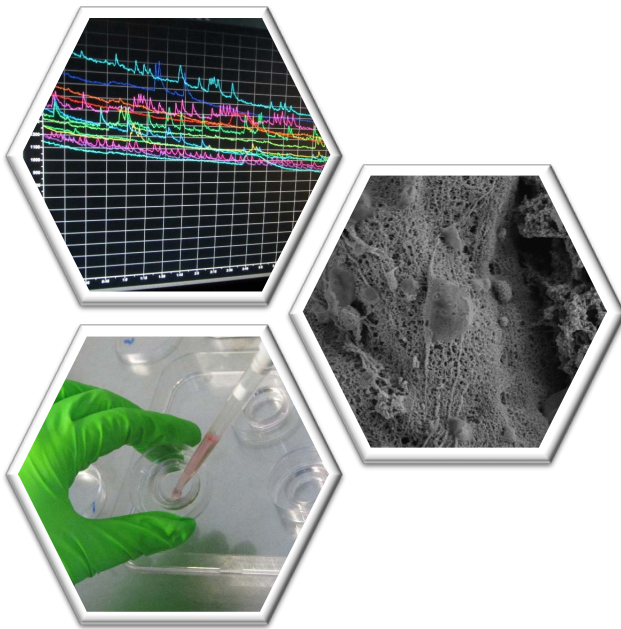
membranes exhibited a fast degradation rate, avoiding the limited applications referred to its slow degradation kinetics. Besides, the introduction of rGO nanomaterials in the PCL matrix slightly accelerated the degradation rate. Nevertheless, the degradation rate of the membranes herein reported would perfectly fit the rate in *in vitro* neural tissue formation that would require around 1 month to be completed.

In addition, the membranes did not alter the cytotoxicity of the buffer solution, as: i) the low amount of acidic products formed by PCL during the hydrolytic degradation of the membranes did not influence the cell proliferation and ii) the rGO nanomaterials preferentially remained immobilized in the polymer matrix of the membrane. Therefore, PCL/rGO membranes were considered promising candidates to be used as scaffolds in perfusion bioreactors.

### 3.5. References

- [1] S. Sánchez-González, N. Diban, A. Urtiaga, *Membranes (Basel)*. **2018**, *8*, 1.
- [2] L. A. Bosworth, S. Downes, *Polym. Degrad. Stab.* **2010**, *95*, 2269.
- [3] M. A. Woodruff, D. W. Huttmacher, *Prog. Polym. Sci.* **2010**, *35*, 1217.
- [4] J. Ferreira, A. Gloria, S. Cometa, J. F. J. Coelho, M. Domingos, *J. Appl. Biomater. Funct. Mater.* **2017**, *15*, 0.
- [5] A. Göpferich, *Biomaterials* **1996**, *17*, 103.
- [6] I. Castilla-Cortázar, J. Más-Estellés, J. M. Meseguer-Dueñas, J. L. Escobar Ivirico, B. Marí, A. Vidaurre, *Polym. Degrad. Stab.* **2012**, *97*, 1241.
- [7] G. P. Sailema-Palate, A. Vidaurre, A. F. Campillo, I. Castilla-Cortázar, *Polym. Degrad. Stab.* **2016**, *130*, 118.
- [8] C. X. F. Lam, M. M. Savalani, S.-H. Teoh, D. W. Huttmacher, *Biomed. Mater.* **2008**, *3*, DOI 10.1088/1748-6041/3/3/034108.
- [9] A. Höglund, M. Hakkarainen, A.-C. Albertsson, *J. Macromol. Sci. Part A Pure Appl. Chem.* **2007**, *44*, 1041.
- [10] Z. X. Meng, W. Zheng, L. Li, Y. F. Zheng, *Mater. Sci. Eng. C*

- 2010**, *30*, 1014.
- [11] S. Mohammadi, S. S. Shafiei, M. Asadi-Eydivand, M. Ardeshir, M. Solati-Hashjin, *J. Bioact. Compat. Polym.* **2017**, *32*, 325.
- [12] E. Murray, B. C. Thompson, S. Sayyar, G. G. Wallace, *Polym. Degrad. Stab.* **2015**, *111*, 71.
- [13] A. E. Hafeman, K. J. Zienkiewicz, A. L. Zachman, H.-J. Sung, L. B. Nanney, J. M. Davidson, S. A. Guelcher, *Biomaterials* **2011**, *32*, 419.
- [14] K. Krishnamoorthy, M. Veerapandian, L. H. Zhang, K. Yun, S. J. Kim, *J. Phys. Chem. C* **2012**, *116*, 17280.
- [15] N. Bölgen, Y. Z. Menceloglu, K. Acatay, I Vargel, E. Piskin, *J. Biomater. Sci. Polym. Edn* **2005**, *16*, 1537.
- [16] S. Lyu, D. Untereker, *Int. J. Mol. Sci.* **2009**, *10*, 4033.
- [17] S. Goenka, V. Sant, S. Sant, *J. Control. Release* **2014**, *173*, 75.
- [18] M. Thomas, S. M. Willerth, *Front. Bioeng. Biotechnol.* **2017**, *5*, 1.
- [19] M. Chen, X. Qin, G. Zeng, *Trends Biotechnol.* **2017**, *35*, 836.
- [20] Y. Zhang, S. F. Ali, E. Dervishi, Y. Xu, Z. Li, D. Casciano, A. S. Biris, *Am. Chemcial Soc.* **2010**, *4*, 3181.
- [21] F. von Burkersroda, L. Schedl, A. Göpferich, *Biomaterials* **2002**, *23*, 4221.
- [22] Q. Zhang, Y. Jiang, Y. Zhang, Z. Ye, W. Tan, M. Lang, *Polym. Degrad. Stab.* **2013**, *98*, 209.
- [23] G. S. Wang, Z. Y. Wei, L. Sang, G. Y. Chen, W. X. Zhang, X. F. Dong, M. Qi, *Chinese J. Polym. Sci.* **2013**, *31*, 1148.
- [24] T. X. Jin, C. Liu, M. Zhou, S. G. Chai, F. Chen, Q. Fu, *Compos. Part A* **2015**, *68*, 193.
- [25] M. A. Lancaster, M. Renner, C.-A. Martin, D. Wenzel, L. Bicknell, M. Hurlles, T. Hofray, J. Perninger, A. Jackson, J. Knoblich, *Nature* **2013**, *501*, 373.
- [26] L. Binan, C. Tendey, G. De Crescenzo, R. El Ayoubi, A. Ajji, M. Jolicoeur, *Biomaterials* **2014**, *35*, 664.
- [27] A. Banerjee, M. Arha, S. Choudhary, R. S. Ashton, S. R. Bhatia, D. V. Schaffer, R. S. Kane, *Biomaterials* **2009**, *30*, 4695.
- [28] M. J. Mahoney, K. S. Anseth, *Biomaterials* **2006**, *27*, 2265.
- [29] X. Wan, S. Ball, F. Willenbrock, S. Yeh, N. Vlahov, D. Koennig, M. Green, G. Brown, S. Jeyaretna, Z. Li, Z. Cui, H. Ye, E. O'Neill, *Sci. Rep.* **2017**, *7*, 1.
- [30] Y. Wang, Y. M. Kim, R. Langer, *J. Biomed. Mater. Res. Part A* **2003**, *66A*, 192.
- [31] N. M. S. Bettahalli, J. Vicente, L. Moroni, G. A. Higuera, C. A. Van Blitterswijk, M. Wessling, D. F. Stamatialis, *Acta Biomater.* **2011**, *7*, 3312.



# *Chapter 4*

## **Influence of graphene-based nanomaterials oxidation state on the differentiation and maturation of human neural progenitor cells behavior**

This chapter was adapted from the manuscript published in “Macromolecular Bioscience”:



S. Sánchez-González, N. Diban, F. Bianchi, H. Ye, A. Urtiaga. Evidences of the effect of GO and rGO in PCL membranes on the differentiation and maturation of human neural progenitor cells. *Macromolecular Bioscience*. 1800195, (2018) 1-8 [1].



## 4.1. Introduction

The development of *in vitro* human neural cell models is progressing due to recent advances in cell research. Although primary cells are still used in tissue engineering, the low proliferative and differentiating potential as well as the invasive nature of cell collection, lead to focus the attention upon the use of stem cells [2,3]. In particular, induced pluripotent stem cells (iPSCs) allow specific cell therapies for the patient, avoiding immune rejections and ethical concerns when using ESCs as a cell source [4].

Our developed poly( $\epsilon$ -caprolactone)/graphene based nanomaterials (PCL/GbNs) membranes revealed preliminary suitable neural cell biocompatibility to be used in *in vitro* neural models using primary cells (*Chapter 2*). However, the ability of these membranes to elicit neural differentiation from stem cells has not been tested yet. Previous studies that investigated the influence of GbN in polymer scaffolds showed promising properties to act as neural cell supports [5–8]. For example, the influence of graphene oxide (GO) enhanced the hydrophilicity of the membrane, which generally provided better affinity for cells [7]. On the contrary, the effect of reduced GO (rGO) improved the electrical conductivity of the scaffolds [5,8], which provided an excellent advantage for neural stimulation as neurons are electrically excitable cells [9,10]. Furthermore, intrinsic properties of GbN such as surface chemistry or nanomorphology may improve the neural cell behavior and response, as they could imply specific interactions between the cells and the material [11].

Based on a report that compared the cell behavior of human neural stem cell cultured on GbN substrates [9], the GbN properties were expected to produce different micro-environmental cues, depending on the nanomaterials distribution over the polymer matrix and their chemical structure that could affect the stem cell fate and the neural response. For instance, they observed higher cell proliferation on GO scaffolds due to its higher hydrophilicity with respect to rGO, while the neural cell differentiation was enhanced by rGO because it was associated to the high electrical conductivity.

The effect of doping PCL membranes with GO or rGO on neural stem cell differentiation and maturation has not been investigated so far. Therefore, the main objective of this chapter was to study the influence of doping PCL membranes with GO or rGO to induce neuronal functionality through differentiated stem cells. The influence of the GO and rGO chemistry in the PCL matrix distribution was characterized and compared via Raman spectroscopy, contact angle measurements and conductivity tests. Cell culture assays were carried out through human iPSCs (hiPSCs)-derived human neural progenitor cell (hNPC) culture. NPCs are cells that have already become lineage committed, resulting in one category of neural component, i.e., glial cells or neurons [12]. However, unlike neural stem cells (NSCs), NPCs have a limited proliferative ability and does not exhibit self-renewal [13]. The hNPCs were characterized in relation to adhesion, proliferation, differentiation and maturation stages.

## 4.2. Materials and methods

### 4.2.1. Characterization of membranes

PCL, PCL/GO and PCL/rGO flat membranes were fabricated using the same procedure as in *Chapter 2*.

Raman spectroscopy analysis of the different membranes was carried out using the same equipment and the same operating conditions explained in *Chapter 2*.

The water contact angle of the dry membranes surface was measured. The method consisted of depositing a drop of ultrapure water on the surface of the membrane. Images were taken right after, and the angle was measured with the software Meazure (C Thing Software) (Figure 4.1).

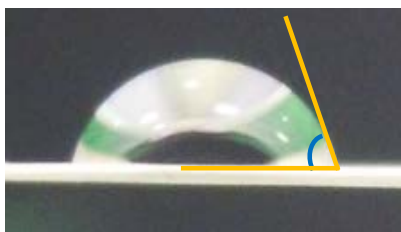


**Figure 4.1.** Example of the water contact angle measurement

The electrical properties along the thickness of PCL, PCL/GO and PCL/rGO membranes were evaluated by electrical impedance measurements, which were carried out in the Department of Physical Chemistry of the University of Valencia (Spain) under the supervision of Prof. Dr. Francisco Vicente Pedrós, Dr. José García Jareño and Dr. Jerónimo Agrisuelas Vallés. Figure 4.2 presents the device employed to execute the experiments. It consisted of a PM 6304 programmable automatic RCL meter (Philips) (Figure 4.2a) that was connected to two

nickel foils with a contact area of  $5 \times 5 \text{ cm}^2$  (Figure 4.2b). The dry membranes were cut, covering the contact area of the foils, and placed between the foils. The system composed of the foils and the membrane was fixed with clamps to avoid any single movement (Figure 4.2c). The nickel foils acted as electrodes, while the membrane was used as electrolyte. The tests were carried out using a variation in the potential frequency of 100, 1000 and 100000 Hz, at room temperature. The impedance analysis provided values of impedance modulus ( $Z$ ) and phase angle ( $\phi$ ).

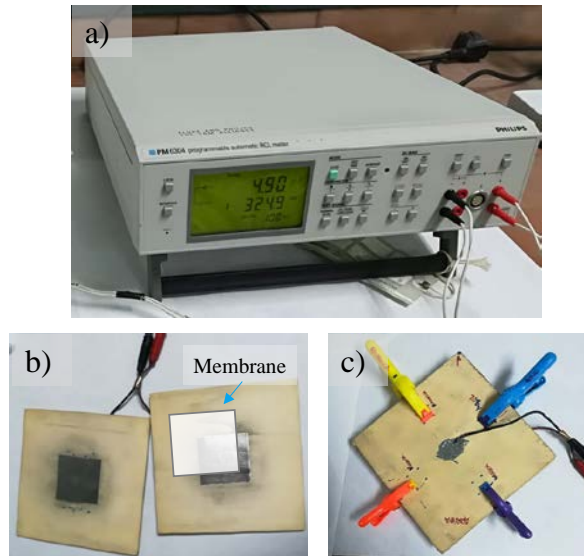


**Figure 4.2.** Equipment used to characterize the electrical properties of the membranes. a) PM 6304 programmable automatic RCL meter (Philips). b) Nickel foils in which membranes are located between the foils, covering its contact area. c) Fixed system used for measuring the electrical impedance.

Equation 4.1 and 4.2 were used to calculate the resistivity of the membranes ( $\delta$ ,  $\Omega \cdot \text{cm}$ ) and the dielectric permittivity ( $\epsilon_r$ ), expressed as:

$$\delta = R \cdot S / l \quad (4.1)$$

$$\varepsilon_r = C \cdot l/S \quad (4.2)$$

where  $l$  is the average thickness of the membrane ( $9.1 \times 10^{-3}$  cm in PCL,  $8.5 \times 10^{-3}$  cm in PCL/GO and  $9.7 \times 10^{-3}$  cm in PCL/rGO, *Chapter 2*) and  $S$  is the contact area ( $25 \text{ cm}^2$ ).  $R$  and  $C$  were calculated from the real  $Z'(\Omega)$  and imaginary  $Z''(\Omega)$  impedance modulus, using Equations 4.3 and 4.4:

$$R = Z' \cdot \cos(\phi) \quad (4.3)$$

$$C = 1/Z'' \cdot \sin(\phi) \cdot \omega \quad (4.4)$$

being  $\omega$  the angular frequency, calculated as  $\omega = 2\pi \cdot f$ .  $f$  is the frequency applied.

#### 4.2.2. Cell culture assays

All reagents were provided by Thermo Fisher, unless otherwise stated.

##### *Scaffold preparation for cell culture assays*

Membrane samples of 15 mm in diameter were used to carry out all the experiments. For membrane sterilization, samples were submerged in 70% ethanol for 1 hour and later, they were introduced in a solution of 1% penicillin-streptomycin (P/S) in PBS for 6 hours. Next, membranes were washed with PBS. Additionally, air-dried membranes were exposed to UV light for 20 minutes in a laminar flow cabinet.

Sterilized samples were kept in 24-well plates (Corning) and polydimethylsiloxane (PDMS) rings were placed on the surface of the membranes to avoid membranes' flotation and to prevent cells from leaving the membranes. Figure 4.3 describes the method followed to

fabricate PDMS rings. First, a silicone elastomer (Sylgard) and a curing agent (Sylgard) were mixed in a mass ratio of 1:10. The mixture was deposited in a 24-well plate and dried inside an oven at 60°C for approximately 6 hours. Then, the obtained disks were punched to form rings with an internal diameter of 11 mm. The final effective surface area of the membranes for cell seeding was 0.95 cm<sup>2</sup>.

Before the seeding of cells, all membrane samples were coated with diluted Matrigel and kept at 37°C for at least four hours. Matrigel dilution was composed of hESC-qualified Matrigel (Corning) that was diluted in ice cold Knockout-DMEM, following the batch-specific manufacturer instructions.

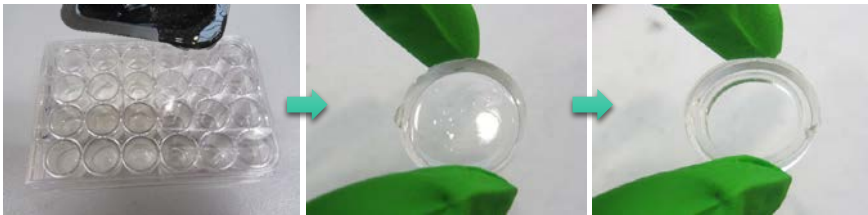


**Figure 4.3.** Procedure to develop PDMS rings.

### ***hiPSCs culture on Tissue Culture Plates (TCP)***

hiPSCs were generated from human dermal fibroblast origin and received at passage 31 from StemBANCC, Oxford.

hiPSCs were thawed and cultured on six-well plates for proliferation with mTeSR medium (StemCell Technologies) supplemented with 1% P/S and 1% RevitaCell. Medium was replaced every 24 hours (minus RevitaCell after 24h). After reaching about 80% confluency of hiPSCs colonies, cells were passaged using versene (0.48nM EDTA) during 3.5 minutes at 37 °C. Next, cells were washed with mTeSR medium and hiPSC

colonies were cut using the STEMPRO EZPassage tool. After that, cells were washed with mTeSR medium and cultured on new Matrigel coated TCP to differentiate hiPSCs into hNPCs.

After day 1, mTeSR medium was substituted with neural induction medium. The medium consisted of KO-DMEM/F:12 supplemented with 10% Knockout serum replacement, 1% non-essential amino acids (NEAA), 1% GlutaMAX, 0.1mM L-ascorbic acid (L-AA, Sigma-Aldrich), 2 $\mu$ M SB431542 (Cell Guidance Systems), 3 $\mu$ M CHIR99021 (Sigma Aldrich), 1 $\mu$ M dorsomorphin (Stem- Cell Tech.) and 1 $\mu$ M compound E (StemCell Tech.). 1% RevitaCell was added exclusively in first 24h.

### ***Proliferation, differentiation and maturation of hNPC cultures***

hNPCs were dissociated from six-well plates when cells reached 80% confluency using accutase. Cells were cultured on Matrigel-coated membranes surface in NPC proliferation medium, which was replaced daily. The cell density used for proliferation assays was  $6.6 \times 10^4$  cells/cm<sup>2</sup>. Cell proliferation was analyzed during 5 days. Proliferation medium consisted of 50% KO-DMEM:F12 and 50% neurobasal medium, supplemented with 1% P/S, 1% B27, 1% N2, 1% NEAA, 1% GlutaMAX, 0.1 mM L-AA, 10 ng/ml b-fibroblast growth factor (b-FGF) and 10 ng/ml epidermal growth factor (EGF, Peprotech).

For cell differentiation, proliferated hNPCs were dissociated using accutase and seeded on the surface of the membranes at a density of  $3.5 \times 10^4$  cells/cm<sup>2</sup> in NPC expansion medium. After day 1, proliferation medium was replaced by differentiation medium. Cells were then kept in differentiation medium that was replaced daily. Cell proliferation was evaluated for 7 days. Differentiation medium consisted of 50% KO-

DMEM:F12 and 50% neurobasal medium, supplemented with 1% P/S, 0.5% B27, 1% N2, 1% NEAA, 1% GlutaMAX , 0.1mM L-AA, 10 $\mu$ M all-trans retinoic acid (Sigma Aldrich), 100ng/ml recombinant Sonic Hedgehog (Peprotech), 0.5 $\mu$ M purmorphamine (Abcam) and 1mM SAG dihydrochloride (Sigma Aldrich).

Differentiated hNPCs were dissociated from six-well plates using accutase and seeded on the membranes at a density of  $5.5 \times 10^4$  cells/cm<sup>2</sup> in maturation medium. The maturation medium was changed daily. Neural maturation was characterized for up to 20 days. Maturation medium consisted of 50% KO-DMEM:F12 and 50% neurobasal medium supplemented with 1% P/S, 1% B27, 1%N2, 1% NEAA, 1% GlutaMAX , 0.1 mM L-AA, 10 ng/ml CNTF (Peprotech), 10 ng/ml BDNF (Peprotech), 10ng/ml NT-3 (Peprotech) and 10 ng/ml GDNF (Peprotech).

Cells cultured in 24-well TCP were used as controls for proliferation, differentiation and maturation assays.

### ***Cell immunocytochemistry and image analysis***

An inverted fluorescence microscope (Nikon TI-E) with multi-wavelength LED excitation and a confocal microscope (Zeiss LSM-710) were used to take microscopic and confocal images of the cells cultured on the membrane surfaces, respectively. All images were analyzed using Fiji (ImageJ) software.

To prepare the samples, membranes with cells were left in fixed solution at 4°C for 20 minutes and incubated at 37°C in permeabilized solution for 30 minutes before staining. Fixed solution was composed of 3.7% paraformaldehyde in PBS (PFA,  $\geq$  36%, Sigma Aldrich), while

permeabilized solution was formed by 0.1% Triton-X (Fisher Biotec), 0.1% Tween-20 (Sigma Aldrich), 1% bovine serum albumin (BSA, Sigma Aldrich) in PBS. Next, cells were stained with primary and second antibodies. First, cells were kept in the primary antibody solution overnight. After that, cells were preserved in secondary antibody solution for 4 hours. Taking both steps, cells were kept in the dark on a gyro rocker (5 rpm) at room temperature. Sox1 and Pax6 (for hiPSCs) or neural specific beta-III tubulin (Tuj1, AbCam) (for hNPCs) primary antibodies were diluted at a concentration of 1:1000 in a 1:10 dilution of the permeabilization buffer. AlexaFluor 488 secondary antibody (LifeTechnologies) was diluted at a concentration of 1:500 in the permeabilization buffer. Besides, NucBlue was added to counterstained cell nuclei (2 drops/ml medium).

### ***Scanning Electron Microscopy (SEM)***

Mature neurons cultured on the membranes were evaluated by SEM images (Zeiss Sigma 300 FEG-SEM) at day 20. SEM images were taken at a voltage of 2kV in high-vacuum mode. Before, membranes with cells were fixed for 20 minutes. The fixed solution consisted of 10 % NaHPO<sub>4</sub> (Sigma Aldrich), 50% PFA and 10 % glutaraldehyde (Sigma Aldrich) in distilled water, adjusted to pH 7.4. Then, membranes were washed with PBS and dehydrated using progressive concentrations of distilled water/ethanol (>99.8%, Honeywell) from 100/0 to 0/100.

### ***Spontaneous Calcium Activity Recording***

The neural activity of mature neurons was evaluated through calcium imaging technique. Cells were analyzed after 20 days of culturing. Mature cells were incubated for 30 minutes in a staining solution composed of Ca<sup>2+</sup>

dye Oregon Green 488 Bapta-1 (4 $\mu$ M) in imaging medium (FluoroBrite-DMEM). Therefore, time-lapse videos were recorded using the inverted fluorescence microscope (Nikon TI-E) with multi-wavelength LED excitation. The conditions of the videos were established at 5 frames per second for 2 minutes, using standard FITC filters. ImageJ was the tool for analyzing the neural activity. Regions of interest related to cell bodies were isolated and changes of fluorescence intensity were measured during time.

### ***Statistical analysis***

Average values were expressed as mean  $\pm$  standard deviation,  $n \geq 3$  for all datasets. The statistical significance was analyzed using one-way ANOVA with Tukey's multiple comparison analysis (GraphPad Prism).  $p$  values less than 0.05 were considered statistically significant.

## **4.3. Results and discussion**

### **4.3.1. Membrane characterization**

Raman spectra of PCL, PCL/GO and PCL/rGO membranes are shown in Figure 4.4a. The surface of the PCL membrane presented the characteristic bands of the PCL polymer [14]. The bands at 1282, 1304, 1417, 1438 and 1469  $\text{cm}^{-1}$  responded to  $\text{CH}_2$  vibrations and the band at 1722  $\text{cm}^{-1}$  to the ester group  $\text{C}=\text{O}$ . The surface of PCL/GO membrane indicated the characteristic bands of the PCL polymer and the G and D bands (1580–1600  $\text{cm}^{-1}$  and 1356  $\text{cm}^{-1}$ , respectively), which are representative of GO Raman spectrum [15,16].

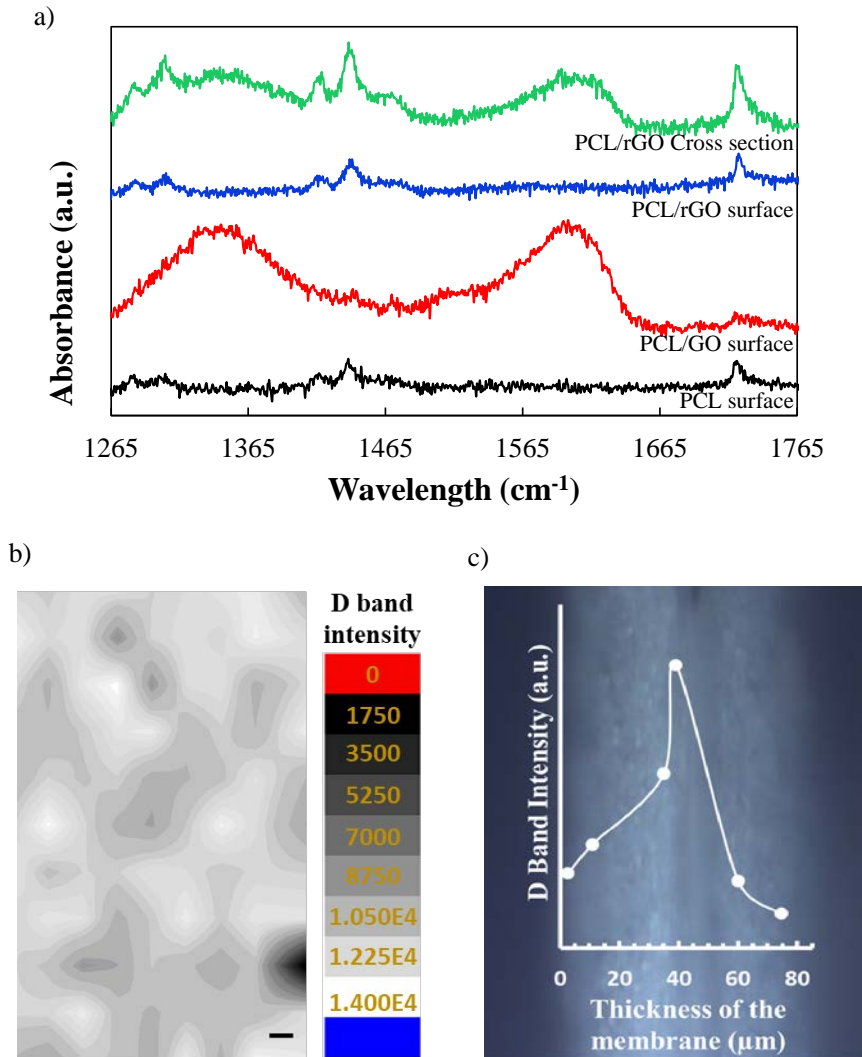


**Figure 4.4.** a) Raman spectra of the PCL and PCL/GO membranes surface, and the PCL/rGO membranes surface and cross section. b) D band intensity surface distribution of GO nanomaterials on PCL/GO membranes. Scale bar= 20  $\mu\text{m}$ . c) D band intensity profile at different points along the thickness of PCL/rGO membrane. Points mean singular experimental data. Lines are only for readers' guidance.

Figure 4.4b represents a  $400 \times 340 \mu\text{m}$  mapping image of the D band intensity of PCL/GO membrane surface. The image described suitable and

homogeneous distribution of GO nanomaterials along the surface of the membrane. On the contrary, the surface of PCL/rGO membrane (Figure 4.4a) did not present neither D nor G bands in the Raman spectrum. Nevertheless, D and G bands were detected in the cross section of the PCL/rGO membranes. Figure 4.4c shows the profile of the D band intensity at different points of the PCL/rGO membrane thickness. Results indicated an increased concentration of rGO nanomaterial towards the center of the PCL/rGO membrane.

The distribution of nanomaterials in the PCL membrane was attributed to the different chemistry of GO and rGO during the non-solvent induced phase separation (NIPS) process. GO had chemically reactive oxygen functionality that conferred a polar behavior. On the contrary, the reduction of GO removed the oxygen groups, which caused a non-polar behavior in rGO. Based on the NIPS technique, the nanomaterials were attracted to the component with similar polarity during the membrane fabrication. The rGO nanomaterials were attracted to the apolar polymer, while the GO nanomaterials were attracted to the polar coagulation bath (isopropanol) [16]. Similarly, Xu et al. [17] observed that GO was distributed on the surface of a polyvinylidene fluoride membrane. They suggested that GO transfer spontaneously to the surface of the membrane to minimize the interface energy during the NIPS process.

The wettability of the membranes was evaluated by measuring the water contact angles. PCL and PCL/rGO presented similar water contact angle ( $96 \pm 11^\circ$  and  $94 \pm 4^\circ$ , respectively). However, the introduction of GO nanoparticles significantly increased the wettability of the membranes in PCL/GO ( $72 \pm 10^\circ$ ) compared to PCL and PCL/rGO. The oxygenated groups of the GO nanomaterials located on the membrane surface provided

the hydrophilic behavior [18,19]. By contrast, the non-polar rGO nanomaterials did not affect the wettability, as the rGO was located inside the membrane. When plain PCL membranes were compared to polymer membranes with low loadings of rGO (up to 1% wt), similar measurements of water contact angles were observed [18,20,21].

Figure 4.5a represents the electrical conductivity along the thickness of the PCL, PCL/GO and PCL/rGO membranes, measured by electrical impedance analysis. The electrical conductivity of the membranes increased with the potential frequency of the alternating current (AC), in agreement with the typical behavior of electrical insulators [22]. The conductivity of PCL at 100 Hz was  $1.8 \times 10^{-9} \pm 1.3 \times 10^{-10} \text{ S} \cdot \text{cm}^{-1}$ . Moreover, Thinh et al. [23] found a conductivity of PCL porous films around  $10^{-10} \text{ S} \cdot \text{cm}^{-1}$  using the four-probe technique. At 100 Hz, the conductivity of the PCL/rGO membranes showed a significant increase of 64% and 141% compared to PCL and PCL/GO, respectively. In contrast, the conductivity of PCL/GO membranes presented a reduction of 32% in comparison to PCL, though not significant.

The differences in the electrical conductivity between the membranes may be caused by the porosity of the membrane [24] and/or by the intrinsic conductivity of the nanomaterials [25,26]. All membranes presented similar porosity and porous structure (*Chapter 2*). Therefore, the diverse electrical properties of PCL/GO and PCL/rGO membranes were attributed to the different intrinsic conductivity of the nanomaterials [20,27], as the electrical conductivity of rGO nanomaterials was widely recognized as being higher than the conductivity of GO (i.e. electrical conductivities of  $0.0206 \text{ S} \cdot \text{m}^{-1}$  in GO and  $2420 \text{ S} \cdot \text{m}^{-1}$  in rGO were reported by Stankovich et al. [25]).

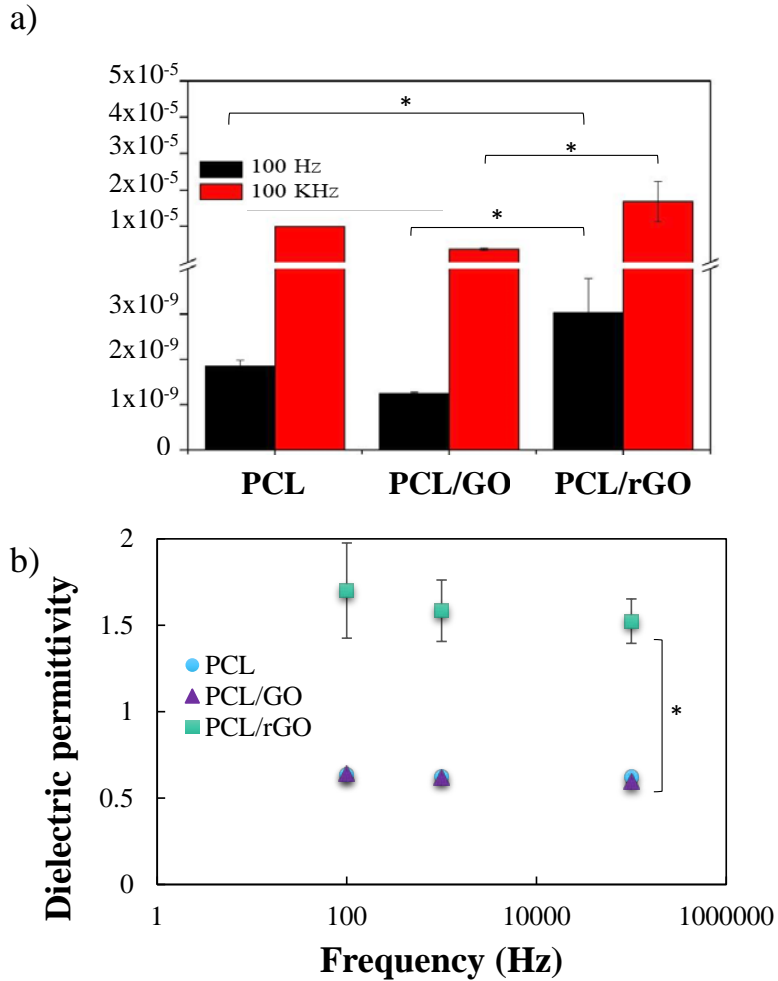


**Figure 4.5.** a) Electrical conductivity along the thickness of the membranes measured at 100 and 100 KHz. b) Relative dielectric permittivity at 100, 1000 and 100000 Hz. Statistical analysis were carried out using one way ANOVA with Tukey’s multiple comparison test (\*= $p > 0.05$ ).

Dielectric permittivity along the thickness of the membranes is illustrated in Figure 4.5b at different potential frequencies. PCL and PCL/GO membranes achieved similar relative dielectric permittivity

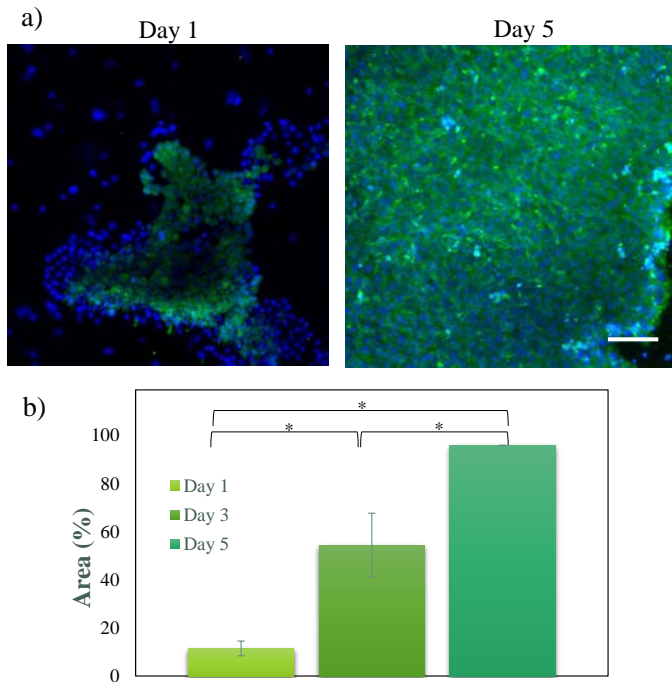
independently of the frequency used. Meanwhile, the relative dielectric permittivity of PCL/rGO membranes presented significant statistical differences ( $p > 0.05$ ) at any frequency in the range tested compared to PCL and PCL/GO. The higher dielectric permittivity observed in PCL/rGO was related to a higher polarizability of the membranes, as Fan et al. stated [28]. Moreover, a constant dielectric permittivity with frequency was attributed to situations in which graphene loading was below the electrical percolation threshold [28].

### **4.3.2. Proliferation and differentiation of hiPCs culture**

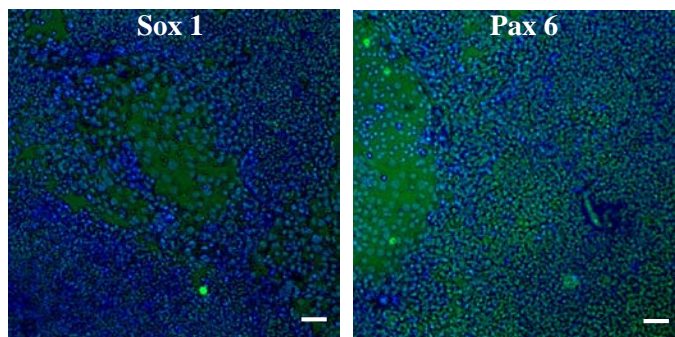
Before seeding the hNPCs on the membranes, tests of hiPSCs proliferation and differentiation were conducted in order to verify the suitable differentiation of hiPSCs into hNPC.

Figure 4.6 and 4.7 present the proliferated and differentiated hiPSCs cultured on TCP, respectively. Microscopic images (Figure 4.6a) showed a progressive formation of hiPSCs colonies after day 1, 3 and 5. Alkaline phosphatase was used to identify hiPSCs. The hiPSCs colonies were quantified by measuring the TCP area occupied by cells (Figure 4.6b). Results demonstrated that hiPSCs proliferated from day 1 to day 5.

Figure 4.7 presents microscopic images of hiPSC colonies that were differentiated into neural rosettes after being in differentiation medium for 7 days. Cells exhibited Sox1 and Pax6 expression, demonstrating the hiPSCs differentiation into hNPCs.



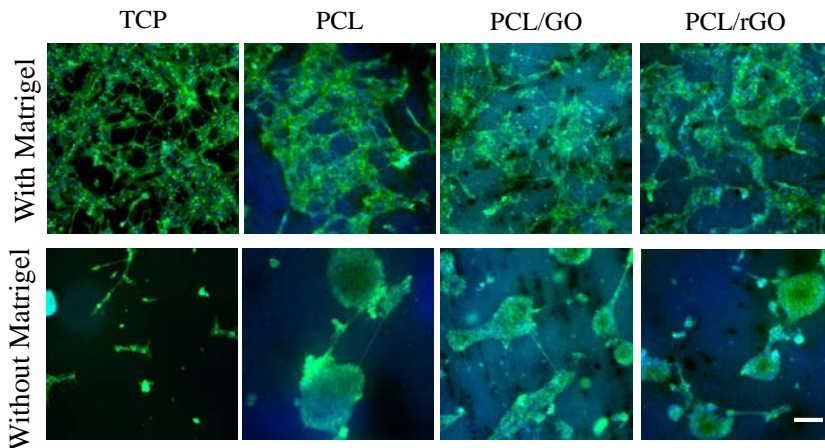
**Figure 4.6.** a) Microscopic images of proliferated hiPSCs cultured on TCP using alkaline phosphatase (green) to identify hiPSCs and Nucblue (blue) to detect cell nuclei. Scale bar=100  $\mu$ m. b) Quantitative analysis of proliferated hiPSCs. \*= $p$ <0.05, using one-way ANOVA with Tukey's multiple comparison test.



**Figure 4.7.** Neural rosettes formed by differentiated hiPSCs cultured on TCP after 7 days. Differentiated cells were discriminated by expression of active transcription factors in neural progenitors (Sox1 and Pax6, green color). Nucblue stained the cell nuclei. Scale bar=100  $\mu$ m.

### 4.3.3. Proliferation, differentiation and maturation of hNPCs culture

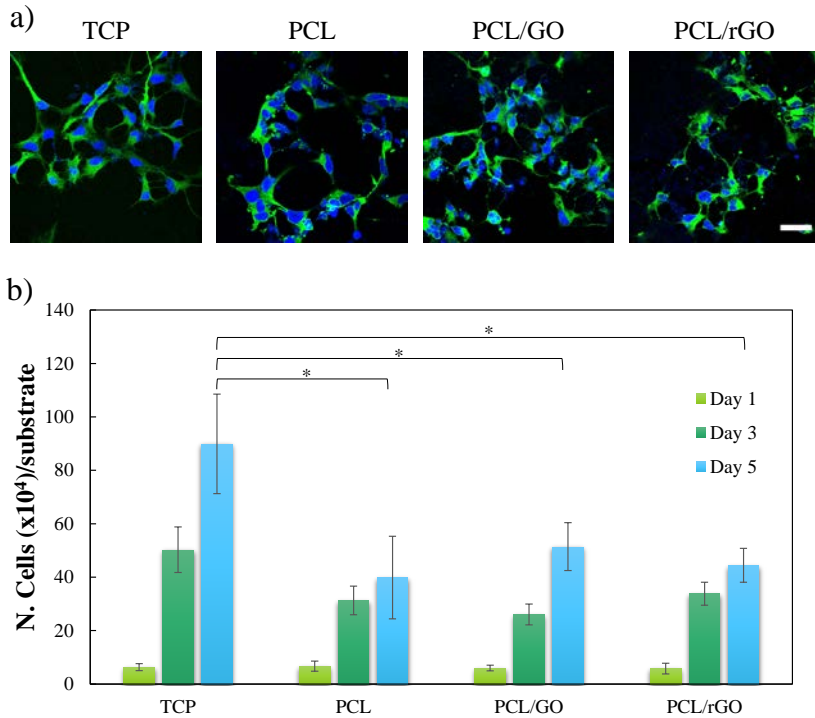
Figure 4.8 presents microscopic images of hNPCs adhesion cultured on Matrigel coated and non-coated substrates. Results demonstrated the importance of using Matrigel to homogeneously distribute cells, without the formation of cell clusters. Specifically, the cell adhesion to non coated PCL/GO membranes slightly enhanced over PCL and PCL/rGO membranes. That behavior was potentially attributed to the lower water contact angle of PCL/GO membranes, in agreement with other works [6,7,18].



**Figure 4.8.** Microscopic images of hNPCs cultured on Matrigel-coated and non-coated substrates. Scale bar represents 100  $\mu\text{m}$ .

Figure 4.9a shows confocal images of hNPCs on the surface of Matrigel-coated TCP, PCL, PCL/GO and PCL/rGO substrates after one day of culture. Cells were stained with Tuj1, which is a cell marker that recognizes a neuron-specific class  $\beta$ -III tubulin.  $\beta$ -III tubulin is a cytoskeletal protein presented in the soma and in all neuronal processes [29]. At day 1, the cell adhesion was similar to all the substrates. Cells were

uniformly distributed on the surface of the substrates with a proper phenotype. The similar cell attachment at day 1 was attributed to the Matrigel coating employed, which was necessary to promote hNPCs adhesion [30].



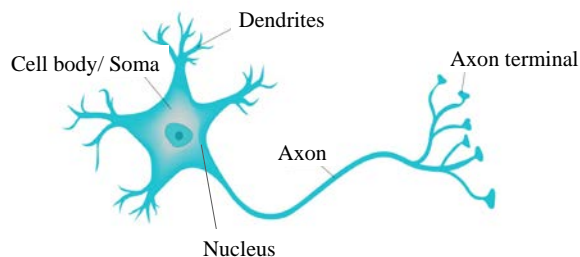
**Figure 4.9.** a) Confocal images of hNPC cultured on Matrigel coated substrates after day 1 of proliferation. Scale bar=50  $\mu$ m. Cells were stained with Tuj1 (green) and Nucblue (blue) to analyze the microtubules of neuron cells and the cell nuclei, respectively. b) Progression of hNPC density on TCP, PCL, PCL/GO and PCL/rGO membranes at day 1, 3 and 5. Statistical analysis were carried out using one way ANOVA with Tukey's multiple comparison test (\*= $p > 0.05$ ).

Figure 4.9b shows the hNPCs proliferation seeded on TCP, PCL, PCL/GO and PCL/rGO membranes at day 1, 3 and 5, analyzed by counting the cell nuclei from microscopic images. The number of cells progressively

increased in all the substrates. Quantitatively, the cell density at day 1 barely changed in all the substrates ( $\sim 6 \times 10^4$  cells/ substrate). However, cells on TCP substrates showed a significant cell growth with respect to the membranes at day 3 ( $50 \times 10^4 \pm 9 \times 10^4$  cells/ substrate) and at day 5 ( $90 \times 10^4 \pm 19 \times 10^4$  cells/ substrate). In contrast to the high surface porosity of the membranes, the significant higher cell density on TCP could be attributed to its smooth surface, which promotes the direct and easy cell-to-cell contact.

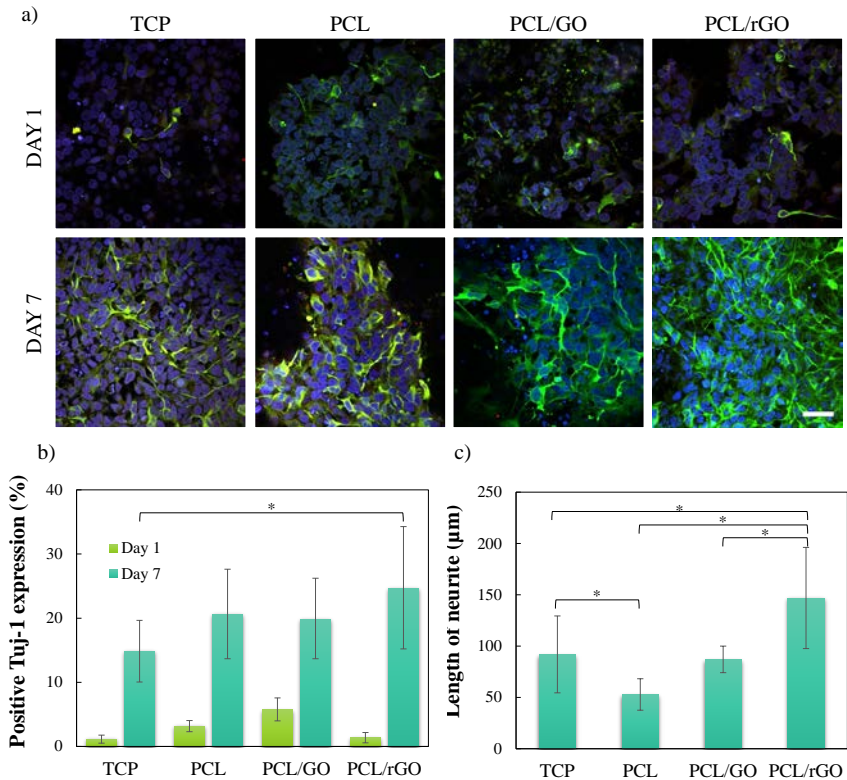
Comparing the membrane effect on cell proliferation, the cell density at day 5 was higher in PCL/GO ( $51 \times 10^4 \pm 9 \times 10^4$  cells/ substrate) than PCL/rGO ( $44 \times 10^4 \pm 6 \times 10^4$  cells/ substrate) and PCL ( $40 \times 10^4 \pm 15 \times 10^4$  cells/ substrate). According to other works [6–8,18,31], the presence of GbN in the polymer matrix enhanced the cell density. Wang et al. [31] stated that thanks to the high surface area, the elastic modulus, the stiffness and the presence of wrinkles and ripples on graphene sheets, there was a better cell attachment and proliferation.

Figure 4.10 indicates the structure and components of a neuron. The neuron is composed of nucleus, axon, axon terminals, dendrites and soma. Moreover, any projection from the cell body of a neuron, considering both axons and dendrites, is called neurites.



**Figure 4.10.** Overview of a neuron structure

Figure 4.11a presents the confocal images of the differentiation of hNPCs into neurons, cultured on TCP, PCL, PCL/GO and PCL/rGO at day 1 and day 7. Images demonstrate the hNPCs differentiation towards neural lineage, since the Tuj1 expression increased from day 1 to day 7.



**Figure 4.11.** hNPCs differentiation cultured on TCP, PCL, PCL/GO and PCL/rGO substrates. a) Confocal images of differentiated hNPCs at day 1 and 7. Neuron cell microtubules and cell nuclei were stained with Tuj1 (green) and Nucblue (blue), respectively. Scale bar=50  $\mu\text{m}$ . b) %Positive Tuj-1 expression of hNPCs after 1 and 7 days of differentiation. c) Length of neurites of differentiated hNPCs at day 7. Statistical analysis was evaluated only at the last day of the experiment using one-way ANOVA with Tukey's multiple comparison test (\*= $p < 0.05$ ).

In particular, the presence of rGO nanomaterials in the PCL matrix significantly encouraged the neurite outgrowth compared to the other

substrates. Figure 4.11b and 4.11c present the percentage of Tuj1-expressing cells and the average length of neurites obtained from confocal images analyses. Both analyses agreed on the significantly accelerated differentiation of hNPCs cultured on the PCL/rGO membranes with respect to TCP in terms of Tuj1 expression (Figure 4.11b) and to TCP, PCL and PCL/GO in terms of length of neurite (Figure 4.11c). In fact, the obtained neurite sprouting showed great elongations, in accordance with other works that observed average neurite length of 70-147  $\mu\text{m}$  [29,32]. Comparing to TCP, the better hNPCs differentiation on membranes could be attributed to its porous structure, which might provide a better platform for intra-cellular communication, migration of nutrients and cellular metabolism [33].

Park et al. [34] found that graphene based scaffolds provided more favorable microenvironments for human NSC (hNSC) differentiation and promoted neural differentiation of hNSCs over glia differentiation, albeit the mechanism is not clear. Akhavan [35] revised the literature looking for different possible mechanisms to explain the graphene-based materials effect on accelerating stem cell differentiation, including morphological, mechanical, electrical and chemical aspects of the graphene-based nanomaterials. Our fabricated PCL/GbN membranes did not present significant changes neither in the mechanical properties nor in the surface morphology compared to PCL membranes. Therefore, the inductive effect on cell differentiation was discarded considering mechanical or topographical mechanism.

Taking into account the surface chemistry effect of the nanomaterials on the membranes, the NIPS technique allowed the selective location of the nanomaterials to be on the surface of the membranes (GO) or in the

membrane matrix (rGO) (Figure 4.4). As the PCL/rGO membranes did not contact directly to the cells, the cell-nanomaterial interaction was not considered to be favored by the surface chemistry mechanism. Therefore, the electrical properties of the nanomaterials seemed to be the most likely cause of the different hNPCs behavior found on the PCL/GbN. The PCL/rGO membrane displayed higher electrical conductivity (Figure 4.5a) and higher dielectric permittivity (Figure 4.5b) than PCL and PCL/GO. Akhavan et al. [36] showed that the high capability of rGO to transfer electrons was core to improve the hNSCs differentiation. This would explain the higher neural differentiation and the significantly higher neurite length observed in PCL/rGO membranes with respect to the PCL/GO membranes.

Figure 4.12 shows SEM images of hNPCs-derived neurons cultured on the membranes after 20 days. Overall, cell nuclei were observed on all the membranes. Cells on PCL/GO and PCL/rGO membranes indicated a suitable neural structure with extensive neurite growth, including a great concentration of dendrites and axons (neurites). On the contrary, PCL membranes barely showed neurites, in agreement with the low neurite length observed in Figure 4.11c.

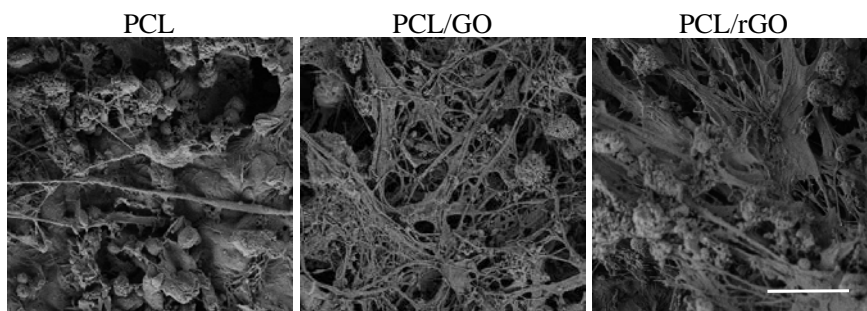


**Figure 4.12.** SEM images of hNPCs -derived neurons cultured on PCL, PCL/GO and PCL/rGO membranes after 20 days. Scale bar = 10  $\mu$ m.

The maturation of differentiated hNPCs-derived neurons was evaluated throughout calcium imaging technique. The technique is based on measuring the voltage differences from inside to outside the membrane cell. The neural activity is commonly known as nerve impulses or action potentials, and mature neurons can generate them spontaneously. Initially, the neuron has a negative potential. When a nerve impulse is generated, the calcium channels of the membrane cell open. Then, the free calcium from the imaging media goes into the cell, producing a voltage increase and a fluorescence response due to the chemical indicator BAPTA.

Figure 4.13 presents the neural electrical response of hNPC-derived neurons cultured on TCP, PCL/GO and PCL/rGO membranes after 20 days. Figure 4.13a shows an example of the results obtained from the video analyses. Results proved the presence of neural activity, as each spike represented the firing of a mature neuron. Figure 4.13b represents the number of active neurons on PCL/GO and PCL/rGO over the number of active neurons on TCP. Finally, Figure 4.13c features the intensity of the cell nerve impulses.

Overall, PCL/GO and PCL/rGO membranes obtained higher number of active neurons and significantly greater magnitude of neuron activity in comparison to TCP. On the one hand, the number of active neurons in PCL/GO was  $1.9 \pm 0.8$  neurons/ active neurons on TCP, which was slightly improved compared to the number of active neurons in PCL/rGO ( $1.1 \pm 0.3$  neurons/ active neurons on TCP). On the other hand, PCL/rGO membranes provided significantly higher magnitude of neuron activity than TCP and PCL/GO substrates.

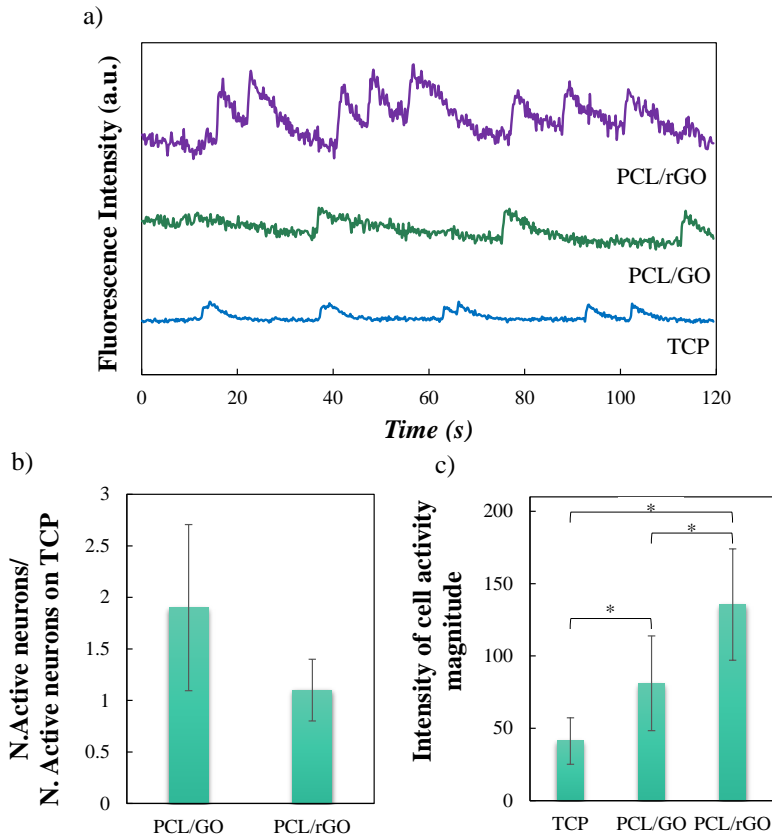


**Figure 4.13.** Calcium imaging analysis of mature hNPCs cultured on TCP, PCL/GO and PCL/rGO substrates after 20 days. a) Fluorescence intensity of a neural-like cell caused by the produced spontaneous nerve impulses during time. b) Number of neural-like cell that generated nerve impulses in two minutes of recording compared to TCP ( $32 \pm 11$  active neurons/mm<sup>2</sup>). c) Magnitude of neural-like cell spike. \* =  $p < 0.05$  using one-way ANOVA with Tukey's multiple comparison test.

The enhanced neuron activity of PCL/GO and PCL/rGO was attributed to the presence of GbNs. For instance, Serrano et al. [37] indicated that the oxygen functional groups of GO could be linked with biologically active moieties, which specifically serve directing neural regeneration. Furthermore, Park et al. [34] detected that genes related to the calcium

signaling pathway were significantly upregulated when hNSCs were differentiated on graphene. In addition, some reports stated that the electrical properties of graphene promoted spontaneous neuron activity [34,38,39].

The position of the GbNs in our fabricated membranes could also affect the neural activity. As GO was distributed on the surface of the membranes, neurons could easily get into contact with the GO nanomaterials. On the contrary, the access of neurons to rGO nanoplatelets located inside the PCL/rGO membranes was limited, as rGO was located in the central part of the membrane wall. As a result, PCL/GO produced higher number of neurons with spontaneous nerve impulses than PCL/rGO. However, neurons cultured on PCL/rGO showed higher spike magnitude than those cultured on PCL/GO, a behavior that was attributed to the higher conductive constitution of rGO [38,40].

#### **4.4. Final remarks**

The influence of GbNs in PCL porous membranes was evaluated in terms of the nanomaterial spatial distribution in the membrane, electrical conductivity of the membranes, compatibility with neural cell growth and functional differentiation. Raman spectra analyses demonstrated the different distribution inside the membrane matrix. The GO nanomaterials were located on the surface of the membrane, while rGO particles were positioned inside the membrane wall with preferential accumulation in the center of the membrane thickness. This behavior was attributed to the nanomaterials polarity, which induced different phase separation during membrane fabrication. The hydrophilicity of PCL/GO membranes was significantly higher than PCL and PCL/rGO membranes. Meanwhile, the

PCL/rGO membranes presented significant improved electrical conductivity and dielectric permittivity with respect to PCL and PCL/GO membranes at low voltage frequencies during the electrical impedance measurements.

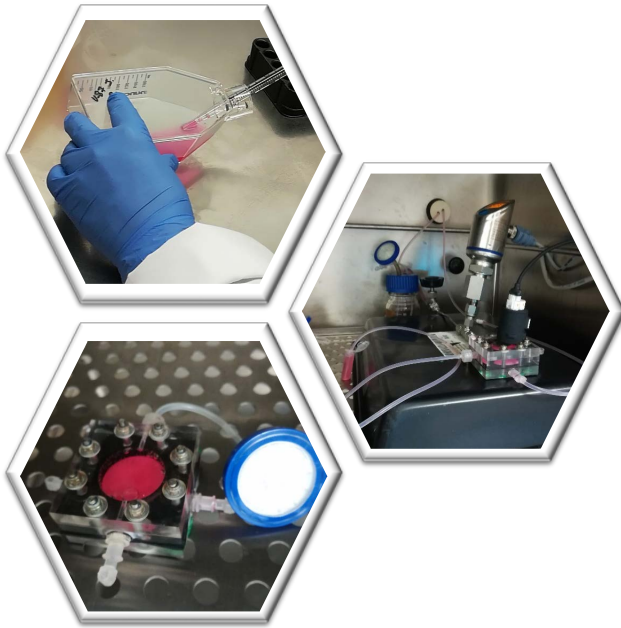
The proliferation of hNPCs cultured on the membranes was slightly improved for membranes that included GbN. Moreover, the differentiation and maturation of hNPCs was enhanced in PCL/GO and PCL/rGO, in comparison to the TCP substrates. The location of GO on the membrane surface easily allowed the direct GO-cell contact. In consequence, the number of electrically active cells during maturation increased. Albeit rGO was embedded in the membrane center, the differentiation and the magnitude of activity spikes of neurons were significantly higher than TCP and PCL/GO supports. That behavior was attributed to the potential of rGO to induce electro-activity on neural cells.

In conclusion, notwithstanding the low nanomaterial concentration used (0.67 wt% theoretical concentration in the solid membrane substrate), results demonstrated that GbNs promoted hNPC differentiation and maturation. The introduction of rGO nanomaterials in PCL membranes provided the best NPC differentiation and magnitude of neural activity spikes during maturation, being related to the better electrical properties of PCL/rGO membranes. Therefore, PCL/rGO membranes could be highly considered as promising materials for scaffolds in neural tissue regeneration.

## 4.5. References

- [1] S. Sánchez-González, N. Diban, F. Bianchi, H. Ye, A. Urriaga, *Macromol. Biosci.* **2018**, 1800195, 1800195.
- [2] D. Howard, L. D. Buttery, K. M. Shakesheff, S. J. Roberts, *J. Anat.* **2008**, 213, 66.
- [3] J. M. Polak, A. E. Bishop, *Ann. N. Y. Acad. Sci.* **2006**, 1068, 352.
- [4] A. Wang, Z. Tang, I.-H. Park, Y. Zhu, S. Patel, G. Q. Daley, L. Song, *Biomaterials* **2011**, 32, 5023.
- [5] S. Sayyar, E. Murray, B. C. Thompson, S. Gambhir, D. L. Officer, G. G. Wallace, *Carbon N. Y.* **2013**, 52, 296.
- [6] J. Song, H. Gao, G. Zhu, X. Cao, X. Shi, Y. Wang, *Carbon N. Y.* **2015**, 95, 1039.
- [7] K. Zhang, H. Zheng, S. Liang, C. Gao, *Acta Biomater.* **2016**, 37, 131.
- [8] N. Golafshan, M. Kharaziha, M. Fathi, *Carbon N. Y.* **2017**, 111, 752.
- [9] O. Akhavan, E. Ghaderi, E. Abouei, S. Hatamy, E. Ghasemi, *Carbon N. Y.* **2014**, 66, 395.
- [10] S. R. Shin, Y. C. Li, H. L. Jang, P. Khoshakhlagh, M. Akbari, A. Nasajpour, Y. S. Zhang, A. Tamayol, A. Khademhosseini, *Adv. Drug Deliv. Rev.* **2016**, 105, 255.
- [11] S. Morelli, S. Salerno, A. Piscioneri, L. De Bartolo, *Compr. Membr. Sci. Eng. II* **2017**, 4, DOI 10.1016/B978-0-12-409547-2.12260-7.
- [12] Y. D. Teng, F. N. C. Santos, P. M. Black, D. Konya, K. I. Park, R. L. Sidman, E. Y. Snyder, in *Princ. Regen. Med.*, **2008**, pp. 300–317.
- [13] B. A. Reynolds, R. L. Rietze, *Nat. Methods* **2005**, 2, 333.
- [14] A. Weselucha-Birczyńska, M. Świętek, E. Sołtysiak, P. Galiński, Ł. Płachta, K. Piekara, M. Błazewicz, *Analyst* **2015**, 140, 2311.
- [15] M. J. Allen, V. C. Tung, R. B. Kaner, *Chem. Rev.* **2009**, 110, 132.
- [16] D. Chen, H. Feng, J. Li, *Chem. Rev.* **2012**, 112, 6027.
- [17] Z. Xu, J. Zhang, M. Shan, Y. Li, B. Li, J. Niu, B. Zhou, X. Qian, *J. Memb. Sci.* **2014**, 458, 1.
- [18] S. Kumar, S. Raj, E. Kolanthai, A. K. Sood, S. Sampath, K. Chatterjee, *ACS Appl. Mater. Interfaces* **2015**, 7, 3237.
- [19] B. Chaudhuri, D. Bhadra, L. Moroni, K. Pramanik, *Biofabrication* **2015**, 7, 015009.
- [20] S. G. Rotman, Z. Guo, D. W. Grijpma, A. A. Poot, *Polym. Adv. Technol.* **2017**, 28, 1233.
- [21] A. M. Pinto, S. Moreira, I. C. Gonçalves, F. M. Gama, A. M.

- Mendes, F. D. Magalhães, *Colloids Surfaces B Biointerfaces* **2013**, *104*, 229.
- [22] T. Nezakati, A. Tan, A. M. Seifalian, *J. Colloid Interface Sci.* **2014**, *435*, 145.
- [23] P. X. Thinh, C. Basavajara, J. K. Kim, D. S. Huh, *Polym. Compos.* **2012**, *33*, 2159.
- [24] B.-H. Kim, K. S. Yang, *J. Ind. Eng. Chem.* **2014**, *20*, 3474.
- [25] S. Stankovich, D. A. Dikin, R. D. Piner, K. A. Kohlhaas, A. Kleinhammes, Y. Jia, Y. Wu, *Carbon N. Y.* **2007**, *45*, 1558.
- [26] S. Goenka, V. Sant, S. Sant, *J. Control. Release* **2014**, *173*, 75.
- [27] J. R. Potts, D. R. Dreyer, C. W. Bielawski, R. S. Ruoff, *Polymer (Guildf)*. **2011**, *52*, 5.
- [28] P. Fan, L. Wang, J. Yang, F. Chen, M. Zhong, *Nanotechnology* **2012**, *23*, 8pp.
- [29] S. Morelli, A. Piscioneri, A. Messina, S. Salerno, M. B. Al-Fageeh, E. Drioli, L. De Bartolo, *J. Tissue Eng. Regen. Med.* **2015**, *9*, 106.
- [30] Z. He, S. Zhang, Q. Song, W. Li, D. Liu, H. Li, M. Tang, R. Chai, *Colloids Surfaces B Biointerfaces* **2016**, *146*, 442.
- [31] W. Wang, G. Caetano, W. S. Ambler, J. J. Blaker, M. A. Frade, P. Mandal, C. Diver, P. Bártolo, *Materials (Basel)*. **2016**, *9*, 992.
- [32] S. Morelli, A. Piscioneri, S. Salerno, F. Tasselli, A. Di Vito, G. Giusi, M. Canonaco, E. Drioli, L. De Bartolo, *J. Mater. Sci. Mater. Med.* **2012**, *23*, 149.
- [33] B. Mammadov, M. Sever, M. O. Guler, A. B. Tekinay, *Biomater. Sci.* **2013**, *1*, 1119.
- [34] S. Y. Park, J. Park, S. H. Sim, M. G. Sung, K. S. Kim, B. H. Hong, S. Hong, *Adv. Mater.* **2011**, *23*, H263.
- [35] O. Akhavan, *J. Mater. Chem. B* **2016**, *4*, 3169.
- [36] O. Akhavan, E. Ghaderi, *J. Mater. Chem. B* **2014**, *2*, 5602.
- [37] M. C. Serrano, J. Patiño, C. García-Rama, M. L. Ferrer, J. L. G. Fierro, A. Tamayo, J. E. Collazos-Castro, F. del Monte, M. C. Gutiérrez, *J. Mater. Chem. B* **2014**, *2*, 5698.
- [38] R. Guo, S. Zhang, M. Xiao, F. Qian, Z. He, D. Li, X. Zhang, H. Li, X. Yang, M. Wang, R. Chai, M. Tang, *Biomaterials* **2016**, *106*, 193.
- [39] M. Tang, Q. Song, N. Li, Z. Jiang, R. Huang, G. Cheng, *Biomaterials* **2013**, *34*, 6402.
- [40] S. Ryu, B.-S. Kim, *Tissue Eng. Regen. Med.* **2013**, *10*, 39.



# *Chapter 5*

**Design and preliminary testing of a perfusion poly( $\epsilon$ -caprolactone)/reduced graphene oxide membrane bioreactor for cell cultures in dynamic conditions**



## 5.1. Introduction

Bioreactors present ideal controlled microenvironments to develop artificial tissues under *in vitro* conditions, including controlled pH, carbon dioxide (CO<sub>2</sub>) concentration and/or temperature, as well as content of nutrients, growth factors, and sterility [1]. Furthermore, bioreactors have been considered suitable devices to provide cells with intrinsic mechanical stimuli such as fluid shear stress or hydrostatic pressure [2]. These mechanical stimuli can affect positively the cell behavior. For example, Jaasma and O'Brien [3] studied the osteoblast cell behavior using a flow perfusion bioreactor (see *Chapter 1*) with intermittent fluid flow pattern with the propose of offering mechanical stimulation. They observed that mechanical stimuli were beneficial in cases of early-stage bone formation, at the same time cell viability was maintained.

Generally, neural cells have been reported to respond positively to different external stimulatory cues [4,5]. For instance, soluble molecules such as nerve growth factors or retinoic acids can induce neural cell differentiation [5]. Moreover, the electrical stimulation on neural tissues enhances the spontaneous regeneration after neurological injuries [6]. Furthermore, the micro-patterned substrates and mechanical stimuli offer improvements on the neurite guidance and outgrowth, which are important to restore and regulate the neuronal function [7–10]. For instance, Morelli et al. [10] analyzed the influence of a micro-patterned membrane of poly(L-lactic acid) on outgrowth and orientation of hippocampal neuronal cells. They found improved neurite extension guidance, including higher orientation and higher ordered neuronal cell matrix when compared to the non-patterned membrane. In another work,

Kim et al. [9] evaluated the introduction of mechanical stimuli in the form of fluid-induced shear stress and micro-patterned substrate with microfibers and its effects on neurite outgrowth. As a result, suitable and promising neurite outgrowth and alignment of neurons were found when they employed microfibers as cell support and low fluid-induced shear stress.

The shear stress produced by the mechanical stimuli is recognized to influence the physiology of several tissues, as it affects the cellular mechanoreception (e.g., ion channels, plasma membrane receptors) and response (e.g., intracellular calcium, nitric oxide production, cytoskeletal remodeling) [2,11,12].

In this chapter, a home-made perfusion PCL/rGO membrane bioreactor was designed and used to generate mechanical stimuli in the form of fluid-induced shear stress to evaluate the potential improvement on cell response. In addition to the intrinsic chemical cue induced by the rGO presence in the membrane, the perfusion bioreactor introduced mechanical stimuli under dynamic conditions. Dynamic conditions provided continuous replacement of nutrients and oxygen across the PCL/rGO membrane to the cell culture. Moreover, the culture medium transported through the membrane produced mechanical stimuli in the form of shear stress across the cells that were seeded on its top surface. During the experimental analysis, the temperature, the CO<sub>2</sub> supply and the flow rate were fixed. Meanwhile, the pressure exerted in the system and the oxygen (O<sub>2</sub>) concentration of the medium were monitored. The feed and permeate streams were collected periodically to quantify any concentration change of key nutrient and metabolite molecules. Besides, the potential effect of the shear stress on the morphological response of

glioblastoma cells was examined by confocal imaging.

## 5.2. Materials and methods

### 5.2.1. Perfusion membrane bioreactor

Figure 5.1a and 5.1b present the perfusion membrane bioreactor used to characterize cell cultures under dynamic conditions. It consisted of a feed reservoir that contained the feed solution. The solution was pumped through the perfusion cell using a peristaltic pump (Minipuls 3, Gilson). The perfusion cell (Figure 5.1c) had a total volume capacity of 8.2 mL (2.7 mL in the feed compartment and 5.5 mL in the cell compartment) and an effective filtration area ( $A_e$ ) of 6.2 cm<sup>2</sup>. It was made of a non-toxic and rigid resin. Besides, it was transparent to facilitate the incorporation of online optical measurement instruments whenever needed. The cell was composed of three main pieces: first, the chamber located at the bottom (feed compartment). Second, the chamber placed in the middle that presented a cavity to allow the cells to grow (cell compartment) and finally, the cover. A PCL/rGO membrane fabricated by non-solvent induced phase separation was located between both chambers to act as cell support. Also, a Teflon<sup>®</sup> ring was used to avoid liquid leakages. The perfusion bioreactor acted as a membrane microfiltration module working in tangential flow configuration. This means that the feed solution circulated in parallel to the membrane feed side (Figure 5.1d). The system included a pressure indicator (B 40.5052.0, JUMO DELOS SI) and a valve. Both elements were located at the outlet port of the feed compartment. The valve regulated the transmembrane pressure that was monitored by the pressure indicator. The transmembrane pressure exerted the driving force to split the feed solution into two fluid streams, the

permeate (fluid that crossed the membrane) and the retentate (fluid that remained in the feed compartment of the membrane module). Then, both permeate and retentate were recirculated to the feed reservoir.

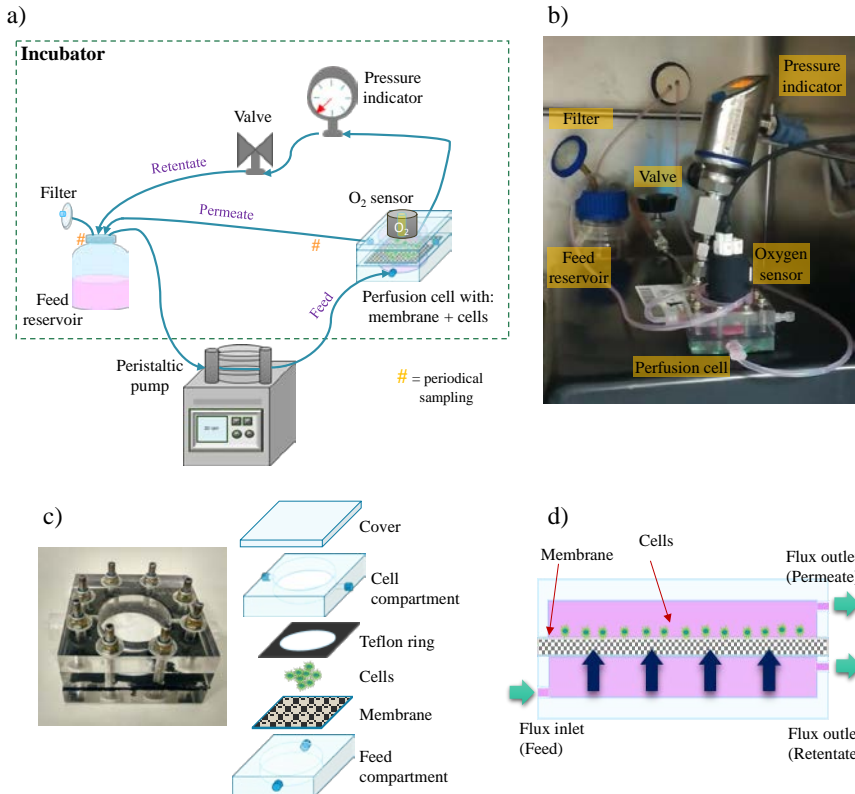


**Figure 5.1.** a) Scheme of the perfusion bioreactor. b) Perfusion bioreactor in the incubator. c) Picture of assembled perfusion cell and scheme of the separated pieces of the perfusion bioreactor. d) Diagram of the flux direction under dynamic conditions in the perfusion cell. The picture was not scaled.

In addition, an oxygen sensor (BlueBlink O<sub>2</sub> sensing system, Ebers Medical Technology S.L.) was set in the cell compartment to monitor the O<sub>2</sub> concentration that fed the cells in the permeate. All the components of the perfusion membrane bioreactor system were placed inside an incubator, except for the peristaltic pump that was located outside. The

feed reservoir integrated a 0.45  $\mu\text{m}$  syringe filter to open up the oxygenation of the perfusion system.

The components of the perfusion membrane bioreactor were sterilized using different protocols: 70% ethanol was sprayed to sterilize externally the valve, the pressure indicator, the  $\text{O}_2$  sensor and the PCL/rGO membrane that was immersed in 70% ethanol solution during 5 min. The perfusion cell, the feed tank, the metallic/silicone tubing and the connections were sterilized using autoclave for 30 minutes at 120°C.

Figure 5.2a presents the  $\text{O}_2$  sensor that was assembled in the perfusion cell. The  $\text{O}_2$  sensor was a contactless sensing system that measures the oxygen concentration in liquid medium. The device consisted of an optical reader (Figure 5.2b) and a sensing spot (Figure 5.2c).

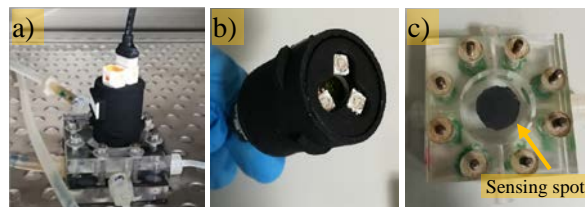


**Figure 5.2.** a)  $\text{O}_2$  sensor used assemble in the perfusion cell, including b) the optical reader and c) the sensing spot placed on the inner side of the cover of the perfusion cell.

On the one hand, the sensing spot had a fluorescent substance that, after being excited by the optical reader, emitted light with different wavelengths. Depending on the oxygen concentration in the perfusion cell, the intensity and time delay of the emitted light varied. On the other hand, the optical reader contained LEDs that generated the exciting light and sensors to capture the emitted fluorescent light related to the oxygen concentration in the medium. It was also connected to a computer used for reading the measurements through the BlueBlink software.

Before performing the experiment, the O<sub>2</sub> sensor was set up. First, the sensing spot was stuck to the inner surface of the perfusion cell cover, in contact with the liquid permeate. The device was then calibrated under the incubator conditions (temperature 37°C, atmospheric pressure and humidity 95%) following supplier instructions: a two-point calibration procedure was applied, operating at 100% air-saturated and 0% air-saturated conditions. For the calibration at 100% air-saturated conditions, distilled water was continuously sparged with air, while the calibration at 0% air conditions was performed using an aqueous sodium dithionite solution (Na<sub>2</sub>SO<sub>3</sub>, 2.5 g·L<sup>-1</sup>) to remove any O<sub>2</sub>, according to the following reaction:  $2 \text{Na}_2\text{SO}_3 + \text{O}_2 \rightarrow 2 \text{Na}_2\text{SO}_4$ .

### 5.2.2. Dynamic cell culture

U87 human glioblastoma cells (ATCC® HTB-14™) were employed to carry out cell proliferation tests under dynamic conditions. The culture medium was composed of Dulbecco's Modified Eagle Medium (DMEM) with 10% of Fetal Bovine Serum (FBS), antibiotic agents (penicillin G (100 U·mL<sup>-1</sup>) and streptomycin (100 mg·mL<sup>-1</sup>) (Appendix I). Cell expansion was obtained using the same protocol previously explained in *Chapter 2*.

Cells were seeded on the surface of the sterile membrane at a density of  $3 \times 10^4$  cells/cm<sup>2</sup>. The perfusion cell contained the membrane with cells. It was kept closed in the incubator during 3 hours to favor cell adhesion. After that, the perfusion cell was connected to the dynamic fluid system. Initially, the volume of culture medium was 115 mL, which was not replaced during the experiment. Cell cultures proceeded during 3 days under dynamic conditions. Simultaneously, cell culture experiments

under static conditions (cell density of  $3 \times 10^4$  cells/cm<sup>2</sup>) for 3 days were also performed as control assay. In this case, the perfusion module was not connected to the perfusion system. Instead, the perfusion cell was filled with culture medium, which was not replaced during the experiment. Both in static and dynamic conditions, the perfusion bioreactor integrated a 0.45  $\mu\text{m}$  syringe filter to allow the air exchange between the perfusion system and the incubator.

Confocal microscopy images of inverted membrane samples were captured after 3 hours in order to analyze the cell adhesion, and later, after 3 days to evaluate the cell proliferation. The procedure previously explained in *Chapter 2* was applied.

The influence of mechanical stimuli on cell cultures under dynamic conditions was evaluated through the calculation of shear stress over the cells. According to Wang et al. [13], the shear stress  $\tau$  (Pa) was expressed as (Equation 5.1):

$$\tau = \sqrt{\mu \cdot J_v \cdot \Delta P / \delta} \quad (5.1)$$

where  $\mu$  is the viscosity of the culture medium ( $9.4 \times 10^{-4}$  Pa·s [14]),  $\delta$  is the thickness of the membrane (97  $\mu\text{m}$ ) and  $\Delta P$  (Pa) is the transmembrane pressure drop. The permeate flux,  $J_v$  (L·m<sup>-2</sup>·h<sup>-1</sup>) was calculated, according to the Equation 5.2:

$$J_v = \frac{V_{\text{permeate}}}{\Delta t \cdot A_e} \quad (5.2)$$

where  $V_{\text{permeate}}$  is the volume of permeate collected along the interval  $\Delta t$  (h).

### 5.2.3. Nutrient flux characterization

The flux of the culture medium across the membrane under dynamic culture conditions was evaluated for three days (*Cult. m. cells*). The experimental system was operated inside an incubator at 37°C and constant CO<sub>2</sub> concentration of 5%. The transmembrane pressure was maintained in the range 7 - 25 mbar, and the tangential feed flowrate of the culture medium was fixed at 1 mL·min<sup>-1</sup> [15,16].

Blank experiments without cells were carried out to set up the perfusion bioreactor. The obtained results were used as background control for the *Cult. m. cells* experiment. The experiments were preferentially conducted for three days. However, the gaseous atmosphere of the incubator was not controlled. Two different solutions were tested: the model medium (*Model m.*) and the culture medium (*Cult. m.*). The model medium consisted of a solution composed of 0.4 g·L<sup>-1</sup> of bovine serum albumin (BSA) and 1 g·L<sup>-1</sup> of glucose in phosphate buffer solution (PBS) at pH 7.4.

The concentration of proteins was analyzed in both permeate and feed solutions by UV-vis spectroscopy (UV-1800 Shimadzu) at a wavelength of 280 nm. The transmission of the proteins was calculated, using the following equation (5.3):

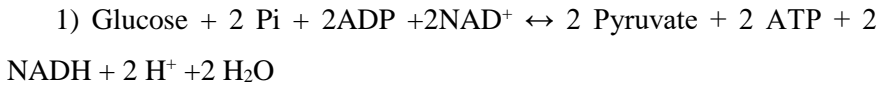
$$\text{Protein Transmission (\%)} = \frac{C_p}{C_f} \cdot 100 \quad (5.3)$$

where  $C_p$  and  $C_f$  are the concentrations of the proteins in the permeate stream and feed stream, respectively.

The concentration of glucose was measured using the Glucose GOD-

PAP lab kit (Biolabo SAS) as aforementioned in *Chapter 2*.

The lactate concentration in the culture medium depended on the glucose consumption through the cell feeding. The following reactions explained the glucose conversion into lactate [17,18]:



*Pi* refers to several orthophosphates including glucose-6-phosphate, fructose-6-phosphate and fructose 1,6-biphosphate among others. *ADP* refers to adenosine diphosphate, *ATP* is related to adenosine triphosphate and *NAD* and *NADH* are associated with nicotinamide adenine dinucleotide and its reduced form, respectively. First, the metabolic process called glycolysis consisted in a sequence of reactions that metabolizes one molecule of glucose into two molecules of pyruvate with the concomitant net production of two molecules of ATP. Then, the pyruvate was processed to lactate by the enzyme lactate dehydrogenase [17].

The lactate concentration ( $C_L$ ) was quantified using the lactate reagent set lab kit (L7596, Pointe Scientific). The sample was prepared following the protocol as indicated by the provider, through a combination of two reagents. Reagent 1 was made of tris(hydroxymethyl) aminomethane (TRIS) buffer 100 mM, 4-aminoantipyrene 1.7mM, peroxidase 10000 U·L<sup>-1</sup> and preservatives, while reagent 2 was constituted of TRIS buffer 100 mM, lactate oxidase 1000 U·L<sup>-1</sup>, N-Ethyl-N-(2-hydroxy-3-sulfopropyl)-3-methylaniline, sodium salt, hydrate (TOOS) 1.5mM and preservatives. The UV-vis light absorbance (ABS) of the sample was

measured at 546 nm. Equation 5.4 was employed to calculate the lactate concentration:

$$C_L (g \cdot L^{-1}) = \frac{ABS \text{ sample}}{ABS \text{ standard}} \cdot [C_{L,st}] \quad (5.4)$$

where the standard (2327 L-lactate standard, YSI) was composed of L-lactate ( $C_{L,st} = 0.45 \text{ g} \cdot \text{L}^{-1}$ ).

The oxygen concentration of the permeate stream in the liquid phase that feeds the cells was monitored periodically. The oxygen concentration was also measured using culture medium in the absence of cells as control assay.

Most of the experiments were tested in duplicate, except the experiment working with the culture medium without cells, which was not replicated.

### 5.3. Results and discussion

#### 5.3.1. Nutrient flux characterization

Figure 5.3 compares the permeate flux across the PCL/rGO membrane in experiments using the perfusion membrane bioreactor. Overall, the permeate flux decreased during the experiment in all cases. This behavior, which was previously observed during the mass transfer characterization of PCL/rGO membranes (*Chapter 2*), is associated with the membrane pores narrowing due to internal protein fouling. Although the initial permeate flux of the culture medium was higher than the flux obtained by the model medium, both types of solutions converged on similar permeate fluxes at steady state. Moreover, no significant

differences were observed when cells were cultured on the membranes, probably because cells were only partially covering the membrane surface during the short time of experiments conducted.

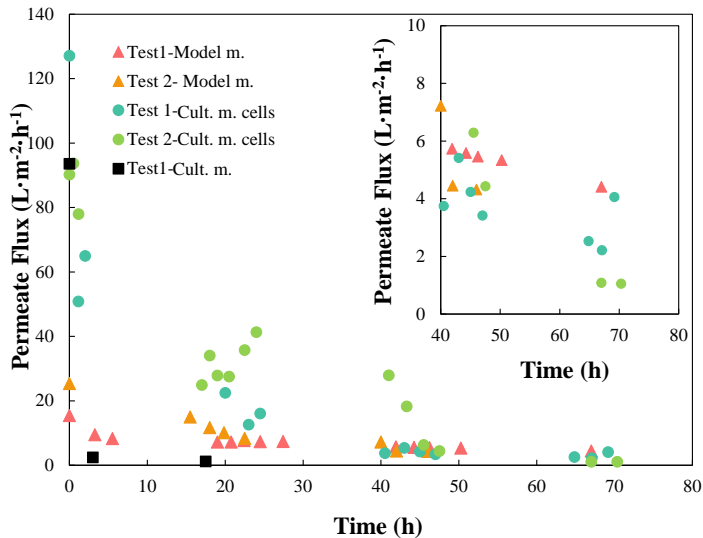


**Figure 5.3.** Evolution of the permeate flux across the PCL/rGO membrane using the model medium (BSA+Glucose in PBS), culture medium (DMEM+FBS) and culture medium with cells (DMEM+FBS). All experiments were performed in the perfusion bioreactor described in section 5.2.1

The nutrient permeance through PCL/rGO membranes in tangential flow configuration using a model medium ( $0.4 \text{ g}\cdot\text{L}^{-1}$  of BSA in PBS at  $37^\circ\text{C}$  and transmembrane pressure of  $0.05\text{-}0.2 \text{ bar}$ , 4 h of experiment) was  $4140 \text{ L}\cdot\text{m}^{-2}\cdot\text{h}^{-1}\cdot\text{bar}^{-1}$  at steady state (*Chapter 2*). Assuming a linear dependency between permeate flux and transmembrane pressure (Eq. 2.10, *Chapter 2*), the calculated flux of the model solution through the membrane at a transmembrane pressure of  $7\text{-}25 \text{ mbar}$  would vary in the range  $29\text{-}103 \text{ L}\cdot\text{m}^{-2}\cdot\text{h}^{-1}$ . This value was 4 - 15 times higher than the permeate flux of the model medium after 4 hours in the perfusion bioreactor ( $6.7 \pm 2.4 \text{ L}\cdot\text{m}^{-2}\cdot\text{h}^{-1}$ ), indicating that the differences in the

hydrodynamics conditions achieved in the perfusion bioreactor and membrane test cell were influencing the transmembrane flux. In light of those results, it was demonstrated that the permeate fluxes obtained from both procedures experienced the same changes during the test, which was associated with the pore narrowing of the membrane by internal fouling.

Figure 5.4 presents the protein transmission across the PCL/rGO membrane in experiments using the perfusion membrane bioreactor. The protein transmission in the model medium decreased from  $92 \pm 1\%$  to  $61 \pm 10\%$  after 3 days. In contrast, the protein transmission was almost constant in the experiments using the culture medium and cell cultures from  $98 \pm 5\%$  to  $96 \pm 0.003\%$  under dynamic conditions.

Regarding the static cultures, protein concentration was maintained constant during the 3 days experiment, both in the cell and feed compartments.

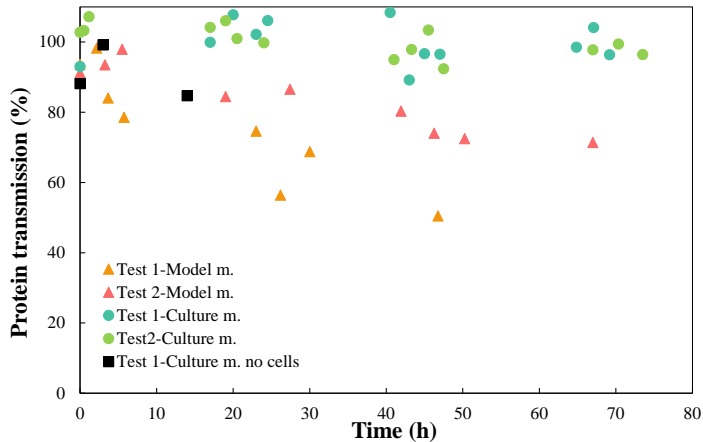


**Figure 5.4.** Evolution of the protein transmission across the PCL/rGO membrane using the model medium (BSA+Glucose in PBS), culture medium (DMEM+FBS) and culture medium with cells (DMEM+FBS). All experiments were performed in the perfusion bioreactor described in section 5.2.1.

Scarce literature has been found dealing with any possible cell-mediated change of protein transmission during filtration through porous membranes. A possible explanation of the higher protein transmission in systems with cells could be that cells could form an additional dynamic membrane at the top of the microporous polymeric membrane that retains some protein aggregates. In consequence, the protein transmission would enhance in comparison with the single protein solution filtration, which progressively would block and/or constrict the pore entrances [19]. This type of effect was reported by Güell et al. [19], who studied the influence of the presence of yeast cells on cellulose acetate membrane fouling by a protein mixture. Notwithstanding, due to the differences between the experimental bioreactor configurations in that work and in the present study, further analysis would be needed to ascertain a plausible mechanism for our observations.

Figure 5.5 shows glucose evolution in the feed and permeate streams in the experiments using culture medium with cells.

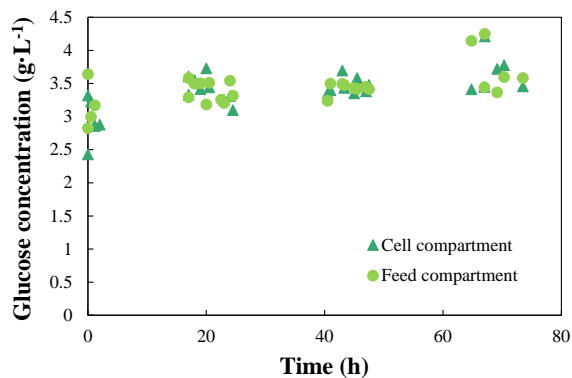


**Figure 5.5.** Glucose concentration of the culture medium (DMEM+FBS) with cells in cell and feed compartments during 3 days of experiment.

Results showed that there was not clear evidence of glucose rejection by the membrane as it was expected [20], neither glucose cell consumption because nutrients were in excess.

The lactate concentration in dynamic experiments was below the detection limit. Therefore, under the present cell density and experimental conditions and duration, nutrients supply limitation did not occur. On the contrary, in static experiments lactate concentration ( $0.1 \text{ g}\cdot\text{L}^{-1}$ ) was equilibrated in cell and feed compartments after 3 days of experiment, indicating, that certain cell metabolism occurred. However, the glucose concentration remained constant at initial and final experimental times and in both perfusion cell compartments, which was attributed to the analytical error.

Oxygen is an important parameter because it is often the limiting nutrient inside high thickness *in vitro* tissues, due to the low solubility of oxygen in aqueous media [15]. Figure 5.6 shows the oxygen concentration that was observed in the culture medium in experiments under dynamic conditions and also in the absence of cells.

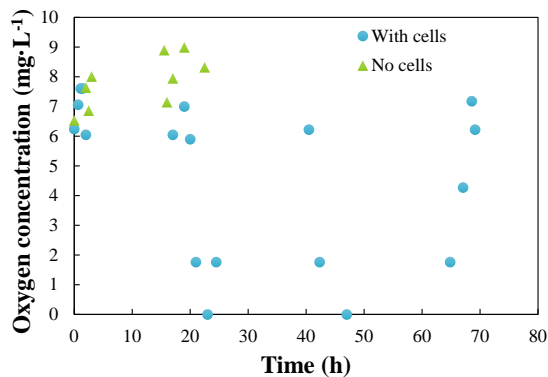


**Figure 5.6.** Oxygen concentration in the culture medium measured at the top of the perfusion cell with and without dynamic cell culture.

The oxygen concentration of the medium without cells was maintained in the range of 6.53-8.32 mg·L<sup>-1</sup>, similar to values of dissolved oxygen in saturated culture medium [21]. On the contrary, the oxygen concentration under dynamic cell cultures formed up-down cycles of oxygen concentration. First the oxygen concentration was established around 6.83 mg·L<sup>-1</sup>. Next, it decreased down to 1.76 and 0 mg·L<sup>-1</sup>. After that, the oxygen concentration increased again. Then, oxygen concentration presented a cyclic behavior, with repetitive ups and downs.

The membrane was expected to provide a suitable oxygenation platform, due to the high porosity of the membrane [22] and also because the cell compartment was open to the incubator atmosphere. Results suggested that the oxygen concentration supply would not be limited. The oxygen concentration cycles could not be clearly related to any cell metabolic consumption, and meanwhile they might be attributed to some artifact of the measuring device or to the bioreactor design, which should be carefully reviewed.

### **5.3.2. Effect on cell behavior in static and dynamic conditions**

Figure 5.7 presents confocal microscopic images of U87 glioblastoma cells cultured on the PCL/rGO membranes, under static or dynamic conditions. Images showed that the number of cells significantly increased after 3 days culture, in both static and dynamic conditions, in comparison to the initial adhesion stage (3 hours). On the one hand, cells cultured under static conditions formed clusters and agglomerated. On the other hand, cells that were cultured under dynamic conditions showed cytoplasmatic expansion and broader and more uniform distribution on

the membrane. In fact, the average cell diameter was  $15\ \mu\text{m}$  in dynamic culture in the perfusion bioreactor, significantly higher than  $7\ \mu\text{m}$  cell diameter obtained in static culture conditions.

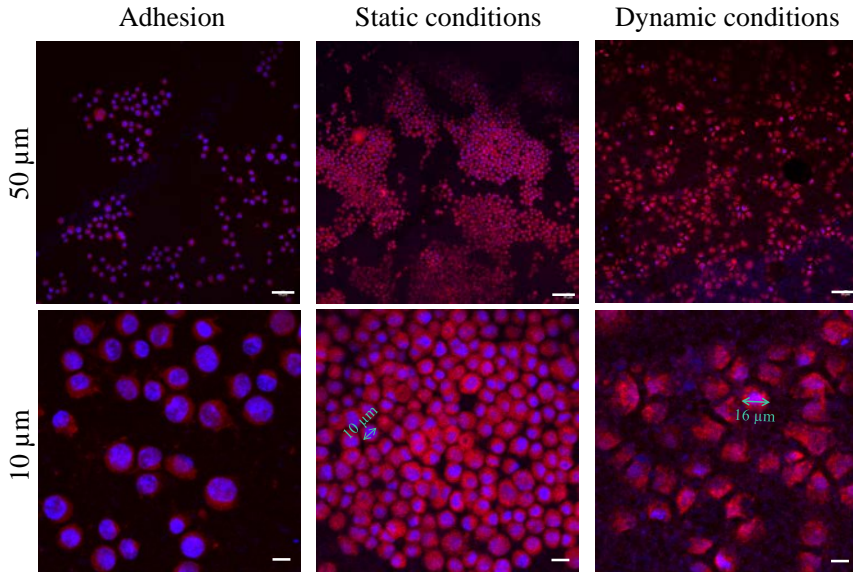


**Figure 5.7.** Confocal images of U87 glioblastoma cells cultured on the PCL/rGO membranes and analyzed at 3 hours after seeding (adhesion) and after 3 days under static or dynamic conditions. Scale bars represent  $50\ \mu\text{m}$  and  $10\ \mu\text{m}$ .

In agreement with our results, several works have reported low uniformity of cells cultured under static conditions compared to dynamic conditions [3,23]. For example, Jaasma et al. [3] observed improved osteoblast cell homogeneity along the collagen–glycosaminoglycan scaffold inside the flow perfusion bioreactor.

Results demonstrated that the intrinsic mechanical stimuli produced by the perfusion bioreactor involved an improvement in the cell distribution and growth. Therefore, the shear stress over the cells in the perfusion bioreactor was calculated from flux data (Equation 5.1). Figure

5.8 shows that the shear stress was steadily decreasing from  $477 \pm 95$  mPa to  $86 \pm 3$  mPa, in agreement with the reduction of the permeate flux along the experiment (Figure 5.3).

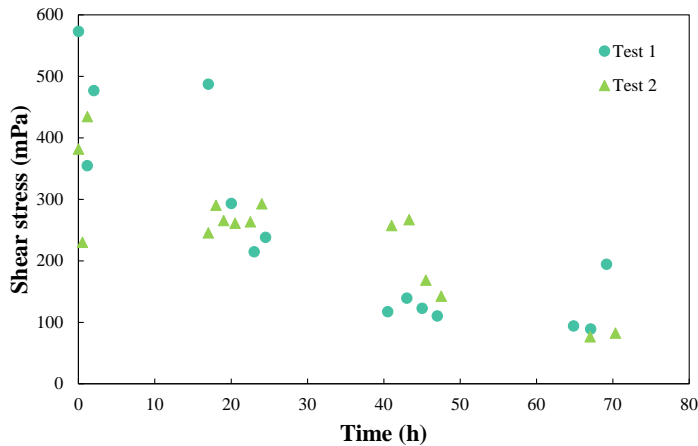


**Figure 5.8.** Shear stress over the cells in the perfusion PCL/rGO membrane bioreactor during a 3 days cell culture experiment.

In comparison to previous works that studied cell cultures using similar systems under dynamic conditions, our calculated shear stress was very low [15,24,25]. We selected conditions of low feed flow rate and low transmembrane pressure to avoid deflection of the membrane, because the polymer material showed marked elastic properties. Transmembrane pressures above  $\sim 50$  mbar could curve membranes until completely touching the cover of the perfusion cell. Moreover, cell exposure to high shear stress could result in cell detachment, damage or death [9,24,26,27]. For instance, Bettahalli et al. [24] used a shear stress of 4270 mPa over muscle cells cultured in a hollow fiber membrane bioreactor that resulted in very few cells on the fiber surface after 7 days.

For neural regeneration, it was reported that low values of shear stress affected positively cellular responses, including adhesion, proliferation,

alignment and differentiation [9,27]. For example, Jeon et al. [27] studied the shear stress effect on cell cultures using a non-perfused system. They used micro-patterned substrates seeded with human MSCs in a parallel-plate flow chamber to induce shear stress. They observed that low shear stresses (100 mPa) promoted higher neuronal response of human MSCs than without shear stress. Therefore, results showed that mechanical stimuli benefited the cell response, regardless the system used.

#### **5.4. Final remarks**

Glioblastoma cells were cultured on PCL/rGO membranes under dynamic conditions to evaluate the aptitude of the mechanical stimuli produced by the perfusion membrane bioreactor to elicit an enhancement of the cell behavior. Due to the influence of the mechanical stimuli that promoted the suitable cell growth and behavior, results presented better cell distribution and growth under dynamic conditions with respect to the static cultures.

Nevertheless, in this study there are certain limitations that should be taken into account for future works:

- Some design deficiencies of the perfusion cell have been detected, producing overpressures inside the perfusion bioreactor that could have caused fluid-dynamic pressure drops and/or local overpressures.
- The experimental conditions used in this study implied working at excess of nutrient supply. For future research, the experimental conditions should be adjusted to evaluate the potential improvement of dynamic cultures compared to static cultures,

regarding the limitation of the nutrient supply.

- Additional experiments under different transmembrane pressures should be studied to optimize the cell culture growth, considering the mechanical properties of the PCL/rGO membrane (high deformation at low transmembrane pressures).
- Further study on the oxygen evolution should be carried out to ascertain the cause of the observed cycle behavior. Besides, a parallel O<sub>2</sub> monitoring in static and dynamic culture experiments is recommended.

In conclusion, the proof of concept conducted in this study confirmed the important effect of the mechanical stimulation on cell cultures. Therefore, the mechanical cues combined with the intrinsic benefits of the membrane composite material to elicit neural differentiation might improve substantially the potential of a PCL/rGO membrane perfused system to produce reliable *in vitro* neural models. However, the obtained results indicated that the perfusion membrane bioreactor design and/or the polymer membrane material used in this work should be revised.

## 5.5. References

- [1] J. Hansmann, F. Groeber, A. Kahlig, C. Kleinhans, H. Walles, *Biotechnol. J.* **2013**, 8, 298.
- [2] T. D. Brown, *J. Biomech.* **2000**, 33, 3.
- [3] M. J. Jaasma, F. J. O'Brien, *Tissue Eng. Part A* **2008**, 14, 1213.
- [4] O. Akhavan, *J. Mater. Chem. B* **2016**, 4, 3169.
- [5] H. Stoll, I. K. Kwon, J. Y. Lim, *Neural Regen. Res.* **2014**, 9, 1810.
- [6] D. Becker, D. S. Gary, E. S. Rosenzweig, W. M. Grill, J. W. McDonald, *Exp. Neurol.* **2010**, 222, 211.
- [7] H. Tsuji, A. Mizuno, Y. Ikada, *J. Appl. Polym. Sci.* **2000**, 77, 1452.

- [8] F. Yang, R. Murugan, S. Wang, S. Ramakrishna, *Biomaterials* **2005**, *26*, 2603.
- [9] I. A. Kim, S. a Park, Y. J. Kim, S.-H. Kim, H. J. Shin, Y. J. Lee, S. G. Kang, J.-W. Shin, *J. Biosci. Bioeng.* **2006**, *101*, 120.
- [10] S. Morelli, S. Salerno, A. Piscioneri, B. J. Papenburg, A. Di Vito, G. Giusi, M. Canonaco, D. Stamatialis, E. Drioli, L. De Bartolo, *Biomaterials* **2010**, *31*, 7000.
- [11] D. Chafik, D. Bear, P. Bui, A. Patel, N. F. Jones, B. T. Kim, C. T. Hung, R. Gupta, *Tissue Eng.* **2003**, *9*, 233.
- [12] M. C. Laplaca, V. M.-Y. Lee, L. E. Thibault, *J. Neurotrauma* **1997**, *14*, 355.
- [13] S. Wang, J. M. Tarbell, *Arter. Thromb Vasc Biol* **2000**, *20*, 2220.
- [14] E. Fröhlich, G. Bonstingl, A. Höfler, C. Meindl, G. Leitinger, T. R. Pieber, E. Roblegg, *Toxicol. Vitro.* **2013**, *27*, 409.
- [15] S. Morelli, S. Salerno, A. Piscioneri, F. Tasselli, E. Drioli, L. De Bartolo, *Chem. Eng. J.* **2016**, *305*, 69.
- [16] D. A. Gaspar, V. Gomide, F. J. Monteiro, *Biomatter* **2012**, *2*, 167.
- [17] J. Berg, J. Tymoczko, L. Stryer, *Biochemistry* **2002**, 319.
- [18] M. J. Rogatzki, B. S. Ferguson, M. L. Goodwin, L. B. Gladden, *Front. Neurosci.* **2015**, *9*, 1.
- [19] C. Güell, P. Czekaj, R. H. Davis, *J. Memb. Sci.* **1999**, *155*, 113.
- [20] E. Curcio, L. De Bartolo, G. Barbieri, M. Rende, L. Giorno, S. Morelli, E. Drioli, *J. Biotechnol.* **2005**, *117*, 309.
- [21] R. J. McMurtrey, *Tissue Eng. Part C Methods* **2016**, *22*, 221.
- [22] M. Loeblein, G. Perry, S. H. Tsang, W. Xiao, D. Collard, P. Coquet, Y. Sakai, E. H. T. Teo, *Adv. Healthc. Mater.* **2016**, *5*, 1177.
- [23] C. Kleinhans, R. R. Mohan, G. Vacun, T. Schwarz, B. Haller, Y. Sun, A. Kahlig, P. Kluger, A. Finne-Wistrand, H. Walles, J. Hansmann, *Biotechnol. J.* **2015**, *10*, 1727.
- [24] N. M. S. Bettahalli, J. Vicente, L. Moroni, G. A. Higuera, C. A. Van Blitterswijk, M. Wessling, D. F. Stamatialis, *Acta Biomater.* **2011**, *7*, 3312.
- [25] S. Morelli, A. Piscioneri, S. Salerno, C. C. Chen, C. H. Chew, L. Giorno, E. Drioli, L. De Bartolo, *Biofabrication* **2017**, *9*, 025018.
- [26] M. Liu, W. Song, P. Li, Y. Huang, X. Gong, G. Zhou, X. Jia, L. Zheng, Y. Fan, *PLoS One* **2013**, *8*, 2.
- [27] K. J. Jeon, S. H. Park, J. W. Shin, Y. G. Kang, J. S. Hyun, M. J. Oh, S. Y. Kim, J. W. Shin, *J. Biosci. Bioeng.* **2014**, *117*, 242.



# *Chapter 6*

**Conclusions and challenges for future research**



## 6.1. Conclusions

This thesis was focused on the development and characterization of a proof of concept for an *in vitro* neural model based on a porous polymer membrane functionalized with graphene based nanomaterials to modulate reproducible neural differentiation.

The main conclusions of this work are summarized below:

- ***Regarding the membrane fabrication and characterization:***

PCL/GbN porous flat membranes were developed to act as cell supports. Membranes were fabricated under mild-temperature conditions and nontoxic reductive reagents using non-solvent induced phase separation technique. The GbNs used were GO and rGO, producing PCL/GO and PCL/rGO membranes. Also, the PCL/GO membranes were exposed to a post-treatment using a UV lamp to reduce the GO embedded in the membranes (PCL/GO/UV). Different concentrations of the nanomaterial into the polymeric matrix were tested. **The selected concentration to obtain an optimal membrane to be used in bioreactors for neural tissue regeneration was 0.1 w/w%.**

The possible composite formation between PCL and GO was evaluated through thermal, mechanical and spectroscopic analysis. Due to the low GO concentration used in the membranes, the formation of covalent bonds between the materials was not conclusive.

The ability of the membranes to act as cell supports was analyzed through morphological, mechanical, water and nutrient filtration, electrical conductivity, hydrophilicity and biocompatibility tests.

**PCL/rGO membranes presented the most promising properties to act as cell supports** in comparison with the other fabricated membranes.

Subsequently, the PCL/rGO membrane was selected to study its hydrolytic degradation, simulating *in vitro* conditions during 12 months, in order to elucidate their applicability as scaffolds in *in vitro* perfusion bioreactors. Results showed higher degradation rate of our PCL/rGO membranes compared to plain PCL networks under similar hydrolytic degradation conditions. This behavior was assigned to the higher porosity of PCL/rGO membranes. During the hydrolytic degradation, the membranes experienced several changes: the reduction of the molecular weight, the increase of the crystallinity fraction, the erosion of the internal structure and the formation of polymer degradation products. Overall, the mechanical resistance was severely reduced. These results demonstrated that the high internal porosity of the membranes facilitated water penetration, thus promoting an accelerated hydrolytic degradation via bulk degradation mechanism. On the contrary, the rGO nanoplatelets remained immobilized inside the membrane during the hydrolytic degradation process. Moreover, the moderately slow formation and release of degradation by-products to the culture medium would not affect negatively the development of cell cultures. **Despite their accelerated degradation, the PCL/rGO membranes were considered suitable to develop *in vitro* neural tissues**, as the *in vitro* neural tissue takes approximately one month to be completed.

- *Considering the influence of GbNs and mechanical stimuli over cell cultures:*

The influence of the chemical state (oxidize or reduced) of GbNs, GO and rGO, and their distribution in the membrane matrix over neural differentiation and maturation was characterized using human neural progenitor cells (hNPCs) under static conditions, which derived from human induced pluripotent stem cells.

Raman spectroscopy analysis demonstrated that GO was deposited on the membrane surface, while rGO was placed inside the membrane. The location of GO allowed the direct contact between the GO nanomaterials and the cells. In consequence, a higher number of electrically active cells was found compared to tissue culture plate (TCP) and to PCL/rGO membrane. Although rGO was embedded in the membrane, the hNPCs differentiation and the magnitude of neural activity spikes during maturation were significantly better in PCL/rGO than in TCP and PCL/GO, attributed to the higher conductivity of the nanomaterial. Therefore, results showed that **the presence of GbNs in the membrane matrix promoted hNPC differentiation and maturation, and that the rGO nanomaterial exhibited the best potential.**

Moreover, cell cultures under dynamic conditions were developed to evaluate the influence of mechanical stimuli on neural cell cultures. Hence, a home-made perfusion PCL/rGO membrane bioreactor was designed and used to generate mechanical stimuli in the form of fluid-induced shear stress. In comparison to static cell cultures, **the mechanical stimuli produced by the bioreactor resulted in an efficient cell distribution on the membrane, as well as a better neural cell growth.**

In conclusion, **the combination of PCL/rGO porous flat membranes with the mechanical stimuli produced by the perfusion membrane bioreactor demonstrated promising properties to develop an *in vitro* neural model with improved reproducible differentiation.**

## **6.2. Challenges for future research**

Based on the results obtained from this PhD thesis, the conduction of the following proposals are suggested for future research:

- Evaluation of PCL/GbNs membranes with improved nanomaterial quality. The graphene produced by chemical vapor deposition would improve the electrical conductivity and hence, the neural cell response.
- Fabrication and characterization of PCL/rGO membranes in hollow fiber configuration. The hollow fibers acting as a vascular system would enhance the nutrient transport favoring the formation and internal nourishment of 3D neural tissues.
- Design of an optimal perfusion hollow fiber bioreactor, including the optimization of the operational variables and the incorporation of electrical stimulation to differentiate stem cells into neural tissues.
- Development of a mathematical model that describes the *in vitro* cell culture behavior under dynamic conditions, the variation of nutrients and the external stimuli that can cause cellular stress. This modeling technique would help to achieve the optimal operating conditions for perfusion bioreactor designs. Moreover, it could estimate the cell consumption parameters for future experimental testing.

### 6.3. Conclusiones

Esta tesis se centra en el desarrollo y caracterización de una prueba de concepto para un modelo neuronal *in vitro* a partir de una membrana polimérica porosa funcionalizada con nanomateriales basados en grafeno para mejorar la reproducibilidad de diferenciación neuronal.

Las principales conclusiones de este trabajo se resumen a continuación:

- ***Respecto a la fabricación y caracterización de membranas:***

Se desarrollaron membranas porosas planas de PCL/GbN para actuar como soportes celulares. Las membranas se fabricaron mediante la técnica de separación de fases inducida por un no solvente en condiciones de temperaturas suaves y sin utilizar agentes tóxicos de reducción. Los GbN utilizados fueron GO y rGO, dando lugar a las membranas de PCL/GO y PCL/rGO. Además, las membranas de PCL/GO fueron expuestas a un post-tratamiento de luz UV para reducir el GO embebido en la membrana (PCL/GO/UV). Se probaron distintas concentraciones del nanomaterial en la matriz polimérica, siendo **la concentración de 0.1 w/w% la seleccionada para la obtención de una membrana óptima para ser usada en biorreactores para regeneración de tejido neuronal.**

La posible formación de materiales compuestos de PCL y GO se evaluó a partir de análisis térmicos, mecánicos y de espectroscopía. Debido a la baja concentración de GO utilizada en las membranas, la formación de enlaces covalentes entre los materiales no fue concluyente.

La capacidad de las membranas para actuar como soportes celulares se evaluó a través de análisis morfológicos, mecánicos, de filtración de agua y nutrientes, de conductividad eléctrica, de hidrofiliidad y de biocompatibilidad. **Las membranas de PCL/rGO presentaron las mejores características para actuar como soportes celulares**, en comparación con las demás membranas fabricadas.

Posteriormente, las membranas de PCL/rGO se seleccionaron con el fin de estudiar su degradación hidrolítica, simulando condiciones *in vitro* durante 12 meses, para esclarecer su aplicación como soportes en biorreactores de perfusión en condiciones *in vitro*. Los resultados mostraron una tasa de degradación mucho mayor en nuestras membranas en comparación con sistemas de PCL en condiciones de degradación hidrolítica similares, relacionado con la alta porosidad de nuestras membranas. Durante la degradación hidrolítica, las membranas experimentaron varios cambios: la reducción en el peso molecular, la mejora de la fracción cristalina, la erosión de estructura interna y la formación de productos de degradación. Estos resultados demostraron que la alta porosidad interna de las membranas facilitó la penetración del agua, promoviendo así una degradación hidrolítica acelerada a través del mecanismo de degradación *bulk*. Por otro lado, el rGO se mantuvo inmovilizado dentro de la membrana durante el proceso de degradación hidrolítica. Además, se considera que la formación y liberación lenta de los subproductos de degradación al medio de cultivo no afectaría negativamente al desarrollo de cultivos celulares. **A pesar de la degradación acelerada, las membranas de PCL/rGO se consideraron adecuadas para desarrollar tejidos neuronales *in vitro***, ya que el tejido neuronal *in vitro* tarda aproximadamente un mes en formarse.

- *Considerando la influencia de los GbNs y estímulos mecánicos sobre los cultivos celulares:*

La influencia del estado químico (oxidado o reducido) de los GbNs, GO y rGO, y su distribución en la matriz de membrana sobre la diferenciación y maduración neuronal fue caracterizado usando células humanas progenitoras neuronales (hNPCs) en condiciones estáticas, las cuales derivan de células madre pluripotentes inducidas de origen humano.

A partir del análisis de espectroscopia Raman, se demostró que el GO se encontraba en la superficie de la membrana, mientras que el rGO estaba dentro de la membrana. La ubicación del GO permitió un contacto directo entre los nanomateriales de GO y las células. Como consecuencia, se observó un mayor número de células con estímulos eléctricos comparado con la placa de cultivos tradicional (TCP) y con la membrana de PCL/rGO. Aunque el rGO se localizó dentro de la membrana, la diferenciación de hNPCs y la magnitud de los picos de actividad de las neuronas durante la maduración fueron significativamente mayores que con el TCP y la membrana de PCL/GO, atribuyéndose este comportamiento a una mayor conductividad del nanomaterial. Por tanto, **la presencia de GbNs en la matriz de la membrana fomentó la diferenciación y maduración de las hNPCs, siendo el nanomaterial de rGO el que mostró el mejor potencial.**

Además, se desarrollaron cultivos celulares en dinámico para evaluar la influencia de los estímulos mecánicos en cultivos de células neuronales. Para ello, se diseñó y utilizó un biorreactor de perfusión con membranas de PCL/rGO para generar estímulos mecánicos en forma de

esfuerzo cortante inducido por el fluido. En comparación con los cultivos en estático, los estímulos mecánicos producidos por el biorreactor causaron una **distribución celular eficiente sobre la membrana, así como un crecimiento celular mejorado.**

Como conclusión, **la combinación de membranas planas y porosas de PCL/rGO junto con los estímulos mecánicos producidos por el biorreactor de perfusión de membrana demostraron unas propiedades prometedoras para desarrollar un modelo neuronal *in vitro* con una reproducibilidad de diferenciación mejorada.**

#### **6.4. Retos para futuras investigaciones**

En relación a los resultados de la presente tesis doctoral, se plantean las siguientes propuestas para futuras investigaciones:

- Evaluación de membranas de PCL/GbNs con una calidad del nanomaterial mejorada. El grafeno producido por deposición química de vapor podría mejorar la conductividad eléctrica y, por tanto, la respuesta de las células neuronales.
- Fabricación y caracterización de membranas de PCL/rGO en configuración de fibra hueca. Las fibras huecas que actúan como un sistema vascular mejorarían el transporte de nutrientes favoreciendo la formación y nutrición interna de los tejidos formados.
- Diseño de un biorreactor de perfusión de fibras huecas optimizado, incluyendo la optimización de las variables de operación e incorporación de estímulos eléctricos para la diferenciación específica de células madre en tejido neuronal.

- Desarrollo de un modelo matemático que describa el comportamiento de cultivos celulares *in vitro* en condiciones dinámicas, la variación de nutrientes y las fuerzas externas que pueden causar estrés celular. La técnica de modelado ayudaría a lograr las condiciones óptimas de operación para los diseños de biorreactores de perfusión. Además, se podría estimar los parámetros de consumo celular para futuras pruebas experimentales.



# *Appendix*



## Appendix I. Composition of the culture medium

The culture medium was composed DMEM supplemented with 10% fetal bovine serum (FBS), antibiotic agents (penicillin G (100 U·mL<sup>-1</sup>) and streptomycin (100 mg·mL<sup>-1</sup>). Table 1 describes the DMEM composition while Table 2 presents the composition of FBS.

**Table 1.** Technical documentation of DMEM obtained from *Hyclone*.

	Description	mg·L <sup>-1</sup>
Inorganic salts	CaCl <sub>2</sub> (anhydrous)	200.00
	Fe(NO <sub>3</sub> )·9H <sub>2</sub> O	0.10
	KCl	400.00
	MgSO <sub>4</sub>	97.67
	NaCl (anhydrous)	6400.00
	NaH <sub>2</sub> PO <sub>4</sub> ·H <sub>2</sub> O	125.00
Amino Acids	L-Arginine HCl	84.00
	L-Cystine 2HCl	62.57
	L-Glutamine	584.00
	Glycine	30.00
	L-Histidine HCl·H <sub>2</sub> O	42.00
	L-Isoleucine	104.80
	L-Leucine	104.80
	L-Lysine HCl	146.20
	L-Methionine	30.00
	L-Phenylalanine	66.00
	L-Serine	42.00
	L-Threonine	95.20
	L-Tryptophan	16.00
	L-Tyrosine 2Na·2H <sub>2</sub> O	103.79
L-Valine	93.60	
Vitamins	D-Ca Pantothenate	4.00
	Choline Chloride	4.00
	Folic Acid	4.00
	Myo-Inositol	7.00
	Niacinamide	4.00
	Pyridoxal HCl	4.00
	Riboflavin	0.40
	Thiamine HCl	4.00
Others	D-Glucose	4500.00
	Phenol Red (Sodium)	15.90
	NaHCO <sub>3</sub>	3700.00

**Table 2.** Technical documentation of approximately final concentration of FBS used in the culture medium. Results were calculated from X. Zheng, H. Baker, W. S. Hancock, F.

Fawaz, M. McCaman, E. Pungor, *Biotechnol. Prog.* 2006, 22, 1294.

<b>Abundant proteins in FBS</b>	<b>mg·L<sup>-1</sup></b>
Serum albumin	706.31
cone cGMP-specific 3',3'-cyclic phosphodiesterase $\alpha$ -subunit	224.97
$\alpha$ -1-antiproteinase	298.24
plasminogen	240.30
lactoperoxidase	225.12
kininogen, LMW II	172.21
NADH-ubiquinone oxido-reductase 75	200.88
$\alpha$ -2-HS-glycoprotein	194.21
hemiferrin	171.17
prothromin	161.90
apolipoprotein A-I	139.03
$\alpha$ -1-1-microglobulin and inter $\alpha$ -trypsin inhibitor light chain	110.56
antihrombin III	148.34
integrin $\beta$ -1	179.60
$\beta$ -2-glycoprotein I	130.93
$\alpha$ -2-antiplasmin	121.23
hemoglobin beta fetal chain	109.51
apolipoprotein A-II	70.32
hemoglobin $\alpha$ chain	70.32
$\alpha$ 1 antichymotrypsin	91.51

---

## Appendix II. Scientific contributions

### - List of papers published

Three papers have been published during the elaboration of this thesis:

- **S. Sánchez-González**, N. Diban, F. Bianchi, H. Ye, A. Urriaga. Evidences of the effect of GO and rGO in PCL membranes in the differentiation and maturation of human neural progenitor cells, *Macromol. Biosci.* 1800195 (2018) 1-8.
- **S. Sánchez-González**, N. Diban, A. Urriaga, Hydrolytic degradation and mechanical stability of poly( $\epsilon$ -caprolactone)/reduced graphene oxide membranes as scaffolds for in vitro neural tissue regeneration, *Membranes.* 8 (2018) 1–14.
- N. Diban, **S. Sánchez-González**, M. Lázaro-Díez, J. Ramos-Vivas, A. Urriaga, Facile fabrication of poly( $\epsilon$ -caprolactone)/graphene oxide membranes for bioreactors in tissue engineering, *J. Memb. Sci.* 540 (2017) 219–228.

### - Congress contributions

Seven scientific communications were presented related to this thesis:

- N. Diban, O. David, **S. Sanchez-Gonzalez**, A. Urriaga. A comparative study of poly( $\epsilon$ -caprolactone) membranes functionalized with graphene on flat and hollow fiber configuration for tissue engineering. Euromembrane 2018, Valencia, Spain, 9-13/07/2018. Poster presentation.

- **S. Sánchez-González**, N. Diban, A. Urriaga, Poly( $\epsilon$ -caprolactone) membranes functionalized with graphene-based nanomaterials as scaffolds for neural tissue engineering. 16<sup>th</sup> Network Young Membrains (NYM 2018), Valencia, Spain, 05-07/05/2018. Oral presentation.
- **S. Sanchez-Gonzalez**, F. Bianchi, H. Ye, A. Urriaga, N. Diban. Graphene-poly( $\epsilon$ -caprolactone) mixed-matrix films modulate the differentiation of neural progenitor cells. The World Conference on Carbon 2018 (Carbon 2018), Madrid, Spain, 1-6/07/2018. Oral presentation.
- **S. Sanchez-Gonzalez**, N. Diban, M. Lázaro-Díez, J. Ramos-Vivas, I. Ortiz, A. Urriaga, Highly nutrient permeable poly( $\epsilon$ -caprolactone) scaffolds functionalized with graphene-based nanomaterials for perfusion bioreactors in neural tissue engineering. 28<sup>th</sup> European Society for Biomaterials 2017 (ESB2017), Athens, Greece, 4-8/09/2017. Rapid fire presentation.
- **S. Sánchez-González**, N. Diban, I. Ortiz, A. Urriaga, Poly( $\epsilon$ -caprolactone) membranes functionalized with graphene-based nanomaterials for neural cell growth stimulation. 6<sup>th</sup> European Chemical Society (EuCheMS) Chemistry Congress, Seville, Spain, 11-15/09/2016. Poster presentation.
- **S. Sánchez-González**, N. Diban, i. Ortiz, A. Urriaga, Hydrolytic degradation of porous poly( $\epsilon$ -caprolactone) membranes for neural tissue engineering. X Ibero-american congress on membrane science and technology and VI National congress of the Mexican society of membrane science and technology (CITEM 2016), City of Mexico, Mexico, 22-25/05/2016. Poster presentation.

- N. Diban, **S. Sánchez-González**, I. Ortiz, A. Urriaga, Effect of degradation of poly(epsilon-caprolactone) films on functional properties for tissue engineering bioreactors. 10<sup>th</sup> World Biomaterials Congress (WBC 2016), Montreal, Canada, 17-22/05/2016. Poster presentation.



## *About the author*

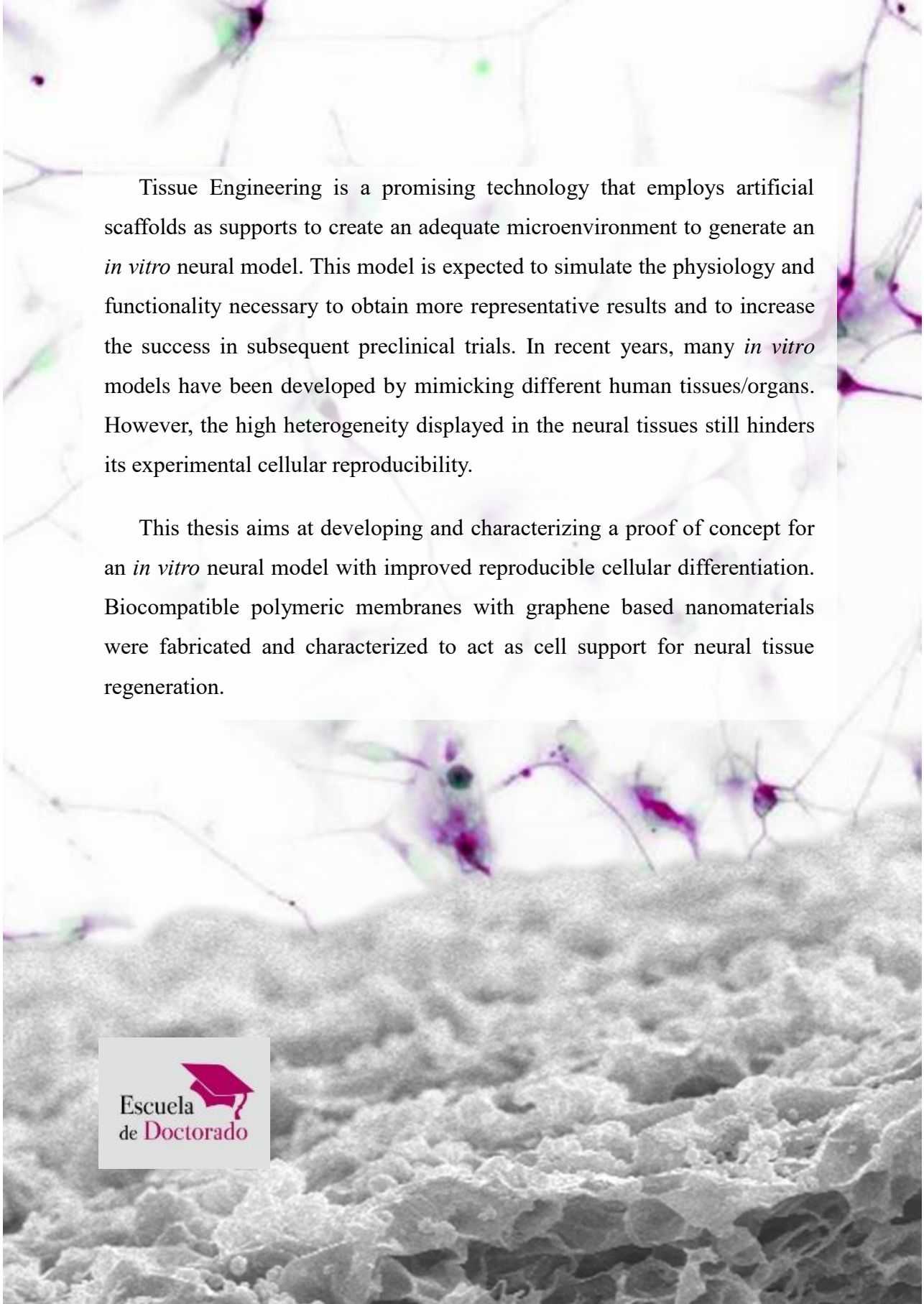
Sandra Sánchez González was born on 10<sup>th</sup> April 1989 in Santander (Cantabria, Spain). She is a Chemical Engineer (2013) from the University of Cantabria and she has specialized in the field of environment throughout the Master's degree in Environment and Clean Technologies (CLEANTECH) (2014) at Deusto University.

Since June 2015, she has been developing her doctoral studies in the PhD program of Chemical Engineering, Energy and Processes under the supervision of Prof. Dr. Ane Urtiaga Mendía and Dr. Nazely Diban Gómez. The work has been carried out in the Department of Chemical and Biomolecular Engineering of University of Cantabria in the group of Environmental Technologies and Bioprocesses (ETB).

During the doctoral thesis, she has collaborated with the research institute of Marqués de Valdecilla (IDIVAL). Moreover, she has had the experience of having completed a research stay at the Institute of Biomedical Engineering in the Department of Engineering Science (University of Oxford) for three months under the supervision of Dr. Hua Ye.

In 2017, she was granted with a Short-Term Fellowship from the European Molecular Biology Organization (EMBO). Moreover, she has been awarded with different prizes of scientific divulgation in the University of Cantabria. To finish, she has published three scientific articles and she has contributed to seven international congresses.





Tissue Engineering is a promising technology that employs artificial scaffolds as supports to create an adequate microenvironment to generate an *in vitro* neural model. This model is expected to simulate the physiology and functionality necessary to obtain more representative results and to increase the success in subsequent preclinical trials. In recent years, many *in vitro* models have been developed by mimicking different human tissues/organs. However, the high heterogeneity displayed in the neural tissues still hinders its experimental cellular reproducibility.

This thesis aims at developing and characterizing a proof of concept for an *in vitro* neural model with improved reproducible cellular differentiation. Biocompatible polymeric membranes with graphene based nanomaterials were fabricated and characterized to act as cell support for neural tissue regeneration.